Numerieke stromingsberekeningen in roterende zuigermachines

Numerical Flow Calculations
in Rotary Positive-Displacement Machines

John Vande Voorde

Promotor: prof. dr. ir. J. Vierendeels
Proefschrift ingediend tot het behalen van de graad van
Doctor in de Ingenieurswetenschappen

Vakgroep Mechanica van Stroming, Warmte en Verbranding
Voorzitter: prof. E. Dick
Faculteit Ingenieurswetenschappen
Academiejaar 2005 - 2006

UNIVERSITEIT
GENT

ISBN 90-8578-041-1
NUR 950, 928
Wettelijk depot: D/2005/10.500/41

Dankwoord

Zoals altijd in het leven, is dit boek niet het werk van 1 man, maar getuigschrift van een periode.

Ik bedank prof. Erik Dick voor de kans en de mogelijkheden die hij mij bood. Evenzo bedank ik prof. Jan Vierendeels, maar ik ben hem nog veel meer verschuldigd voor zijn begeleiding. Zonder hem kon dit werk niet geworden.

Als dit boek voor u ligt, is dit eveneens omdat de vakgroep waarin ik terechtkwam een aangename en vruchtbare omgeving is. Ik wil in het bijzonder Chris, Koen en Yves danken voor hun vriendschap, ook buiten het werk om.

Yves verdient ook expliciet hulde, omdat hij erin slaagde de levensspanne van computers, die in mijn aanwezigheid merkbaar krimpt, voldoende te verlengen. Maar in alle ernst, geen CFD zonder computers en Yves verdient mijn dank.

Tot slot maar niet tenslotte dank ik mijn ouders voor de liefde en de steun die ze mij al mijn hele leven geven. Een belangrijke plaats voor mijn grootmoeder. Dit is voor haar.

Nomenclature

a_b	$\frac{\partial a}{\partial b}$
J	Jacobian
(x, y, z)	coordinates in cartesian coordinate system
$\vec{r}$	coordinate vector in cartesian coordinate system
(χ, ψ)	projection of coordinates (x, y)
(x, Y)	cartesian coordinate system with scaled y-coordinate
Y_B, Y_T	particular values of Y-coordinate
θ	rotation angle
s	arc length
(i, j, k)	tangential, radial and axial coordinates in a structured grid
p	pressure
V	volume
T	temperature
R	gas constant
κ, γ	polytropic and isentropic exponent

ρ	density
m	mass
$\dot{m}$	mass flow rate
$\vec{u}$	velocity vector
$\vec{u}_d, \vec{g}, \vec{g}_0, \vec{v}_{rigid}, \vec{v}_{wall}$	particular velocity vectors
$\vec{u}_b$	grid cell boundary velocity
$\vec{\vec{\tau}}$	friction tensor
E	internal energy
ΔW	specific work
ϵ	efficiency
$\epsilon_V, \epsilon_c, \epsilon_a, \epsilon_T$	volumetric, compression, adiabatic and temperature efficiency
Ω, ω	domains
$\partial\Omega, \partial\omega$	domain boundaries
λ, Λ	Lagrange multiplier, field of Lagrange multipliers
δ	Dirac pulse
C_0	penalty force strength
Φ	potential
Φ_T, Φ_B, Φ_D	particular values of potential Φ

nrl	number of radial nodes in the left grid block
nrr	number of radial nodes in the right grid block
ntl	number of tangential nodes in the left grid block
ntr	number of tangential nodes in the right grid block
$ndiv$	number of nodes on the division line
$R(s), r(s)$	unfiltered, filtered radius of curvature of the division line
$q, \Delta L$	geometric factor and starting length for node spacing according to geometric series
$q_{i,L}, q_{i,R}$	factor q for tangential coordinate i in left, right grid block
ΔL_i	starting length ΔL for tangential coordinate i

Nederlandse Samenvatting

In dit werk wordt een numerieke berekening van de stroming door roterende zuigermachines (ofte volumetrische machines) beoogd.

Zuigermachines zijn pompen en compressoren die een vloeistof, respectievelijk een gas op hogere druk brengen. Dit gebeurt door de vloeistof of het gas in te sluiten in een werkingskamer en vervolgens de inhoud van deze werkingskamer te verplaatsen naar een uitlaat op hogere druk. In het geval van een compressor verkleint het volume van de werkingskamer reeds tijdens de verplaatsing (dus terwijl er geen contact is met de uitlaat, noch de inlaat). Hierdoor treedt reeds een drukverhoging op tijdens de verplaatsing. De aldus gerealiseerde drukverhoging wordt de interne drukverhouding genoemd.

Bij klassieke zuigermachines wordt de werkingskamer gevormd door een heen- en weergaande zuiger in een cilinder. Bij roterende zuigermachines wordt de werkingskamer gevormd door twee rotoren in een behuizing. De meest bekende roterende zuigermachines zijn tandradpompen en schroefcompressoren.

Alhoewel deze machines veel toegepast worden in de industrie, is er relatief weinig kennis over de stroming binnenin deze machines. Aangezien een roterende zuigermachine in se gevormd wordt door twee rotoren die bewegen in een stilstaand huis, treden er onvermijdelijk lekstromen op. Deze lekstromen hebben een grote invloed op het rendement van de machine. Het is belangrijk voor het ontwerp deze lekstromen juist te kunnen begroten. Aangezien experimenteel onderzoek sterk bemoeilijkt wordt door de geometrie, zouden numerieke stromingsberekeningen hierin erg nuttig kunnen zijn.

Desalniettemin zijn er tot op heden bijna geen numerieke stromingsberekeningen uitgevoerd in dergelijke machines. Bij alle volumetrische machines moet de stromingssimulatie zich in de tijd uitstrekken over ten minste een aantal cycli van de machine om zinvol te zijn. Dit betekent echter dat de

rotoren moeten bewegen tijdens de simulatie. Hier bevindt zich het probleem. De beweging van de rotoroppervlakken is zo complex dat ze tot op heden stromingsberekeningen in de weg stond.

Het doel van dit onderzoek is het ontwikkelen van een methode die het mogelijk maakt om stromingsberekeningen uit te voeren in eender welke roterende volumetrische geometrie.

Een eerste techniek die onderzocht wordt is de Fictitious Domain techniek. Met deze techniek is het mogelijk bepaalde grenzen van het fysisch domein niet in het rekendomein op te nemen, doch hun invloed op de stroming te simuleren door de stromingsvergelijkingen lokaal aan te passen. Het wordt onderzocht of het mogelijk is met deze techniek de bewegende rotoroppervlakken uit het rekendomein te verwijderen, wat het probleem de facto zou oplossen.

In de literatuur is er veel verschenen over deze methode toegepast op onsamendrukbare open stromingen. Er wordt onderzocht of het mogelijk is deze methode uit te breiden naar gesloten geometrieen en compressibele stroming. Dit wordt behandeld in hoofdstukken 2 en 3.

Uit dit onderzoek blijkt gedeeltelijk succes voor onsamendrukbare stroming (pompen). Het blijkt echter dat deze methode niet geschikt is voor de studie van de lekstromen. Het is immers niet mogelijk om een scherpe aflijning te bekomen van het ondergedompelde rotoroppervlak. Bovendien treden lokaal onfysische drukpieken op die de lekstromen beinvloeden [50].

Bij de uitbreiding naar samendrukbare stromingen (compressoren) blijkt het niet mogelijk de rotoroppervlakken ondoorlatend te maken voor het gas. Het probleem blijkt van die aard dat het een realistische stromingsberekening in een roterende zuigercompressor verhindert.

In de verdere hoofdstukken van dit werk wordt een tweede techniek uiteengezet, genaamd de Arbitrary Lagrangian-Eulerian ofte ALE techniek.

Deze techniek laat toe dat het rekenrooster beweegt tijdens de berekening, op voorwaarde dat de definities van de rekencellen behouden blijven. Dat betekent dat elke rekencel in het rooster tijdens de simulatie gedefinieerd blijft door dezelfde vlakken en knopen. Praktisch betekent dit dat enkel het bewegen van de roosterknopen toegelaten is. Natuurlijk moet voor elke tijdstap wel een rooster bekomen worden van goede kwaliteit.
Bij deze methode verschuift de moeilijkheid naar het correct manipuleren van

het rekenrooster tijdens de berekening. Er wordt een strategie ontwikkeld die het rekenrooster correct beweegt.

In het geval van een roterende zuigermachine, zijn de enige bewegende grenzen in het rekendomein de oppervlakken van de rotoren. De inlaat en de uitlaat van de machine bewegen niet. Daarom worden deze voorzien van een stilstaand rekenrooster. De roostermanipulatie heeft enkel betrekking op het huis van de machine.

Dit huis wordt voorzien van een gestructureerd hexagonaal rekenrooster. Nu is het zo dat de celdefinities in twee hexagonale gestructureerde roosters met hetzelfde aantal knopen in axiale, radiale en tangentiale richting identiek zijn. Het probleem van het bewegen van het rooster wordt daarmee gereduceerd tot het genereren van een hexagonaal gestructureerd rooster in het huis van de machine voor elke rotatie van de rotoren. Immers, als deze roosters achtereenvolgens aan de stromingsvergelijkingen aangeboden worden, lijkt het voor de stromingsvergelijkingen net alsof het rooster beweegt.

Het rooster in het huis wordt geconstrueerd door tweedimensionale gestructureerde rechthoekige roosters in verschillende sneden loodrecht op de as met elkaar te verbinden (figuur 1). Het probleem wordt hierdoor verder gereduceerd tot het genereren van een tweedimensionaal rechthoekig rooster in een snede van het huis loodrecht op de as, voor elke rotatie van de rotorprofielen.

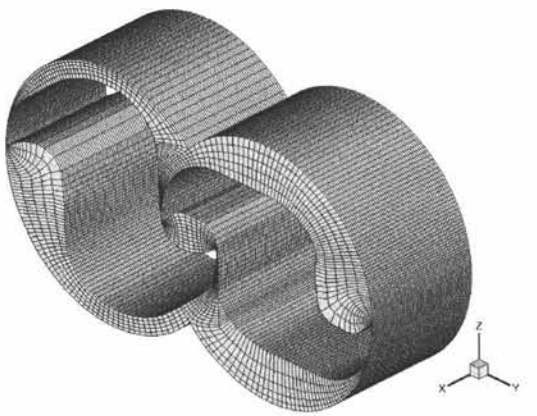

Figure 1: Hexagonaal gestructureerd rooster in de behuizing van een tandcompressor

Tot dit doel wordt een techniek ontwikkeld, die beschreven is in hoofd-

stukken 4 en 5.
Het tweedimensionale gestructureerde rechthoekige rooster wordt geconstrueerd op basis van de oplossing van een potentiaalvergelijking $\nabla^2\Phi = 0$ in het domein (figuur 2). Het gebruik van een potentiaaloplossing om een rooster te bekomen van hoge kwaliteit is reeds langer bekend en gaat terug op Winslow [52] in 1967. Het grote verschil tussen deze methode en alle anderen, afgeleid van de techniek van Winslow, is dat hier de potentiaaloplossing expliciet berekend wordt in het domein. In alle andere technieken is de potentiaalberekening impliciet. Dit verschil laat een grotere controle over de potentiaaloplossing en haar gebruik bij de roostergeneratie toe. Daardoor kan in deze complexe geometrie toch een gestructureerd rooster van hoge kwaliteit bekomen worden.

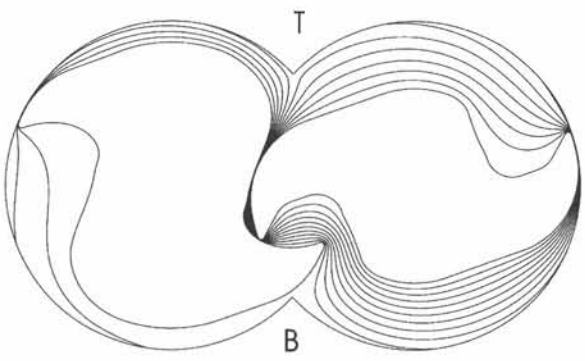

Figure 2: Oplossing van de potentiaalvergelijking in een typisch 2D domein

De strategie die hierboven kort beschreven werd, wordt toegepast op stromingsberekeningen doorheen een tandcompressor (hoofdstuk 6) en een olievrije schroefcompressor (hoofdstuk 7).

Vergelijking van numerieke resultaten met experimentele toont een erg goede overeenkomst. Hierbij moet opgemerkt worden dat van een roostergeneratie standpunt, de geometrie van de olievrije schroefcompressor de meest complexe is van alle roterende zuigermachines. De geometrie is sterk driedimensionaal door de schroefvorm van de rotoren. Bovendien zijn de verscheidene spleten die optreden extreem klein (van een orde tientallen micrometer voor een rotordiameter van een orde 100 mm).

Daarom wordt besloten dat de techniek gevalideerd is door de voorgestelde berekeningen. De roostermanipulatie en -generatie mag beschouwd worden als volledig ontwikkeld.

In de toekomst kan deze techniek gebruikt worden om de verschillende

invloeden op het rendement van roterende zuigermachines (en in het bijzonder schroefcompressoren) te onderzoeken. Vooral de invloed van de grootte van de verschillende spleten en de vorm van de rotorprofielen lijken interessant. Dit kan het inzicht in de werking van en de evolutie van deze machines bevorderen.

Een volgende stap in de simulatie van roterende zuigercompressoren moet zeker de injectie van olie in de machine zijn. Het gedrag van de ingespoten olie is complex en het is van groot belang dit gedrag goed te simuleren. De olie mengt zich sterk met het comprimerende gas. Terwijl het dit doet, onttrekt het warmte aan het gas, wat het rendement verhoogt. Bovendien vormt de olie een film op de verschillende oppervlakken die verschillende spleten effectief dicht. Dit komt het rendement eveneens sterk ten goede.
Het correct simuleren van zowel het opbreken van de olie in een wolk en het vormen van een oliefilm belooft een flinke uitdaging.

English Summary

The research presented in this book aims at the numerical calculation of flow through rotary positive-displacement machines.

Positive-displacement machines are pumps and compressors used to pressurize a fluid, or a gas respectively. This is done by isolating the fluid or the gas in a working chamber and subsequently transferring the content of the working chamber to an outlet at higher pressure. In the case of a compressor, the volume of the working chamber is reduced during this transfer (so while there is contact with neither the outlet nor the inlet). This results in a pressure rise during the transfer, which is named the internal pressure ratio.

In a piston machine, the working chamber is formed by a piston moving up and down in a cylinder. In a rotary positive-displacement machine the working chamber is formed by two rotors in a housing. The most commonly known rotary positive-displacement machines are gear pumps and screw compressors.

As a rotating positive-displacement machine is in essence formed by two rotors rotating in a stationary casing, it is inevitable for various leakage flows to occur. These leakage flows have a very large impact on the compressor efficiency. It is paramount that these leakage flows are assessed correctly. As experimental flow analysis is severely hampered by the geometry, numerical flow calculations could prove to be very useful.

Nonetheless, hardly any numerical flow calculations have been performed on these machines until present day. As the operating principle of these machines is volumetric, the simulation run has to span several cycles of the machine. This means that the rotor surfaces have to move during the simulation. This is the problem. The movement of the rotor surfaces is of such a complexity that is has made numerical flow calculations impossible to this date.

The goal of this research is to develop a method that allows numerical flow calculations in any rotating positive-displacement machine geometry.

A first technique studied is the Fictitious Domain technique. With this technique it is possible to ignore certain specific boundaries to the flow domain by simulating their influence on the fluid flow by modifying the flow equations. It is investigated whether it is possible with this technique to lift the moving rotor surfaces from the calculation domain, as this would de facto solve the problem.

In literature, much was published on the application of this method to incompressible flow with moderate pressure build-up. It is studied whether this method can be extended to flows in closed geometries and to compressible flows. This study is reported in chapters 2 and 3.

Moderate success is achieved for incompressible flows (pumps). But the method is not suited for the study of the leakage flows. It is not possible to obtain a sharp (fictitious) boundary at the immersed rotor surface. Furthermore, unphysical pressure peaks are present which influence the leakage flows too much [50].

The extension of the method to compressible flows proved impossible. Severe problems arise concerning the impermeability of the (fictitious) rotor surfaces. The problem is such that it makes realistic flow calculations in a rotary positive-displacement compressor unachievable.

In the remaining chapters of this book a second method is described, namely the Arbitrary Lagrangian-Eulerian or ALE method.

This method allows the calculation grid to move during the simulation, on the condition that the grid cell definitions are maintained. This means that all grid cells are defined by the same faces and nodes during the entire simulation. In practice, this means that it is only allowed to move the grid nodes. Obviously, a grid of good quality has to be obtained for every time step.
Thus the focus of the difficulties is shifted to the correct manipulation of the grid during the calculation. A strategy is developed that moves the grid correctly.

For rotary positive-displacement machines, the only moving boundaries to the flow domain are the rotor surfaces. The inlet and the outlet are stationary.

Therefore these are furnished with a stationary grid. The grid manipulator only has effect on the grid in the machine casing.

The casing is furnished with a hexagonal structured grid. It is a known fact that two hexagonal structured grids with the same number of nodes in axial, radial and tangential direction, have identical grid cell definitions. The grid manipulation problem is therefore reduced to generating a hexagonal structured grid in the casing for any rotation of the rotors. After all, if these grids are provided to the flow solver one after the other, it seems to the flow solver as if the grid is moving.

The grid in the casing is constructed by connecting two-dimensional structured rectangular grids in slices of the casing perpendicular to the rotor axis (cf. figure 3). This way the grid movement problem is further reduced to generating these two-dimensional structured rectangular grids in a slice of the casing, for any rotation of the rotor profiles.

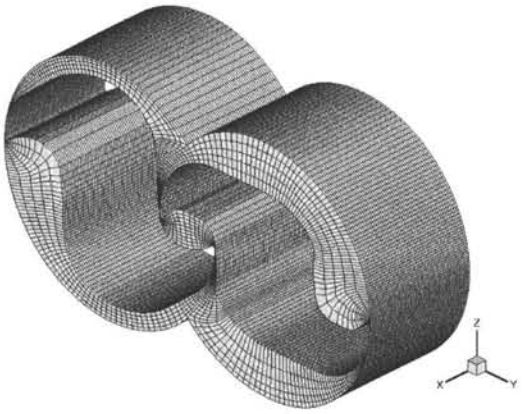

Figure 3: Hexagonal structured grid in a tooth compressor casing

To this end a grid generator was developed, which is described in chapters 4 and 5.
The two-dimensional structured rectangular grid is constructed based on the solution of a potential equation $\nabla^2\Phi = 0$ in the 2D flow domain (cf. figure 4). The use of a potential solution to construct a grid of high quality is well-known. It dates back to Winslow in 1967 [52]. The important difference between this method and all methods derived from Winslow's method, is that here the potential solution is explicitly obtained in the flow domain. In all other methods, this solution is implicit. This difference allows far more control over the potential solution and its use in the grid generation process. This allows

to construct a structured grid of high quality in such complex geometries as considered here.

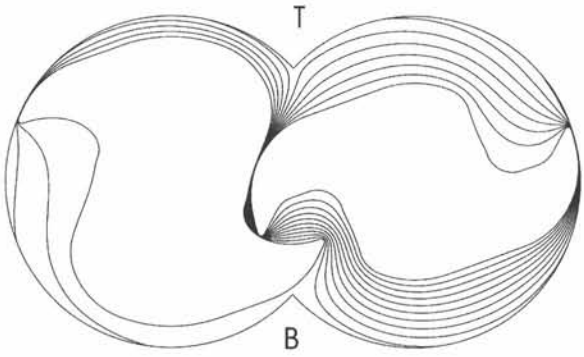

Figure 4: Potential solution in a typical 2D domain

The grid manipulation strategy as described above is applied to calculations of flow through a tooth compressor (chapter 6) and through an oil-free screw compressor (chapter 7).

Comparison of numerical results with experimental results shows a good agreement. It should be mentioned that from a grid generation viewpoint, the oil-free screw compressor geometry is the most complex of all rotating positive-displacement machines. Because of the helix in the screws, the flow domain is distinctly three-dimensional. Furthermore, the size of the various gaps between rotors and casing is extremely small (order tens of micron versus a rotor diameter of order 100 mm).

Therefore it is concluded that the technique is validated by the presented calculations. Both grid generation and manipulation are considered fully developed.

In the future, this technique can be applied to study the various influences on the efficiency of rotary positive-displacement machines, and screw compressors in specific. An interesting study could be aimed at the influence of the gap sizes and the rotor profiles.

A next step in the simulation of rotating positive-displacement machines is the introduction of oil injection in the casing. The behaviour of the injected oil in the gas is complex. It is important to capture the behaviour correctly. The oil breaks up in sprays and mixes with the compressing gas. In doing this, heat is extracted from the compressing gas, which has a positive impact on

the compression efficiency. On the other hand, oil hitting the surfaces forms a liquid film. This film is very effective in sealing various leakage gaps, which in turn also has a large positive influence on the efficiency. Simulating both the break-up in a spray and the formation of an oil film promises quite a challenge.

Contents

Chapter 1

Rotary Positive-Displacement Machines

In this book the possible use of Computational Fluid Dynamics or CFD in rotary positive-displacement machines (also known as rotary volumetric machines) is studied. These machines represent a substantial part of the flow machines industrially used. However, there is not much insight in the flow conditions inside these machines. Because of the specific closed-up geometry of the machines, experimental flow analysis is difficult. Computational Fluid Dynamics could be a valuable tool to obtain better understanding of the internal flow conditions, which is needed for further improvement of these machines. There are however problems associated with performing such flow calculations. This study tries to assess and overcome the problems obstructing the use of CFD in rotary positive-displacement machines.

In this first chapter, rotary positive-displacement machines will be described to allow a good understanding of the working principle of these machines. The fundamental problem obstructing the use of CFD will be explained. Two possible methods offering a solution will be presented. In the following chapters, these methods will be studied for both compressible and incompressible flow and conclusions will be drawn from the study. In the final chapter, all conclusions will be collected.

1.1 Definition

Positive-displacement machines or volumetric machines are characterized by having a working volume that increases in volume when in contact with the inlet, and that decreases in volume as it expels fluid in the outlet. The best-known example is a piston pump or piston compressor (figure 1.1).

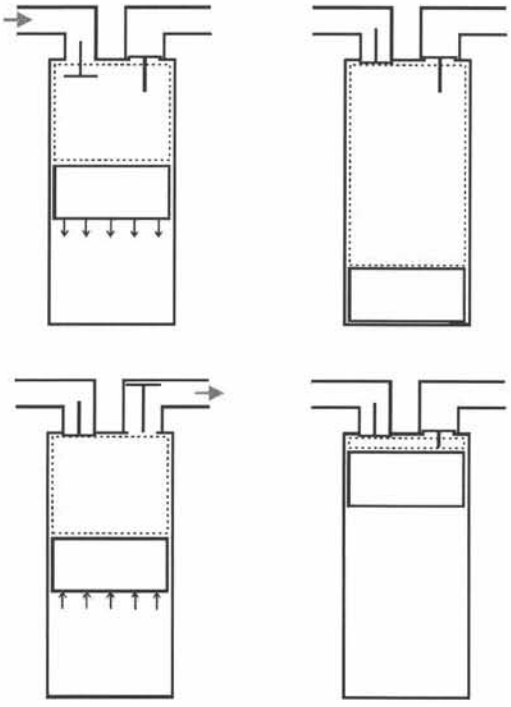

Figure 1.1: Operating principle of a piston pump or compressor; fltrttb : suction phase; maximum working chamber volume and end of suction phase; reduction of working chamber volume (possibly with internal compression); minimum working chamber volume and end of discharge phase

A piston machine consists in essence of a piston that moves up and down in a cylinder. The working volume is the volume inside the cylinder. As the piston moves down, the working volume increases. This creates a pressure drop. The inlet valve opens and fluid is sucked into the cylinder from the inlet. When the piston reaches its lowest point, the working volume is at its largest and the inlet valve closes. As the piston moves up, the working volume decreases. The pressure in the cylinder rises. If the fluid is incompressible (piston pump) the outlet valve opens immediately and the fluid is pushed into the outlet. If the fluid is compressible (piston compressor) the pressure in the

cylinder will rise until the pressure is larger than the outlet pressure. At this value the outlet valve opens and the gas is expelled in the outlet.

This process is fundamentally different from what happens in turbo machinery. In a turbo machine the work is transfered directly from rotating blades onto the fluid to augment its energy (or vice-versa for a turbine). The fluid flow is continuous. For a volumetric machine, the energy is transferred to or from the fluid by trapping it in a closed working chamber and subsequently changing the volume of this working chamber.

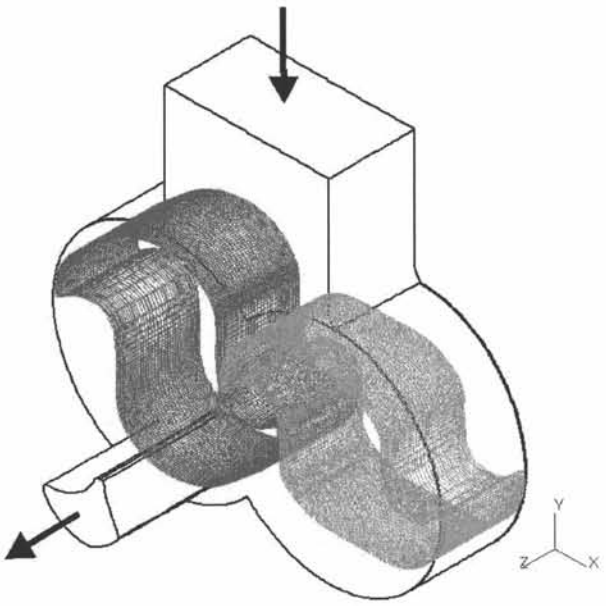

Figure 1.2: A typical tooth compressor geometry; inlet at the top and axial outlet

The volumetric machines considered in this book are rotary. This means that the change in volume of a working chamber is not the result of the linear motion of a piston, but of the rotation of one or two rotors. Figure 1.2 shows the geometry of a tooth compressor. The compression cycle is illustrated in figure 1.3.

The rotor surfaces and the housing of the compressor bound the working chamber. At any time two working chambers can be defined. As the rotors turn, a working chamber first increases in volume. At this time it is in contact with the inlet from which is sucks gas. From a specific position of the rotors on, the working chamber is cut off from the inlet. It is not yet in contact

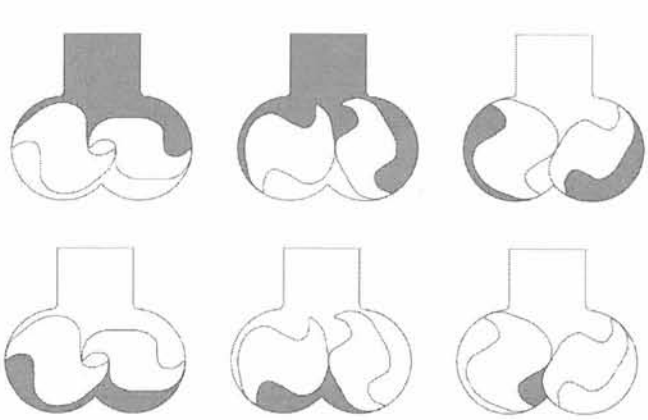

Figure 1.3: Operating principle of a tooth compressor

with the outlet port. As the rotors turn on, the isolated working chamber is reduced in volume and the pressure in it rises. For another specific position of the rotors, the working chamber comes in contact with the outlet port. From then on, the gas is expelled in the outlet as the rotors keep turning.

From the time at which the working chamber is cut off from the inlet to the time when it first makes contact with the outlet port, the volume of the working chamber is reduced by a constant factor. This factor is named the volume ratio. It is often referred to in terms of pressure and is then called the internal pressure ratio of the machine. Of course the pressure ratio is also determined by the nature of the compressed gas. The internal volume ratio is completely determined by the geometry of the inlet port and the outlet port. It is fixed for a specific geometry. All rotary positive-displacement machines have a fixed internal volume ratio. Obviously, for a rotary volumetric pump the internal volume ratio must be one.

Compared to other positive-displacement machines (which all work on the principle of the piston machines) rotary positive-displacement machines have a number of distinct advantages.

As there are no reciprocating or eccentrically rotating masses such as pistons and cranks in a rotary machine, these are inherently much better balanced. By consequence, they can operate at a high rotational speed while producing relatively little noise. Rotary volumetric machines are therefore in general much more compact than their piston counter parts. Good examples are the screw compressors in the mobile pressurized-air generators used frequently in construction.

Another advantage of the high rotational speed at which rotary volumetric machines operate, is the much more constant flow rate. While a screw compressor rotating at 10000 rpm may perform 60000 compression cycles per minute, a piston compressor rotating at 1000 rpm (of the crank shaft) will perform only 1000 compression cycles per minute. Obviously, the output flow rate of the piston compressor is more pulsed.

A third advantage is the absence of valves. In a piston machine, both the inlet and the outlet are at the same end of the cylinder. Because of this, valves are needed to direct the inlet flow from the inlet into the cylinder and the compressed gas from the cylinder into the outlet. Not only are the valves the most fragile parts of the machine, but they also add substantial losses to the inlet and outlet flow. After all, the inlet port and the outlet port are at the same end of the cylinder, which is in area relatively small. The presence of the valves adds to the losses. Rotary positive-displacement machines on the other hand have inlet and outlet ports at different ends of the housing. At no time the working chamber is in contact with both the inlet and the outlet ports, so there is no need for valves.

A specific advantage applies only to rotary positive-displacement compressors, and not to pumps. A rotary volumetric compressor, is very tolerant to liquid carry-over. This can be a significant advantage as the liquid phase can be used to seal leakage gaps and to cool the gas during compression. This significantly reduces the amount of work needed per compression cycle. The liquid phase is usually extracted from the compressed gas in an extruder. The most common example where this principle is applied is the oil-injected compressor. Because of the injection of oil, higher pressure ratios can be obtained with a good efficiency.

Versus these advantages stand two big disadvantages.

The leakages in rotary positive-displacement machines are higher than in piston compressors. This brings down the overall efficiency of these machines. It also introduces a slight dependency of the flow rate on the pressure ratio between inlet and outlet. A specific advantage of positive-displacement machines over turbomachinery is just this independency of the flow rate on the pressure rise.

A second important disadvantage is the fixed volume ratio, and thus pressure ratio. In a piston compressor, the outlet valve doesn't open until the pressure in the working chamber reaches the outlet pressure. In rotary volu-

metric compressors, the pressure rise obtained inside the working chamber is fixed by the geometry of the inlet and the outlet ports. If the outlet pressure is higher, gas flows back from the outlet into the working chamber. In the end all gas is expelled into the outlet at the higher pressure, but at the cost of compression losses. This phenomenon is called undercompression. If the outlet pressure is lower than the pressure in the working chamber, obviously more energy than necessary has been put in the compression to the higher pressure. This is called overcompression. Both will be handled more elaborately further on in this chapter.

1.2 Rotary positive-displacement pumps

1.2.1 Work and efficiency

When the fluid is incompressible, the ideal $p - \theta$ diagram and $p - V$-diagram of the rotary positive-displacement pump is shown in figure 1.4. As long as the working chamber is in contact with the inlet port, the pressure is equal to the inlet pressure. Once the working chamber comes in contact with the outlet port, the pressure rises immediately (discrete) to the outlet pressure.

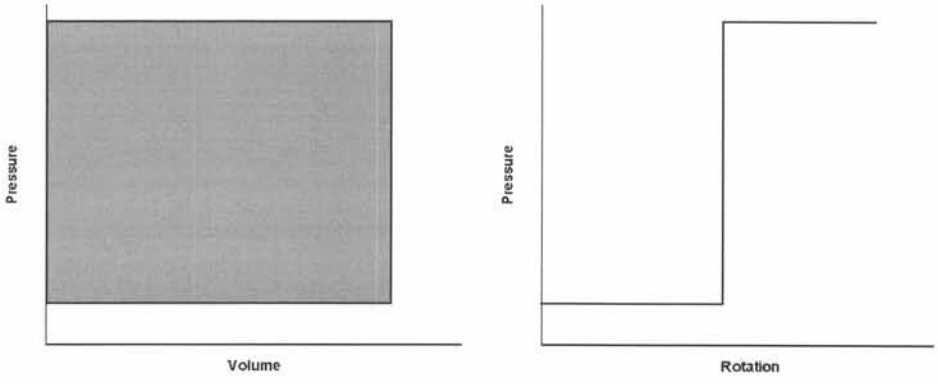

Figure 1.4: Idealized $p - V$ and $p - \theta$ diagrams for a positive-displacement pump

It is possible to have a period in-between where the working chamber is neither in contact with the inlet nor the outlet port. During this period the volume of the working chamber may not change. If the fluid were really incompressible, a change of volume would result in an infinite pressure rise or

drop. In reality, this pressure change is not infinite, but nevertheless very large, and can only be alleviated through violent leakages from or to the working chamber.

To determine the overall efficiency of a positive-displacement pump mechanical losses (such as friction losses in the transmission etc) are disregarded. For the ideal p-V diagram shown in figure 1.4 all the work added to the fluid by the rotors is used to expel the fluid against the outlet pressure. The efficiency of this is 100%. The gray-coloured area in the p-V diagram represents the work needed for one pumping cycle. The specific work can easily be determined to be :

$$\Delta W = \frac{(p_{out} - p_{in})}{\rho_{in}} \tag{1.1}$$

In reality, a small bit of the work added to the fluid is dissipated through frictional losses, both internal in the fluid (mixing losses and turbulent losses) and as friction between the fluid and the rotors and housing. These losses are however very small and may be ignored.

The major loss in a rotating positive-displacement pump is the leakage flow in the gaps between the rotors (in motion) and the (stationary) housing. This loss is expressed in a volumetric efficiency. This is the ratio of the actual flow rate $\dot{m}$ to the theoretic flow rate $\dot{m_{th}}$ (without leakages).

$$\epsilon_v = \frac{\dot{m}}{\dot{m_{th}}} \tag{1.2}$$

For a positive-displacement pump, the volumetric efficiency may be considered to be the overall efficiency.

1.2.2 Application

Rotary positive-displacement pumps can produce a medium-range mass flow rate. The pressure rise they can handle is also considered to be medium-range. If a high and controlled pressure is a design characteristic, piston pumps are usually favoured as the outlet pressure can be easily and correctly controlled using the outlet valve.

This puts rotary volumetric pumps in the same range of turbopumps, which are usually preferred. The most important advantage rotary volumetric pumps have over turbopumps, is that the mass flow rate is (very nearly) independant of the pressure rise. Application of rotary volumetric pumps is most common in situations where this characteristic is important.
In general, rotating volumetric pumps have a rather small application domain.

Examples of rotating positive-displacement pumps are gear pumps and lobe pumps in all their configurations (figure 1.5).

1.3 Rotary positive-displacement compressors

1.3.1 Work and efficiency

For rotating positive-displacement compressors a volumetric efficiency is defined analogous as for pumps (1.2). The work needed for the compression is however also dependant on the compression cycle. Besides the volumetric efficiency ϵ_v, a compression efficiency ϵ_c of some form is introduced. The compression efficiency is the ratio of the specific work W_t needed to compress the gas in a theoretical compression cycle to the specific work W_r really needed to perform the compression. This leads to the following definition of the overall efficiency :

$$P = \dot{m} \cdot W_r = \frac{\epsilon_v}{\epsilon_c} \cdot \dot{m_{th}} \cdot W_t \tag{1.3}$$

For a positive-displacement compressor, the relation between pressure and volume is polytropic (figure 1.6). The polytropic exponent is κ.

$$p \cdot V^{\kappa} = C^{onstant} \tag{1.4}$$

In general the relation between the rotation angle θ and the volume of the working chamber is of a form as depicted in figure 1.7. It is possible to construct a compressor where the volume of the working chamber stays constant over a certain rotation, but this transport of gas without compression is not loss-free. As during this transport no useful work is added to the gas, it merely brings down the efficiency of the compression. It is usually avoided in real-use compressors. The relation between pressure and rotation angle θ of the rotors is depicted in figure 1.8.

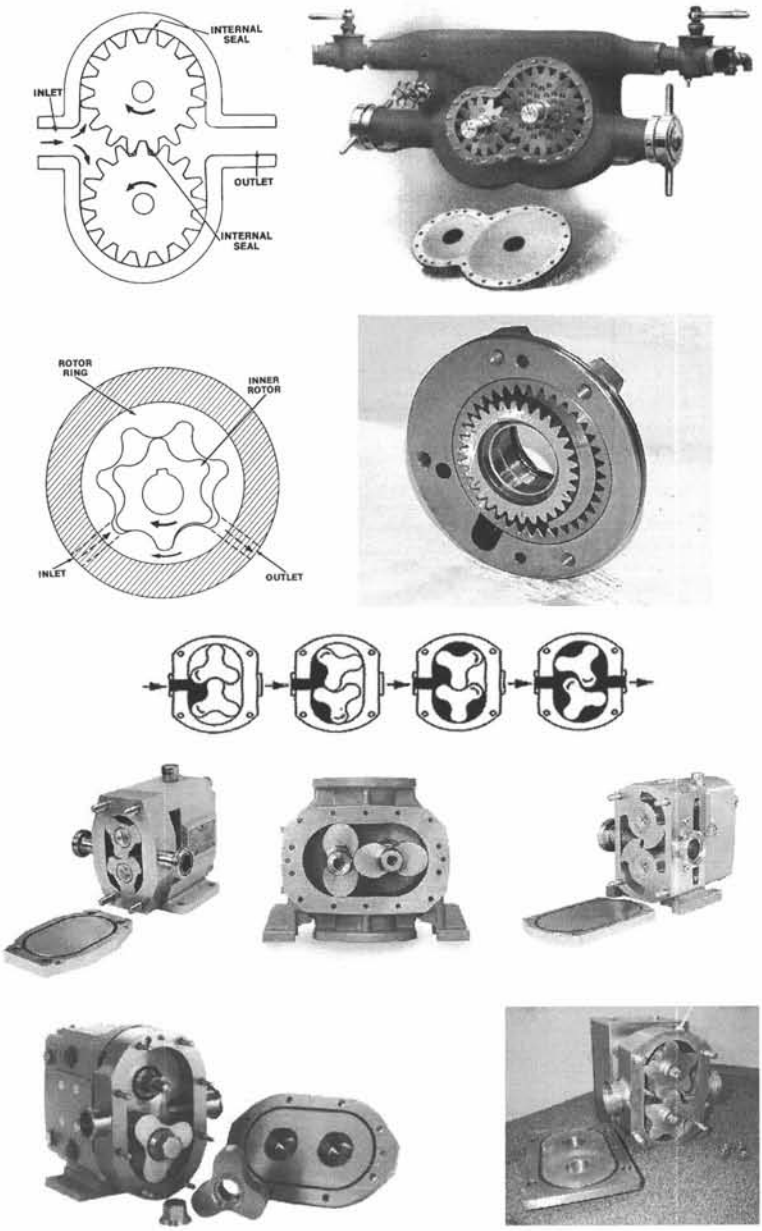

Figure 1.5: Several examples of internal and external gear pumps and lobe pumps

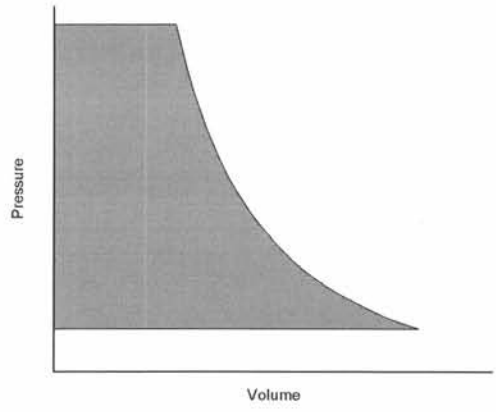

Figure 1.6: The polytropic relation between pressure and volume

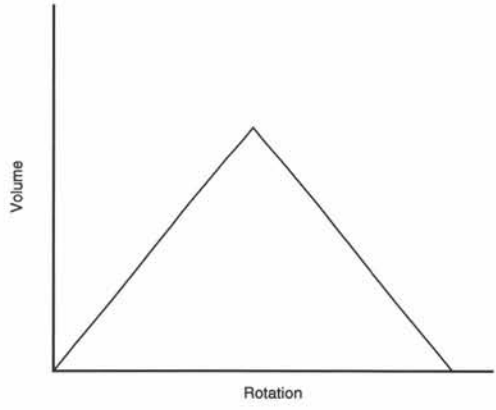

Figure 1.7: Change of volume versus the rotation angle θ

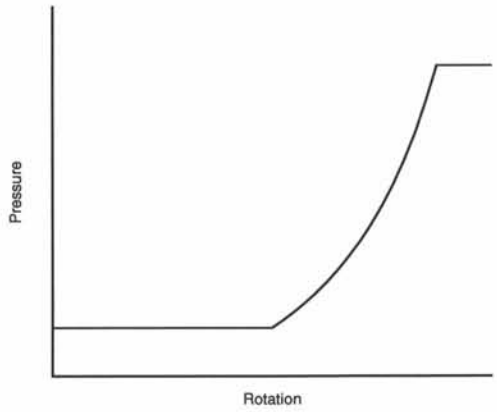

Figure 1.8: Idealized p-θ diagram for a positive-displacement compressor

In figure 1.6, the work needed for one compression cycle between pressures p_1 and p_2 is the gray-coloured area under the polytropic curve.
This work is :

$$\oint_{p_1}^{p_2} V \cdot dp \tag{1.5}$$

With the polytropic relation (1.4) this can be rewritten as :

$$\oint_{p_1}^{p_2} p_1^{\frac{1}{\kappa}} V_1 p^{-\frac{1}{\kappa}} dp = \frac{\kappa}{\kappa - 1} p_1 V_1 \left[\left(\frac{p_2}{p_1} \right)^{\frac{\kappa-1}{\kappa}} - 1 \right] \tag{1.6}$$

The specific work W (work per mass unit) is derived from (1.6) to be :

$$W = \frac{\kappa}{\kappa - 1} R T_1 \left[\left(\frac{p_2}{p_1} \right)^{\frac{\kappa-1}{\kappa}} - 1 \right] \tag{1.7}$$

When the polytropic relation (1.4) is combined with the ideal-gas law

$$pV = mRT \tag{1.8}$$

an alternative polytropic relation is obtained :

$$pT^{\frac{\kappa}{1-\kappa}} = C^{onstant} \tag{1.9}$$

and (1.7) can be rewritten as :

$$W = \frac{\kappa}{\kappa - 1} RT_1 \left(\frac{T_2}{T_1} - 1 \right) \tag{1.10}$$

From (1.10) it is clear that the specific work needed for a pressure rise from p_1 to p_2 is lower if the final temperature T_2 is lower. In practice, this means that the extraction of heat from the compressing gas lowers the work needed for the compression.

Consider a polytropic exponent κ of value 1. This signifies isothermal compression. After all :

$$pV = C^{constant} = mRT \tag{1.11}$$

The second law of thermodynamics forbids heat transfer from matter at a lower temperature to matter at a higher temperature. So the theoretical maximum amount of heat is extracted from the compression for isothermal compression. This means that isothermal compression needs the minimal amount of compression work and that $\kappa = 1$ is the lower limit for the polytropic exponent.

One could define a compression efficiency ϵ_c as the ratio of the work needed to compress along the real polytrope between two pressures, to the theoretical minimal amount of work needed to compress isothermally between these two pressures.

However, it is current practice to use the work needed for adiabatic isentropic compression (polytropic exponent $\gamma = 1.4$ for air) as the theoretical work needed. This efficiency is called adiabatic efficiency ϵ_a.

$$\epsilon_a = \frac{W_a}{W_r} \qquad \text{with} \qquad W_a = \frac{\gamma}{\gamma - 1} RT_1 \left[\left(\frac{p_2}{p_1} \right)^{\frac{\gamma - 1}{\gamma}} - 1 \right] \tag{1.12}$$

Note that an adiabatic efficiency of more than 100% is in theory possible.

The (adiabatic) efficiency of compression will be large if the compressed gas is well-cooled during compression. Due to the short time it takes to complete a compression cycle (rotary positive-displacement compressors operate at high

rotational speeds), it is not possible to efficiently cool the compressing gas through external cooling. However, rotary positive-displacement compressors are very tolerant to liquids in the compressing gas (liquid carry-over). Specifically screw compressors are often injected with oil. Because of the intimate mixing with the gas during compression, this significantly cools the compression. This allows high compression efficiencies to be obtained in oil-injected screw compressors.

If the extraction of heat from the gas during compression raises the compression efficiency, of course heat transfer to the compressing gas lowers the efficiency. Only a small part of this heat flows from external sources (such as heat transfer through the compressor housing and rotors from the warm outlet port to the cool inlet port). It is mainly the leakage flows that are responsible for heating of the compressing gas. Because the rotors have to rotate in a stationary housing, leakages are inevitable. More specifically, gas not only leaks back to the inlet port or the outside atmosphere, but also from a compression chamber at a higher pressure and thus also higher temperature to the neighbouring compression chamber at lower pressure. This leaked gas mixes with the gas in the compression chamber at lower pressure and temperature and thus raises the temperature in this chamber. Thus the leakage flows do not only directly influence the volumetric efficiency ϵ_v, but also the efficiency of the compression. It makes insight in these leakage flows a very important issue.

It should be noted that in industry often other characteristics are used than the compression efficiency ϵ_c. For oil-free screw compressors often the polytropic exponent κ derived from the real work W_r is used to express compression efficiency. For oil-injected screw compressors, usually the work is recalculated to a nominal torque needed to rotate the rotors. These characteristics are used as they give a more at-glance insight in the efficiency for a specific type of compressor. As the definition of adiabatic efficiency ϵ_a is generally valid and to avoid confusion in efficiency characteristics, in this book only volumetric efficiency and adiabatic efficiency will be used.

1.3.2 Overcompression and undercompression

As mentioned above, rotating positive-displacement compressors have a constant volume ratio determined by the position and geometry of the inlet and outlet ports. With this volume ratio corresponds a specific internal pressure ratio. If the pressure ratio between outlet port and inlet port is not the same

as the internal pressure ratio, the machine is subject to under- or overcompression. Overcompression occurs when the pressure in the outlet is lower than the pressure at the end of the compression cycle. Undercompression occurs when the pressure in the outlet is higher than the pressure at the end of the compression cycle. Figures 1.9 and 1.10 plot the pressure in a working chamber versus the volume of the working chamber for under- and overcompression.

In figure 1.9 a compression with undercompression is depicted idealized. The undercompression is unrealistic in that it is assumed that the pressure in the working chamber rises immediately (discrete) to the outlet pressure as soon as the outlet port is reached. A plot demonstrating real undercompression is shown in figure 1.11.

In figure 1.9, the bold line shows the compression cycle with undercompression. The fine line shows the cycle for a pressure ratio equal to the internal pressure ratio of the compressor. The gray rectangular area corresponds with extra work needed versus a situation where the pressure ratio is the internal pressure ratio. The rotors need this extra work to expulse the gas against the higher outlet pressure.

However, it would not be correct to classify the entire rectangular gray area as a loss. After all, the gas that flows back from the outlet in the working chamber raises the pressure in the chamber to the outlet pressure. It would be better to compare the undercompression with a cycle where the compression is continued with the same polytropic exponent until the desired outlet pressure is reached (dashed line in figure 1.9). In this sense, only the dark gray area marked L is in fact a loss that can be avoided.

Figure 1.10 depicts a compression with idealized overcompression. The full line shows the cycle with overcompression. A hypothetical cycle where the internal pressure ratio equals the real pressure ratio is also depicted. The entire area coloured gray is a loss. This loss is in fact extra work needed by the rotors to compress the gas to a too high pressure. All of this extra work is subsequently dissipated as mixing losses when the gas is expulsed in the outlet.

Consider the definition of adiabatic efficiency in formula (1.12). In this formula p_2/p_1 is the (external) pressure ratio. In figures 1.9 and 1.10 the compression cycles are depicted where the internal and the external pressure ratio are adjusted to each other. For these cycles the adiabatic efficiency is determined by the polytropic exponent κ of the cycle as discussed above.

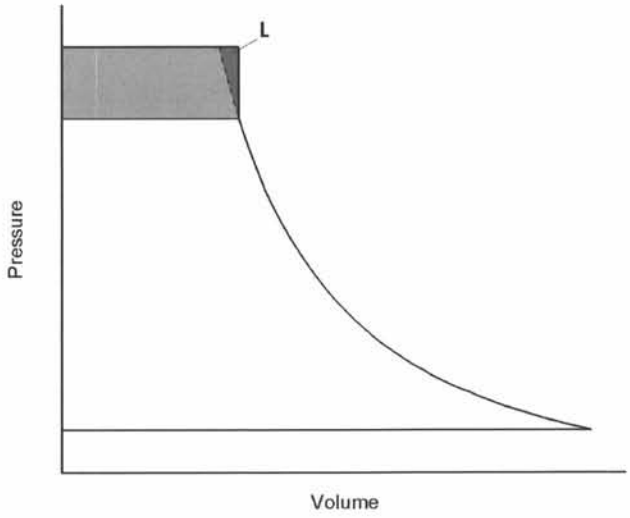

Figure 1.9: Idealized p-V diagram in case of undercompression

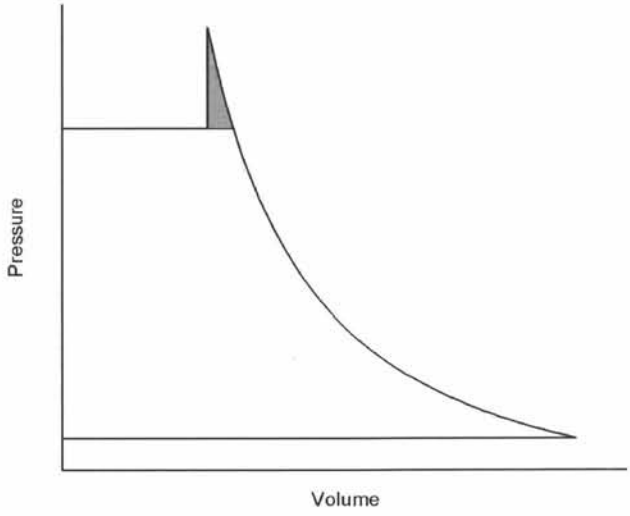

Figure 1.10: Idealized p-V diagram in case of overcompression

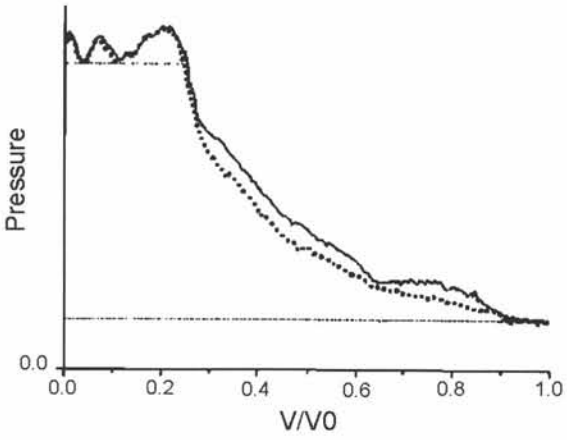

Figure 1.11: Realistic p-V diagram in case of undercompression

However, the gray areas (only the one marked L in figure 1.9) correspond with extra losses due to under- and overcompression. Therefore under- and overcompression lower the adiabatic efficiency of a compressor.

1.3.3 Application

The application range of rotary positive-displacement compressors is for medium pressure ratios and medium mass flow rates. Similarly as for volumetric pumps, the application range is bounded by the piston compressors for high pressure ratios and low mass flow rates and by turbocompressors for high mass flow rates (cf. figure 1.12).

However, rotary positive-displacement compressors experience less competition from turbomachinery than rotary volumetric pumps. At present, they have carved their own place in industry. As much-used pressure ratios fall in the pressure application range, rotating positive-displacement compressors constitute an important part of the compressor industry.

Certain types of rotary volumetric compressors have specific advantages that increase their use. Oil-free screw compressors are often preferred when clean pressurized air is needed. Oil-injected screw compressors on the other hand are very efficient (due to the oil cooling of the compressing air), compact and generate pressurized air that contains a small amount of oil to lubri-

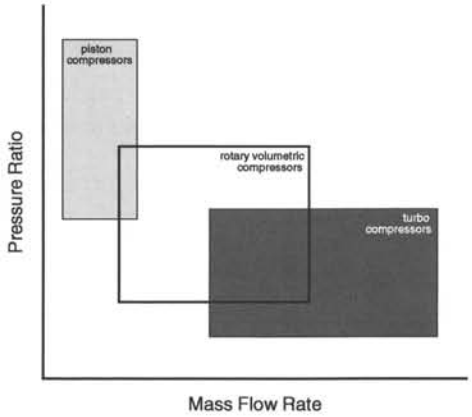

Figure 1.12: Illustration of the application ranges of rotary positive-displacement compressors, relative to piston compressors and turbocompressors

cate air-driven appliances. This makes them desirable for mobile construction work. Examples of rotating positive-displacement compressors are screw compressors, tooth compressors and roots blowers (figure 1.13 and 1.14).

1.4 Rotary positive-displacement expanders

A third group of rotating volumetric machines are expanders. They perform in essence the inverse operation of compressors. By expanding pressurized gas through the machine, the rotors are driven. The expansion cycle is polytropic and thus the p-V diagram looks the same as the p-V diagram for a compressor (figure 1.8).

Just like rotating volumetric compressors, expanders have a geometrically determined internal volume and pressure ratio. Analogous as to what occurs in volumetric compressors, underexpansion and overexpansion occur if the pressure ratio between inlet and outlet is not equal to the internal pressure ratio (figure 1.15). Similar as with over- and undercompression, over- and underexpansion lead to a drop in efficiency.

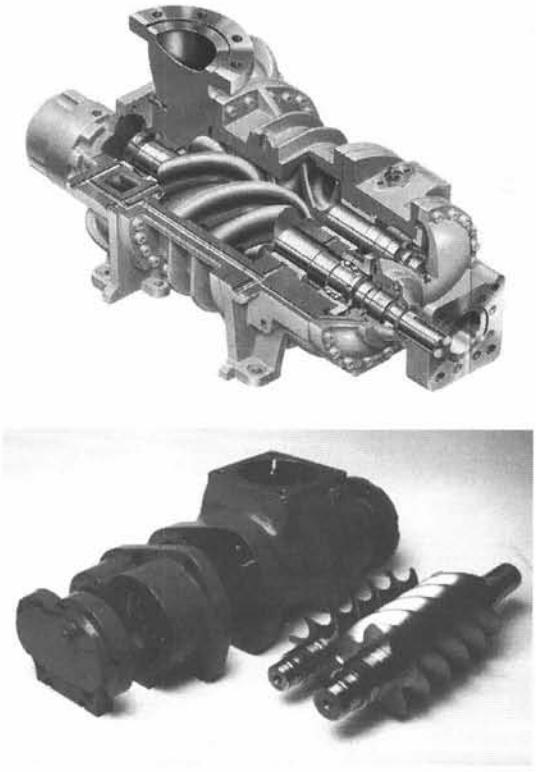

Figure 1.13: Examples of screw compressors

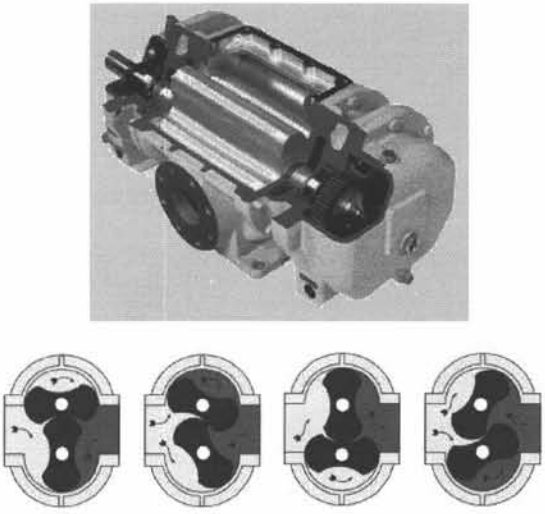

Figure 1.14: Example of a roots blower

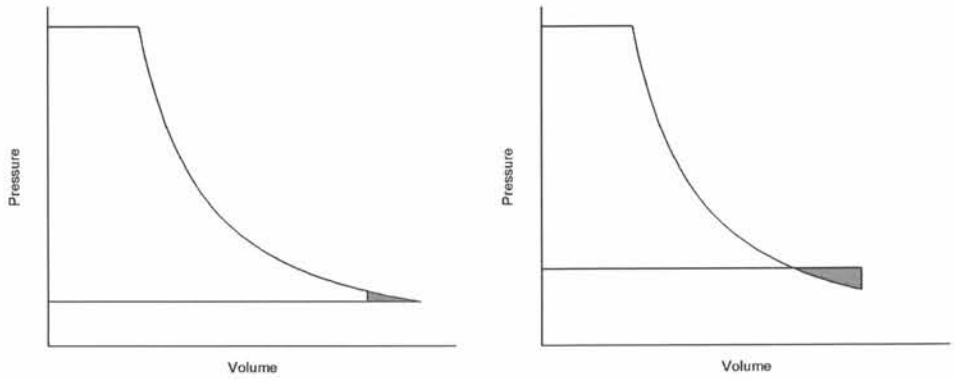

Figure 1.15: Idealized p-V diagrams in case of underexpansion and overexpansion; losses are marked in gray

As turbines (turbo machines) exist for a large variety of flow rates and pressure ratios with a higher efficiency than expanders, the use of expanders is at best marginal. They will not be handled further in this book.

1.5 Problem and importance of CFD

Computational fluid dynamics or CFD could prove to be a useful tool in the development and design of rotating positive-displacement machines, and in specific compressors. Over the years, a lot of research has been performed to further the development of these machines. As the twin-screw compressor is the most widely used, it is also the most widely studied. From this research some conclusions can be drawn.

First off, it is useful to have insight in the inlet and outlet flow. The geometry of the inlet and outlet can either reduce or increase hydrodynamic and aerodynamic losses. If the flow is compressible, the interaction of running waves in the complete piping after the compressor also has an impact on the overall efficiency of the machine. By tuning the outlet piping correctly, noise and needed power can be reduced.

Inside the rotary positive-displacement machine, leakage flows play an important role. The various leakage flows determine the volumetric efficiency. For pumps the volumetric efficiency equals the overall efficiency, as there are virtually no other losses. For compressors, the leakage flows between compress-

ing chambers also determine largely the compression efficiency. As mentioned in the previous section, the leaking gas is the largest contributor in the heat transfer to the compressing gas, lowering the compression efficiency. Therefore it is necessary to minimize the leakages to obtain a good overall efficiency for rotary volumetric machines.

It is not possible to eliminate all leakages, as the machines consist in essence of rotors rotating in a stationary housing. The various leakage paths are determined by the geometry of the rotors and the casing of the machine. Thus a small change in the geometry of the rotors may have a large impact on the efficiency of the machine. Most of the research reported in literature is dedicated to this problem, usually applied to twin-screw compressor. However, most rotary volumetric machines currently in use were designed with an absolute minimal insight in the flow conditions inside these machines.

Experimentally, it is very difficult to obtain data inside a screw compressor, or for that matter any other rotary volumetric machine. The geometry of the machine is very closed and it is impossible to obtain velocity data of the flow inside. Pressures can be measured by placing sensors in the casing, but placing sensors on the rotors is more difficult. Temperature measurements are not possible, as the current temperature sensors are too slow in response for the high rotational speeds at which screw compressors operate (order 10000 rpm). Usually experimental measurements limit themselves to measuring the overall mass flow rate and possibly the outlet temperature for various pressure ratios. Examples of such measurements can be found in papers by Stosic et al [41, 43], Fujiwara [11], and Wu et al [53].

This means that there is no physical insight in the leakage flows and paths. Screw compressor profiles (of the rotors) are currently designed based on mathematical calculations. There are diverse methods for calculating the various leakage paths based on the geometry of the machine. The leakage flow following these paths is derived using rather crude models. Several examples of these models have been developed : by Deng and Shu [7], Sing and Onuschak [38], Singh and Schwartz [39], Singh and Bowman [36], Zhou [57], Zhang and Hamilton [56], Fong et al [10], Zaytsev [55] and Litvin [24].

These models were later on integrated in one-dimensional models. With these models the overall performance of a screw compressor can be studied rather accurately. Most recently, these one-dimensional models were combined with an optimization technique. This way, the profile of the screw rotors can be optimized to lower losses. Such an optimization model was introduced by

Stosic et al [43, 41, 40].

Nevertheless, such techniques still do not offer the least insight in the physical flow conditions inside the machine, and more particularly in the leakage flows. Computational Fluid Dynamics could offer valuable and interesting new information.

There are however difficulties with CFD in rotating positive-displacement machines. Because these machines deliver work by continuously expanding and reducing the volume of a working chamber, an immediate steady-state flow condition is never reached. When the process is time-converged, a steady-state cycle is reached. This means that stationary calculations are useless. Only the time-dependent calculation of an entire time-converged cycle is meaningful.

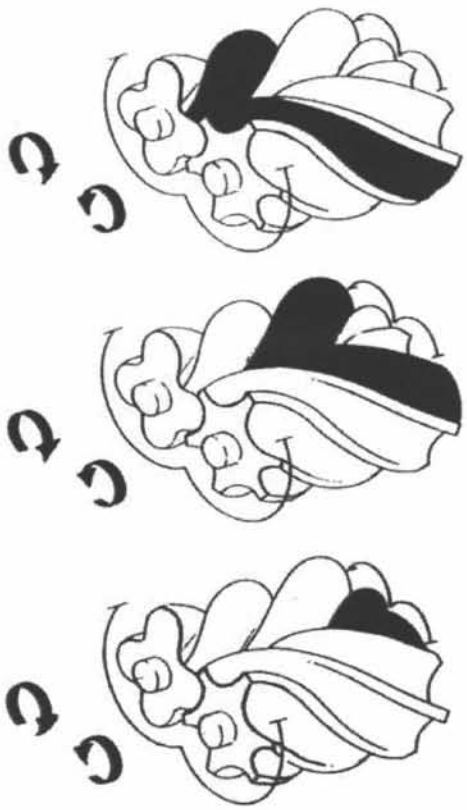

Figure 1.16: Evolution of the working chamber boundaries in a screw compressor during rotation

The problem is that during this cycle the rotors obviously rotate. As can be observed in figure 1.16, the boundaries of the flow domain move in a very complex manner. This is what has obstructed CFD calculation so far. Further complications arise when the fluid is compressible or when a second phase is present in the fluid (oil-injection). But these complications still allow simulations with the current state of technology.

Until now, very little CFD calculations in rotary volumetric machines have been published. Vimmr [51] has studied the leakage flow through the gap between the rotor and the housing of a screw compressor. But only the gap was modeled and the calculation was time independent. Bertrand et al [4] have modeled the flow in an extruder. This however is a very easy geometry and the flow is incompressible.

The most complete CFD calculation published so far, is by Kovasevic and Stosic [43, 42]. They have published an unsteady CFD calculation in a screw compressor with oil injection. But their method has certain shortcomings.

The grid Kovasevic and Stosic use for their flow calculations consists of two stationary blocks forming the inlet and the outlet port and two blocks of moving hexagonal grid forming the housing of the screw compressor. The hexagonal grid in the housing is generated by axially connecting two-dimensional rectangular grids in slices of the housing.

These two-dimensional rectangular grids are generated by an algebraic grid generator they developed.
First, the 2D domain is split in two to form the two blocks of grid. This is done based on the rack line of the screw profiles. The rack line is the screw profile for an infinite screw diameter. It can be shown that the rack line is identical for a matching male and female screw profile. Thus the rack line can be used to split the domain between the male and the female rotor.
Subsequently, each subdomain is meshed by an algebraic grid generator using transfinite interpolation. A resulting 2D grid is shown in figure 1.17.

The method developed by Kovacevic and Stosic is however developed completely dedicated to screw compressors. If no rack line can be defined for the rotors of the rotary positive-displacement machine, the method cannot be applied. Unfortunately this is the case for most rotary volumetric machines, with the exception of screw compressors and gear pumps.

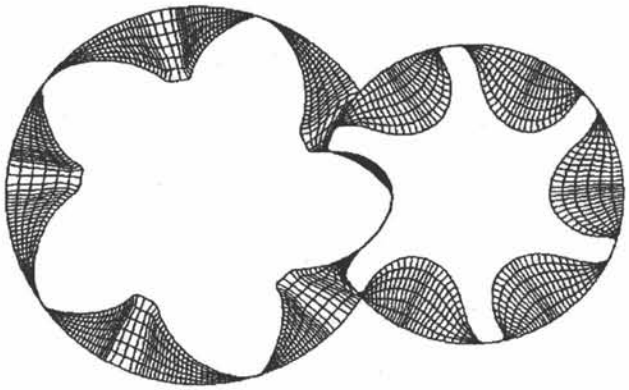

Figure 1.17: A 2D rectangular grid in a screw compressor housing slice as generated by Kovacevic and Stosic

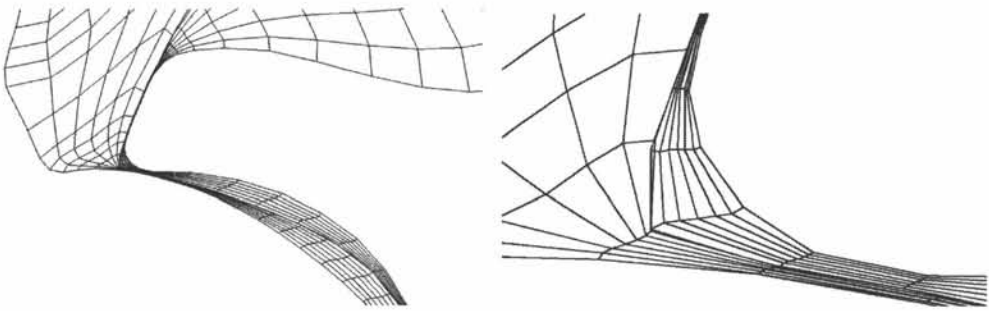

Figure 1.18: Blow-ups of a 2D rectangular grid in a screw compressor housing slice as generated by Kovacevic and Stosic

More importantly, the generated grids are of rather low quality in the gaps between rotors and between rotors and casing (cf. figure 1.18). There are cells with high aspect ratios, there are jumps in cell volume, there are skewed cells and in the zone of the meshing rotors, there are even cells of the two blocks that overlap. It in these zones where the grid is poor that the most important flow phenomena occur, namely the leakage flows. The quality of the grid in these zones may have a large impact on the value of the calculated results. No comparison of experimental and numerical results has been published in oil-free screw compressors, and only little in oil-injected screw compressors.

In this work, CFD method(s) are studied and developed that are generally applicable and that allow time dependent CFD in flow domains with complex moving boundaries such as encountered in rotary positive-displacement

machines. Special attention must be paid to the quality of the results in the various gaps.

Chapter 2

Computational Fluid Dynamics in Moving Geometries

In the first chapter of this book, rotary positive-displacement machines have been presented in general. The working principle of these machines has been explained. It has become clear that a deeper insight in the flow conditions in these machines is desirable. Computational fluid dynamics or CFD is a strongly favourable technique to obtain this insight, if certain problems associated with it can be addressed.

More specifically, there are two areas where more insight in the fluid flow could considerably further the development of these machines. Firstly, the inlet and the outlet ports of rotary positive-displacement machines are designed without exact knowledge of the flow patterns into and out of the casing of the machine. The geometrical form of these ports, and the tuning of the entire piping system after the outlet section in the case of compressors, are therefore not optimally designed. Secondly, the various leakage paths inside the machine as described in the previous chapter have not yet been studied properly. As explained in the previous chapter, reducing leakage flows raises both the volumetric and the compression efficiency.

It is impossible to obtain sufficient data from experiments to study these areas. CFD seems to be the only viable option. However, there is a serious problem associated with it.

Due to the positive-displacement principle on which these machines operate, only time dependent computations are meaningful. The simulation run should cover at least one time-converged displacement cycle. The problem this raises is that during this run time, the boundaries of the flow domain (in specific the rotor surfaces) move in a geometrically complex manner through the flow domain.

Ample research has been performed and reported for CFD calculations with moving boundaries in turbo machinery and piston machinery. In rotary volumetric machines, the movement of the boundaries is however much more complex.

The solutions developed for turbo machinery are not applicable here. They all rely on the possibility to split the flow domain in two subdomains that have a common and stationary interface (cf figure 2.1). In figure 2.1, one can distinguish a sub-domain associated with the rotor and a sub-domain consisting of the rest of the flow domain. The interface between both is a cylinder mantle (or a circle in two dimensions). The sub-domain attached to the impeller can be allowed to rotate around the same axis as the impeller. The interface between both does not change in time. The calculation domain consists of a cylindrical grid block rotating inside a second grid block with a cylindrical hole. The only difficulty with such calculations lies in handling the data transfer of flow properties across the interface. This problem has been studied extensively.

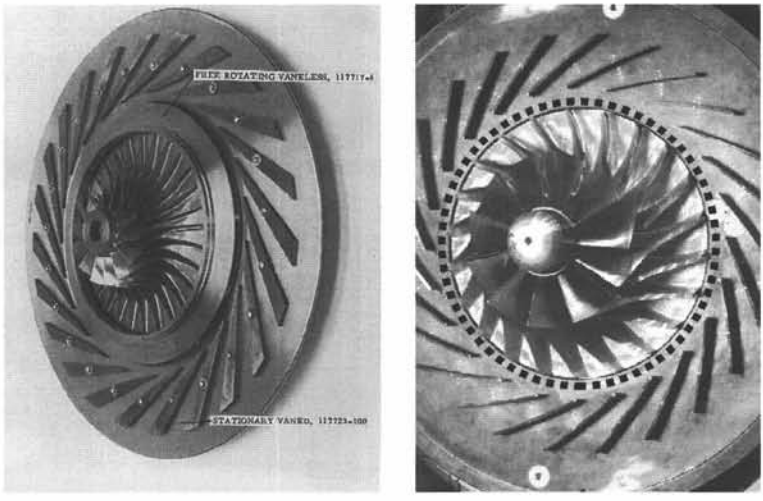

Figure 2.1: Stator and impeller of a turbo pump; a possible division into 2 domains is presented in dashed line on the right picture

The three most applied methods for flow calculations in turbo machinery are the mixing plane method, the multiple reference frames method and the sliding meshes method (which is the only fully time dependent). For further analysis reference is made to [46] and general literature.

In the case of rotary positive-displacement machines it is not possible to find a division of the flow domain in two (or more) subdomains with a common stationary interface. As is illustrated in figure 2.2, if the flow domain were split into two blocks associated to each rotor, the interface between these two blocks would have to move in time. This makes the above-mentioned methods unusable.

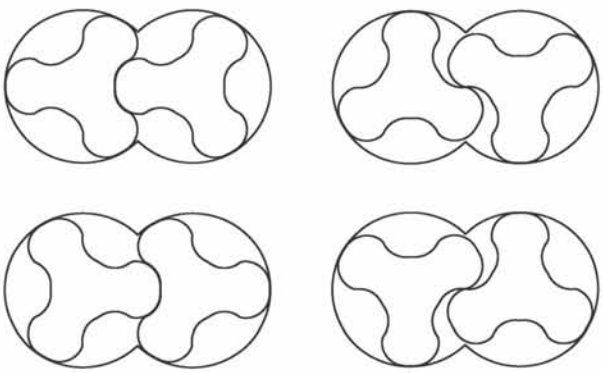

Figure 2.2: Typical lobe pump geometry

There are two methods in CFD that can be applied to a geometry with the complexity encountered here.

The first is a set of techniques designated Fictitious Domain Techniques. The defining characteristic of these methods is that not all boundaries physically present in the flow domain are incorporated as such in the calculation flow domain. By adapting the flow equations, the influence of the ignored boundaries on the flow is simulated. For the problem at hand this would mean that the rotor surfaces are not incorporated in the calculation domain. The entire inside of the machine housing would be gridded and the effect of the moving rotor surfaces on the flow would be substituted by changes in the flow equations. This would remove the problems associated with the moving boundaries in the flow domain.

However, these techniques have never been applied to compressible flow. Another drawback is that it is very difficult to obtain a sharp fluid-solid inter-

face at the boundary that is lifted from the calculation domain. The effects of the rotor surfaces on the flow, even if adapting the flow equations can simulate them, are always smeared out to some degree over a span of several grid cells. This means that the fictitious domain technique is not optimal for studying the various leakage flows near the rotors. After all, to obtain a picture of the flow between two walls, it is imperative that both boundaries are sharp. Nevertheless, this could be a technique that can be used to study the flow conditions at the inlet and outlet of the machine.

A different approach is to adapt the calculation grid as the rotors move through the flow domain. In this case the Arbitrary Lagrangian Eulerian (ALE) formulation of the flow equations has to be used. This formulation allows the grid nodes to move freely during the simulation. There are only two limitations : at each time step the grid must be of sufficient quality to allow spatial discretization (as is the case for stationary grids) and the cell definitions (the grid topology) must remain unchanged. The latter means in practice that only the grid nodes may be moved (cf. figure 2.3). The ALE formulation of the flow equations can be incorporated in a flow solver mathematically correct (no supplementary approximations) and essentially without great complications. At this time, several commercial CFD codes already offer this possibility. The problem is thus in se shifted to developing a robust grid manipulation algorithm that can move the grid during the simulation run, whilst maintaining the grid cell definitions and the grid quality.

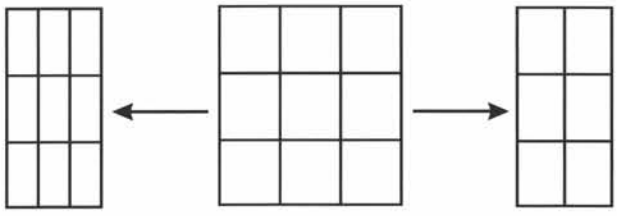

Figure 2.3: Grid movement; left : maintaining grid topology; right : loosing grid topology

If after a certain amount of time steps the calculation grid were to be so severely distorted and degraded in quality as to make calculations difficult, it is always possible to regrid the flow domain. The flow parameters then have to be interpolated from the old grid to the new grid and ALE calculations are resumed with this new grid. This interpolation or remapping of the flow parameters introduces numerical inaccuracies that have to be avoided as much as possible. The goal is to develop a grid manipulation algorithm that is powerful enough to make interpolations unnecessary.

In the remainder of this chapter, the Fictitious Domain method and the Arbitrary Lagrangian Eulerian method are described more in detail.

2.1 Fictitious Domain Methods

The Fictitious Domain (FD) Method is an interesting method of flow calculation for domains where mesh generation is not straightforward. This method has been reported in literature to be able to simulate flow in open domains with incompressible fluids relatively well.

The 'Fictitious Domain Method' is a name for several CFD techniques that have as common feature that in the fluid domain parts of the real geometry are not present as boundaries, yet the effect of these immersed or fictitious boundaries on the fluid flow is simulated by altering the flow equations.

Consider a domain Ω and a subdomain ω with boundaries $\partial\Omega$ and $\partial\omega$ as visualized in figure 2.4. Ω/ω is the fluid part of the domain and ω is the solid part. In Ω/ω the flow is defined by the Navier-Stokes equations with appropriate boundary conditions.

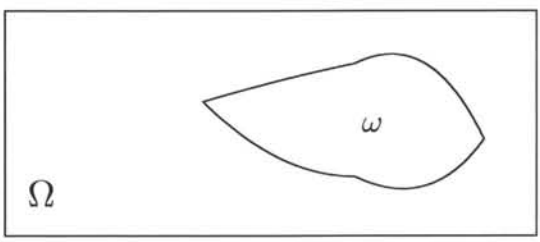

Figure 2.4: A domain Ω with subdomain ω.

Classically, to perform a CFD calculation in the flow domain of figure 2.4, the subdomain Ω/ω would be furnished with a calculation grid. The Navier-Stokes equations would be approximated by a spatial discretization on the calculation grid that can be solved mathematically.

In FD methods, the Navier-Stokes equations are extended to the entire domain Ω and the entire domain is spatially discretized with a calculation grid.

The boundary conditions at $\partial\Omega$ are explicitly imposed. In ω, the Navier-Stokes equations are adapted to provide flow conditions at the immersed boundary $\partial\omega$ equaling as much as possible the desired boundary conditions.

For all research reported until present day, the immersed boundary is always a wall boundary. It is shown in [8] that if the method succeeds in imposing the desired wall velocity and impermeability of the immersed boundary, the actual flow conditions in ω have no effect on the flow conditions in the physical flow domain Ω/ω.

The idea behind the Fictitious Domain methods was conceived in the late sixties and the early seventies by various investigators of the Marchuk-Yanenko school of Numerical Mathematics at Novosibirsk. The method was mainly aimed at steady flow calculations in geometrically complex domains. At that time it was far from self-evident to generate a good calculation grid in complex flow domains.

Since then, many new powerful grid generation techniques have been developed. These new techniques, using the expansion in computational power of the last years, have made Fictitious Domain methods obsolete for steady flow calculations. More recently, the Fictitious Domain principle has been rediscovered to calculate unsteady incompressible flow in domains with moving geometries. The method is particularly advantageous for fluid-structure interaction. The movement of the (immersed) boundary is not known a priori, but the flow forces themselves drive the movement. A well-known example is the calculation of blood flow past a heart valve by Peskin [32]. In the last decade, a lot of research has been reported in this domain.

At the moment, there are four different techniques that qualify as Fictitious Domain techniques. They are the Lagrange Multiplier Fictitious Domain (LMFD) method, the Cartesian Grid method, the Immersed Interface or Immersed Boundary method and the Penalty Force Fictitious Domain (PFFD) method. Although not all techniques published carry one of these names, they in essence all fall in one of these four categories.

2.1.1 Lagrange Multiplier Fictitious Domain (LMFD) method

The first technique is the Lagrange Multiplier Fictitious Domain (LMFD) method, of which Glowinsky is a prominent developer [12, 30, 31, 37]. In this method, the Navier-Stokes equations, which are valid in the fluid domain Ω,

are combined with boundary conditions on the fictitious boundaries $\partial\omega$ in a variational form with the use of a Lagrange multiplier.

The incompressible flow equations

$$\nabla \cdot \vec{u} = 0 \tag{2.1}$$

$$\frac{\partial \vec{u}}{\partial t} - \nu \Delta \vec{u} + (\vec{u} \cdot \nabla)\, \vec{u} + \frac{\nabla p}{\rho} = \vec{f} \tag{2.2}$$

Boundary conditions

$$\vec{u}\,(\vec{x}, 0) = \vec{u_0}\,(\vec{x})\,,\ \vec{x} \in \Omega \setminus \omega \tag{2.3}$$

$$\vec{u} = \vec{g_0} \quad \text{on } \partial\Omega \tag{2.4}$$

$$\vec{u} = \vec{g_1} \quad \text{on } \partial\omega \tag{2.5}$$

Functional Spaces

$$V_{g_0(t)} = \left\{ \vec{v} \mid \vec{v} \in \left(H^1(\Omega)\right)^d,\ \vec{v} = \vec{g_0}\,(t) \text{ on } \partial\Omega \right\} \tag{2.6}$$

$$V_0 = \left(H_0^1(\Omega)\right)^d \tag{2.7}$$

$$L_0^2(\Omega) = \left\{ q \mid q \in L^2(\Omega)\,;\ \int_\Omega q d\vec{x} = 0 \right\} \tag{2.8}$$

$$\Lambda(t) = \left(H^{-1/2}(\gamma(t))\right)^d \tag{2.9}$$

Consider $\vec{U_0}$ (resp. $\tilde{\vec{f}}$) such that $\vec{U_0} = \vec{u_0}$ (resp. $\tilde{\vec{f}} = \vec{f}$) in $\Omega \setminus \omega$ and $\nabla \cdot \vec{U_0} = 0$. It can be shown that this problem is equivalent to :

For $t \geq 0$, find $\{U(t), P(t), \lambda(t)\} \in V_{g_0(t)} \times L_0^2(\Omega) \times \Lambda(t)$ such that

$$\int_\Omega \frac{\partial U}{\partial t} \cdot \vec{v} d\vec{x} + \nu \int_\Omega \nabla U \cdot \nabla \vec{v} d\vec{x} + \int_\Omega (U \cdot \nabla) U \cdot \vec{v} d\vec{x} \tag{2.10}$$

$$- \int_\Omega P \nabla \cdot \vec{v} d\vec{x} \tag{2.11}$$

$$= \int_\Omega \tilde{\vec{f}} \cdot \vec{v} d\vec{x} + \int_{\partial\omega} \lambda \cdot \vec{v} ds, \forall \vec{v} \in V_0 \tag{2.12}$$

$$\nabla \cdot U(t) = 0 \tag{2.13}$$

$$U(0) = U_0 \tag{2.14}$$

$$U(t) = g_1 \text{ on } \partial\omega \tag{2.15}$$

This multiplier λ can be physically interpreted as the force on the fictitious boundary. It can be shown that λ is the jump of $\nu \frac{\partial \vec{U}}{\partial \vec{n}} - \vec{n}p$ at the immersed boundary

A further version of the LMFD method that allows direct numerical simulation of fluid-structure interaction with moving boundaries is the Distributed Lagrange Multiplier Fictitious Domain method. In a first step the flow inside the subdomain ω is constrained to be a rigid body motion:

$$\frac{1}{2}\left(\nabla \vec{u} + \nabla \vec{u}^T\right) = 0$$

This constraint is coupled with the flow equations using a variational form. To do this a field Λ of well-chosen Lagrange multipliers is needed (instead of a single λ). It can be shown that this field Λ can be physically interpreted as the stress inside the solid domain. Using this viewpoint it can be analogously shown that the pressure is a field of Lagrangian multipliers enforcing the incompressibility constraint.

In a similar manner, other constraints expressing the movement of the solid subdomain (such as rotation, elastic deformation etc) can be coupled with the flow equations in a variational form using a field Λ of Lagrange multipliers.

This technique has been applied to the sedimentation of particles in incompressible fluid [12, 31, 37], DNS simulation of a heart valve [2] and the flow in a stirred reactor [3].

Although this is a powerful technique for incompressible flow with fluid-structure interaction, there are drawbacks. Firstly, the extra constraint, be it a simple boundary condition or some more complex constraint, has to be decoupled from the classical flow equations to solve the problem numerically. It is not straightforward to do this. Several operator-splitting techniques have been published, but there is no clear favorite. In any case, it is not possible to incorporate this method in a commercial CFD package.

More fundamentally, it is not immediately clear how this method is extended to compressible flows.

2.1.2 Cartesian Grid method

A second technique is the Cartesian Grid Method [45, 54]. The governing equations are discretized on a Cartesian grid that does not conform to the immersed boundaries. The location of the immersed boundary is tracked in time by calculating the position of several control points. Then the immersed boundary is approximated piece-wise linearly (figure 2.5).

At the immersed boundary the spatial discretization is done in a special manner. The effect of this special discretization is that here the flow equations are calculated using irregular (typically trapezoidal) cells (figure 2.5). The immersed boundary thus coincides with faces of (fictitious) grid cells. By imposing the correct boundary conditions at these faces, the effect of the immersed boundary on the fluid can be simulated. Notice that the Cartesian Grid method is the only Fictitious Domain technique that shows a sharp interface between fluid and solid.

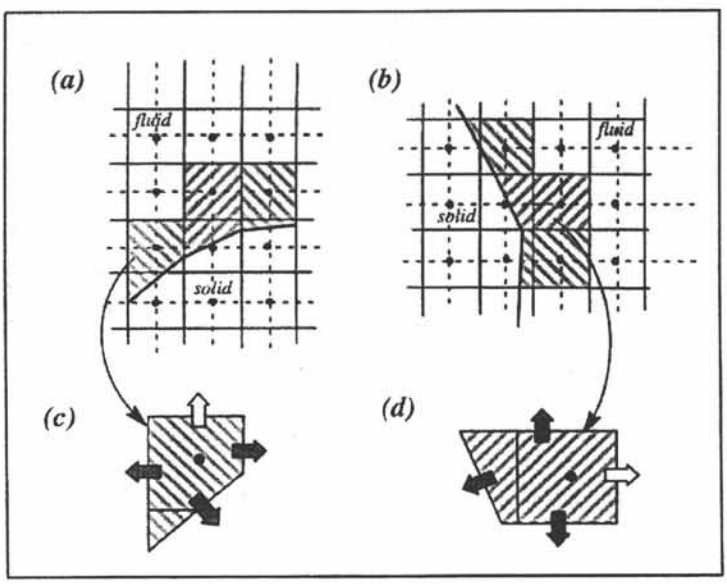

Figure 2.5: Trapezoidal cells as a result of the Cartesian Grid method

Although the principle idea behind the Cartesian Grid method is simple, implementing this idea raises several problems. The special spatial discretization at the immersed boundary can become complex. Besides this, at the cell faces that form the immersed boundaries, fluxes and gradients need be obtained to solve the flow equations. But these cells have an irregular form and

they have neighbouring cells that are situated in the solid subdomain, which obviously contain no valid data concerning the fluid flow. The fluxes and gradients at the immersed boundary therefore cannot be obtained in the normal manner, but have to be interpolated based on fluxes and gradients obtained in neighbouring cells in the fluid subdomain.

If the immersed boundary moves, imposing the correct boundary conditions is not obvious. The wall boundary condition is transformed into imposing a pressure gradient (aka a force), because this is a moving wall in a stationary grid. This is different from wall boundaries in body-fitted grids, where the wall moves together with the grid. Furthermore, conservation of mass has to be explicitly imposed at the immersed boundary. In [45, 54] this is done by adequately adapting the intermediate velocity field in the pressure correction scheme.

The largest problem however is how to handle the so-called 'freshly cleared cells'. As the immersed boundary moves through the stationary grid, there will be cells that at a specific time step become part of the fluid subdomain, while they were inside the solid subdomain the previous time step (figure 2.6). These cells are called 'freshly cleared'. They have no history as a fluid before they were cleared. This is of course a difficulty for the time discretization. In [45, 54] this problem is solved by interpolating the velocity in a freshly cleared cell based on the neighbouring fluid cells. As the flow is incompressible, the pressure field follows from the velocity field and thus the problem is handled.

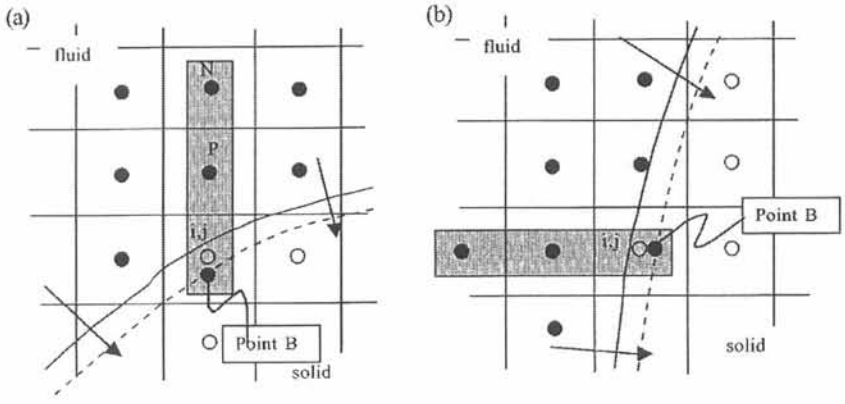

Figure 2.6: Freshly cleared cells in the Cartesian Grid method

The sharply defined interface and the benefits in terms of computational efficiency of Cartesian grids are responsible for increasing popularity. Flow

calculations have been reported in a geometry as complex as a two-dimensional diaphragm piston compressor.

2.1.3 Immersed Interface or Immersed Boundary method

A third technique is the Immersed Interface or Immersed Boundary method (II/IB). This technique was developed by Peskin [32, 19, 16, 25, 33, 58, 18, 23, 6, 13] and adopted by Le Veque and Li [21]. In this technique, the interaction force exercised by the immersed (fictitious) boundary is explicitly added to the Navier-Stokes equations :

$$\nabla \cdot \vec{u} = 0 \tag{2.16}$$

$$\rho \frac{\partial \vec{u}}{\partial t} - \mu \Delta \vec{u} + \rho(\vec{u} \cdot \nabla)\vec{u} + \nabla p = \vec{f} \tag{2.17}$$

$$\int_{\partial\omega} \vec{F}(s,t) \cdot \delta\left(\vec{x} - \vec{X}(s,t)\right) ds = \vec{f}(\vec{x},t) \tag{2.18}$$

where $\vec{X}(s,t)$ is a point on $\partial\omega$, defined by time t and curve parameter s.
$\vec{F}(s,t)$ is a definition of the force exercised by the flow on $\partial\omega$.

In theory, the force $\vec{F}(s,t)$ should be applied to the fluid using a Dirac delta function δ in order to obtain a sharp solid-fluid boundary. In practice, a Dirac delta function is not feasible, both because of the spatial discretization and for numerical reasons. In practice, a discrete approximated Dirac function is used, called a delta function in mathematics. This discrete delta function is spread over several cell widths (typically 3 or 4). Because of this, the solid-fluid interface is smeared out.

There are several different choices of delta functions that can be used. Each gives rise to a new II/IB method [5, 19, 21, 22, 35]. However, whatever the chosen delta function, a loss of accuracy near the immersed boundary seems inevitable. Adaptive refining moving with the boundary through the grid ameliorates the accuracy, but also makes the implementation more complicated.

Because of the explicit introduction of the interaction force in the flow equations, this method always implies fluid-structure interaction (FSI). This naturally integrated form of fluid-structure-interaction can be an advantage

when FSI is desired. However, it also means that problems specifically related to fluid-structure interaction calculations have to be dealt with (such as the distinction between strongly and weakly coupled interaction etc.). When the movement of the immersed boundary is known a priori, the II/IB method is not usable.

All calculations with the II/IB method that have been published include fluid-structure interaction. As Peskin was a major developer of the code, a lot of calculations in biomedical applications are known. A calculation of compressible flow is not yet published.

2.1.4 Penalty Force (PFFD) Fictitious Domain method

The fourth technique is the Penalty Force (PFFD) technique [8, 17]. This method is similar to the Immersed Interface/Immersed Boundary method. In essence it also consists of applying a force to the fluid at the immersed boundary. The difference is that in this method, the force applied is not the physical interaction force, but a penalty force. In this method the velocity of the immersed boundary is known a priori and the penalty force locally forces the velocity at the immersed boundary to be the desired velocity $\vec{v}_D$. The penalty force is the velocity difference $(\vec{v}_D - \vec{v})$ multiplied by a large constant.

The flow equations for incompressible flow thus are :

$$\nabla \cdot \vec{u} = 0 \tag{2.19}$$

$$\frac{\partial \vec{u}}{\partial t} - \nu \Delta \vec{u} + (\vec{u} \cdot \nabla)\, \vec{u} + \frac{\nabla p}{\rho} = C \cdot (\vec{v}_D - \vec{v}) \tag{2.20}$$

In (2.20) C is a large constant.

If the local fluid velocity $\vec{v}$ were to exactly match the desired velocity $\vec{v}_D$, the penalty force would be zero. In that case there would be no force to ensure that $\vec{v}_{\partial\omega} = \vec{v}_D$, so this is not possible. The situation described is the limit towards which the calculation converges, yet never reaches.

This has two important consequences. Firstly, it means that the desired velocity boundary condition can never be exactly imposed. If the constant C in (2.20) is chosen large, the velocity deviation will be small. From this viewpoint, C should be as large as possible (still allowing numerical stability).

On the other hand, as the velocity boundary condition is never exactly imposed, there is always a penalty force acting on the fluid. As the velocity field is locally enforced (by the penalty force), the penalty force acts on the pressure field. This penalty force has no physical meaning, and thus locally causes an abnormality in the pressure field. If the constant C in (2.20) is small, the penalty force and by consequence the abnormality in the pressure field will be small. From this viewpoint it is important to choose C as small as possible.

The exact choice of the value of C in (2.20) therefore has to be made contemplating both consequences above. It is usually a case-specific trade-off. It should be noted that in principle it is possible to choose C in such a manner that the resulting penalty force is in fact the physical force acting on the fluid. However, this implies a fluid-structure interaction calculation. The Penalty Force method is then a special case of an Immersed Interface/Immersed Boundary method.

Finally three more small remarks have to be made. In principle, the penalty force should be a surface force acting on the immersed boundary through a Dirac function. Just as described for the Immersed Interface/Immersed Boundary method, this is not feasible and a delta function has to be used smearing the force over at least one cell.

If the energy equation of the Navier-Stokes equations is calculated, the influence of the penalty force must be added to the energy equation the same way as any other body force. For incompressible flow, the energy equation is decoupled from the momentum equation and the continuity equations. As the penalty force is not physical, its energy-term in the energy equation locally causes an abnormality in the temperature field, just as the force itself does in the local pressure field.

Finally, it should be noted that for incompressible flow, a velocity constraint on the immersed boundary is sufficient as wall boundary condition, if the velocity constraint expresses a rigid-body motion. After all, for a rigid-body motion the velocity constraint fulfills the condition :

$$\oint_{\partial\omega} \vec{u} \cdot d\vec{S} = 0 \tag{2.21}$$

Therefore the impermeability of the wall is automatically ensured with a constant density ρ :

$$\oint_{\partial\omega} \rho\vec{u} \cdot d\vec{S} = 0 \tag{2.22}$$

2.2 Arbitrary Lagrangian Eulerian Method

The Arbitrary Lagrangian-Eulerian method is a time-dependent CFD method that allows the calculation grid to deform during the calculation. It is a mix between the Lagrangian and the Eulerian methods (hence the name) [14].

In the Eulerian method, the calculation grid is stationary. The flow equations are the general equations (2.23)-(2.25).

conservation of mass

$$\frac{\partial}{\partial t}\int \rho dV + \int \rho \vec{u} \cdot d\vec{S} = 0 \tag{2.23}$$

conservation of momentum

$$\frac{\partial}{\partial t}\int \rho \vec{u} dV + \int \rho \vec{u}\vec{u} \cdot d\vec{S} = \int -p \cdot d\vec{S} + \int \vec{\bar{\tau}} \cdot d\vec{S} \tag{2.24}$$

conservation of energy

$$\frac{\partial}{\partial t}\int \rho E dV + \int \rho E \vec{u} \cdot d\vec{S} = \int -p\vec{u} \cdot d\vec{S} + \int \left(\vec{u} \cdot \vec{\bar{\tau}}\right) \cdot d\vec{S} \tag{2.25}$$

It obviously is not hampered by tangling grids, but is incapable of representing moving domain boundaries.

The Lagrangian method is a time-dependent CFD method in which the calculation grid moves with the local fluid velocity. A serious disadvantage of the Lagrangian method, however, is that the grid is very prone to grid entanglement. After all, the calculation grid is directly linked to the local flow velocity and the quality of the moving grid is in no way guaranteed. In multi-dimensional problems, especially when vortices occur, the degradation of grid quality is so rapid and grave that the Lagrangian method is unusable.

The ALE method is a mix of the Lagrangian and the Eulerian method in that it allows the grid to move with a velocity that is independent from the flow solution. The flow equations with an unspecified boundary velocity become :

geometric conservation law

$$\frac{\partial}{\partial t}\int dV - \int \vec{u_b}\cdot d\vec{S} = 0 \tag{2.26}$$

conservation of mass

$$\frac{\partial}{\partial t}\int \rho dV + \int \rho\left(\vec{u}-\vec{u_b}\right)\cdot d\vec{S} = 0 \tag{2.27}$$

conservation of momentum

$$\frac{\partial}{\partial t}\int \rho\vec{u}dV + \int \rho\vec{u}\left(\vec{u}-\vec{u_b}\right)\cdot d\vec{S} = \int -p\cdot d\vec{S} + \int \vec{\bar{\tau}}\cdot d\vec{S} \tag{2.28}$$

conservation of energy

$$\frac{\partial}{\partial t}\int \rho E dV + \int \rho E\left(\vec{u}-\vec{u_b}\right)\cdot d\vec{S} = \int -p\vec{u}\cdot d\vec{S} + \int \left(\vec{u}\cdot\vec{\bar{\tau}}\right)\cdot d\vec{S} \tag{2.29}$$

By adding the boundary velocity to the flow equations, an extra unknown is introduced. To solve the flow equations in ALE formulation the velocity of the boundaries of the control volumes must be known for each time step. An additional equation is necessary to close the set of equations. The additional equation is the space conservation law or geometric conservation law (2.26).

The space conservation or geometric conservation equation in essence expresses the conservation of volume. It is decoupled from the other flow equations and can be solved separately. Often this equation is discretized exactly, without truncation term, although this is not necessary [20, 9].

In principle, there are no important problems connected with the implementation of the ALE flow equations in a flow solver. Several commercial CFD codes offer the possibility to perform ALE calculation. In this research it is opted to use a commercial CFD code as a black box to perform the flow calculation. Instead the focus lies on the manipulation of the grid.

There are only two limitations for the movement of the grid. Firstly, it must be possible to discretize the equations (2.26)-(2.29) spatially on the calculation grid at each time step. This means that the grid must be of sufficient quality at each time step. The quality restrictions (no negative volumes, low aspect ratios, skewing of the cells, ...) are no more stringent than for a normal (Eulerian) calculation.

The equations must also be discretized in time. Although a cell may deform and move between time steps, its definition must be the same. During the run the grid topology has to be maintained. Each cell of the calculation grid has to be defined by the same faces and vertices. In practice, this means that the only allowed manipulation of the grid, is moving the vertices freely.

In principle it is possible to use the Arbitrary Lagrangian Eulerian formulation of the flow equations to calculate the flow parameters from one time step to the next. At this next time step, the flow domain could be regridded and the flow parameters on the new grid could be obtained though interpolation of the flow parameters obtained from the ALE time step. After doing this, a new time step could be calculated using the ALE formulation on the new grid. This method would allow for a certain degree of grid quality degradation, as the bad quality grid is replaced by one of better quality. However, the interpolation of flow parameters between two grids introduces inaccuracies in the method that are best avoided. If the grid topology is maintained during the entire run, the ALE flow equations can be solved time-dependently without need for remapping or flow data interpolation between time steps.

Chapter 3

Fictitious Domain Calculations

In chapter 2, two techniques were presented that could allow computational fluid dynamics calculations of flow through rotary positive-displacement machines. In this chapter the application of fictitious domain techniques is described. It will be shown that this technique can be used for incompressible flow (pumps), but with certain limitations. For compressible flow, the method does not work. This research has been published in the Journal of Computational and Applied Mathematics [50].

3.1 Incompressible flow

There exist four methods that can be labeled fictitious domain technique. These are the Cartesian Grid method, the (Distributed) Lagrange Multiplier Method, the Immersed Boundary or Immersed Interface Method and the Penalty Force Method. All these techniques have been exclusively developed and researched for incompressible flow. At the time of this study, no calculations were published of incompressible flow inside a machine. Most simulations were of so-called open flows. The pressure gradients occurring in the flow field are relatively small.
Examples are the settling of small objects in fluid, the movement of a valve in a general pipe flow etc.

For the calculation of flow through a rotary positive-displacement pump, the fictitious boundary should consist of the rotor surface. Larger pressure gradients will occur in the flow field, which are entirely the consequence of the motion of the fictitious boundary. Its influence is much more important.

To study the use of a fictitious domain technique, the Penalty Force Fictitious Domain method is chosen. This method is chosen because it is relatively easy to implement in a commercial CFD code. The implementation of the Lagrange Multiplier method or the Cartesian Grid method would imply the development of a flow solver in which these techniques are embedded. As the flow domains this study is aiming at are three-dimensional, the development of such a solver would be a serious investment of time. It is opted to first study the technique using a rough fictitious domain method implemented in a commercial CFD code and draw conclusions from this study.

The commercial CFD code used is FLUENT version 5.4. Through the use of user-defined memory and functions and a user-defined impulse source term a rough version of the PFFD technique is implemented.

FLUENT is a co-located cell centered CFD code. This means that all flow parameters are stored in the cell centers of the calculation grid. As the object is to have fictitious boundaries at the rotating rotor surfaces, it should be determined at each time step whether a cell center is located inside a rotor. If it is, a penalty force is applied to this cell to force the velocity to conform a rigid-body motion. By consequence, the immersed boundary does not conform very well geometrically to the rotor surface (cf figure 3.1). In this sense, the applied technique is rough. There have been studies reported in literature on how to make the immersed boundary conform more to the real boundary using mass sources and sinks [27]. However, it is opted not to incorporate these complications in this first study.

For a preliminary study, the geometry of a lobe pump is chosen (cf figure 3.2). Each rotor has three lobes. It is possible to perform the calculation two-dimensional. The geometry shown in figure 3.2 is generic. It is not an existing lobe pump and therefore there are no experimental results to compare with. However, as the lobe pump is a positive displacement pump, the theoretical mass flow can be readily determined. The calculated mass flow rates can be compared with this leakage-free mass flow rate.

The entire housing of the lobe pump is meshed with an unstructured grid using FLUENT's preprocessor GAMBIT. Figure 3.1 is an illustration.

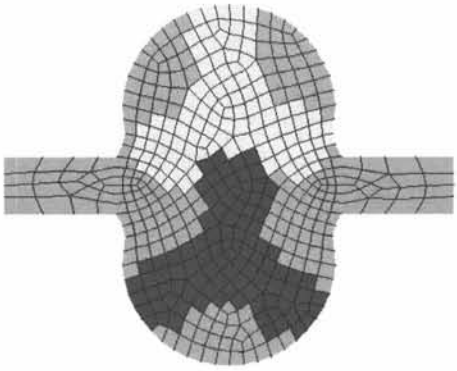

Figure 3.1: Immersed boundary of a lobe pump on a coarse grid (435 cells)

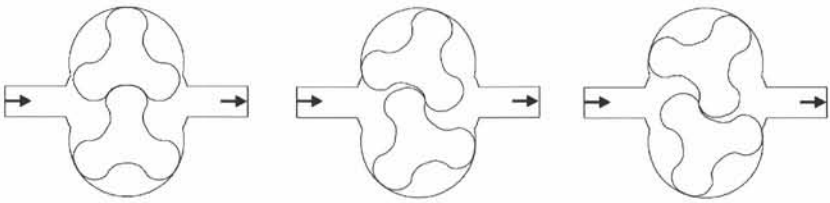

Figure 3.2: Working principle of a lobe pump

The FLUENT code is extended with two user-defined functions. The first user-defined function determines whether a grid cell center is located in one of the rotors. This function is a simple algorithm based on the following mathematical property :

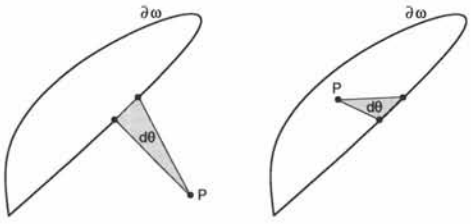

Figure 3.3:

Be $\partial\omega$ a two-dimensional closed curve and be θ the angle between two points on $\partial\omega$ separated by an infinitesimal arc length ds seen from a point P as illustrated in figure 3.3. Then the integral $\oint_{\partial\omega} d\theta$ over the entire curve $\partial\omega$ is 0 if P lies outside the curve $\partial\omega$ and 2π if P lies inside the curve $\partial\omega$.

For the lobe pump, the rotors are defined as a list of x and y coordinates of points on the surface of the rotor.

The sum Σ of all oriented angles $\hat{\theta}$ between consecutive points in the list, as seen from a cell centre C, is a discretized approximation of the fore-mentioned integral. A cell-center C is considered to be located inside a rotor if the sum Σ is more than π.

This simple algorithm is called for each cell in the grid. The result is stored in user-defined memory. Figure 3.1 shows the result of this user-defined function for a coarse grid. Figure 3.4 shows the result on a more realistic (finer) grid.

Comparing figure 3.1 and figure 3.4, the influence of grid refinement on calculation results is immediately obvious. If the calculation grid is more refined, the surface of the fictitious rotors will geometrically conform more to reality. For the very coarse grid shown in figure 3.1, the gaps aren't even resolved and there would be no leakage. As mentioned above, recently some studies have been published on how to place the fictitious boundary through

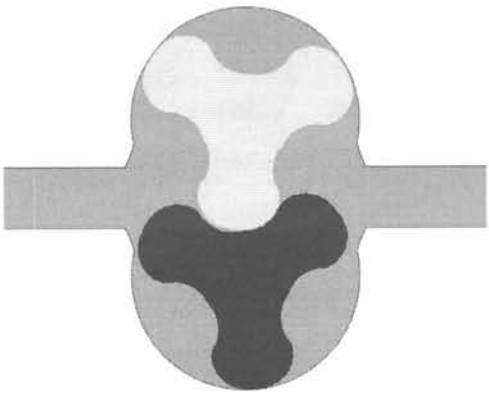

Figure 3.4: Immersed boundary of a lobe pump on a fine grid (22191 cells)

cells instead of following the cell faces (edges in 2D). This is done through the use of mass sources and sinks, but is not implemented here. In any case, the influence of grid refinement on the calculation results is one of the things that will have to be studied.

After the call of the first user-defined function, a second one is called to determine the penalty force. As outlined in chapter 2, this penalty force should be introduced as a singular force at the immersed fictitious boundary using a Dirac delta pulse to be physically the most correct. As also outlined in the previous chapter, this is numerically impossible due to the spatial discretization. In literature, several alternative delta functions have been put forth spanning three or more cell widths.

In this preliminary study, it is opted to introduce in each cell with its centre inside a rotor a body force of the form

$$\vec{F_p} = -C_0 \cdot (\vec{v}_{rigid} - \vec{v}) \tag{3.1}$$

In (3.1) C_0 is a large constant. $\vec{v}_{rigid}$ is the rigid-body velocity of the rotor :

$$\vec{v}_{rigid} = \vec{\omega} \times \vec{r} \tag{3.2}$$

This is not the most refined method, but it allows studying the influence of the constant C_0 on the calculation results. As outlined in the previous chapter, a large constant will result in a velocity field that conforms strongly to the rigid-body motion of the fictitious boundary. A deviation of this correct velocity field not only results in errors in the velocity field, but also in loss of impermeability of the fictitious boundary. On the other hand, the size of the penalty force, which physically has no real meaning, is linear with the constant C_0. Thus a small constant C_0 is desirable to obtain a physically more correct pressure field.

Finally, it should be mentioned that there are no consequences to applying a penalty force to all cells with their center inside a rotor, instead of only those cells cut by the fictitious boundary. If the boundary conditions at the location of the fictitious boundary can be enforced, the flow field in the sub-domain formed by the rotors can have no influence on the flow field in the physical flow domain. Literature confirms this [8].

3.1.1 Influence of grid refinement and penalty force strength

Before performing a time dependent calculation of flow through the lobe pump, the influence of the grid size and the size of the constant C_0 has to be determined. To do this, the rotors are frozen in a fixed position and a time steady calculation is performed for several grid sizes and constants C_0. For each of these calculations, the mass flow rate is determined. As the rotors are frozen and as the lobe pump is a positive-displacement pump, these mass flow rates have no real physical meaning. However, they can be used to assess the influence of grid size and constant C_0, while saving valuable computing time.

In figure 3.5, the mass flow rate is displayed versus the constant C_0 for frozen rotor calculations on several grids. These grids are : a triangular grid of 783 cells, a rectangular grid of 4196 cells, a triangular grid of 12836 cells, the triangular grid of 783 cells refined on pressure gradient to 7834 cells and the rectangular grid of 4196 cells refined to 10038 cells and once more refined to 24750 cells.

From a certain value on, the results are independent of the value of the constant C_0 (around 10^{11}). This means that the boundary condition at the fictitious boundary is as well enforced as can be for a constant C_0 of 10^{11}. Higher values do not enforce the velocity constraint any better. They just result in higher penalty forces, and thus larger (unphysical) pressure gradients.

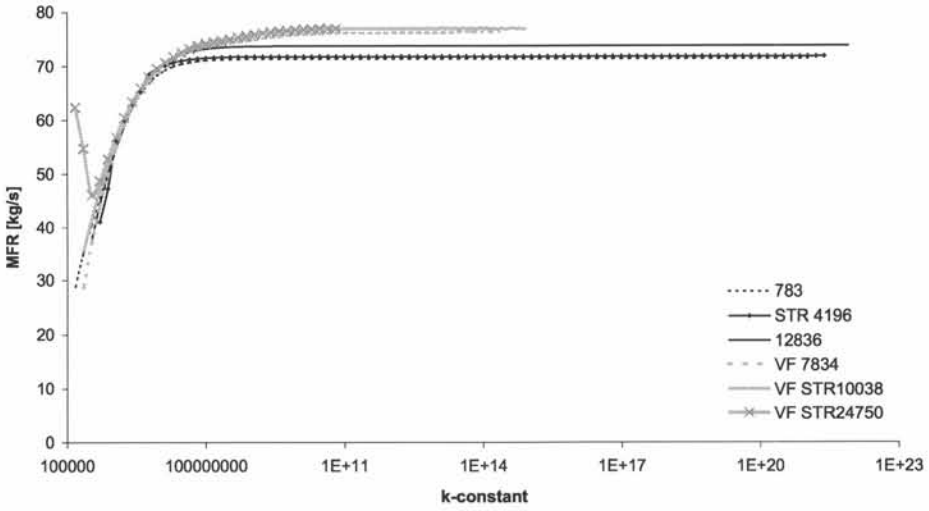

Figure 3.5: Plot of MFR versus penalty force strength C_0 (k-constant) on various grids

From figure 3.5, the dependence of the results on the coarseness of the grid can also be evaluated. Only on the grids refined on pressure gradients a mass flow rate is obtained that is grid independent. Further refinement does not lead to a better result, which illustrates grid independence.

It is important to notice that a grid independent result is obtained on the refined triangular grid of 7834 nodes, but not on the unrefined rectangular grid of 12836 nodes. The rectangular grid of 4196 nodes refined on pressure gradient to 10038 nodes however is sufficiently refined. This leads to the conclusion that the difference between triangular and rectangular grid is not important, but the refinement on pressure gradient is.

On closer inspection of the grids, it becomes clear that on the refined grids the gaps between rotors and between rotors and casing are fully resolved, while this is not the case on the unrefined grids. The neighbouring grid cells in which different velocity constraints are imposed in the unrefined grids are causing problems.

Consider two neighbouring cells as depicted generically in figure 3.6. Consider the top cell to have its center within the boundary of the top rotor and the bottom cell analogously the bottom rotor. Consider that the velocity constraints are enforced perfectly. In that case the velocity in the top cell center

C_t conforms a rigid-body motion around the top rotor center and the velocity in the bottom cell center C_b conforms a rigid-body motion around the bottom rotor center, as illustrated in figure 3.6.

Even though a rigid-body motion is essentially divergence-free, the flow field considered over the two cells in figure 3.6 is in general not divergence-free. In such it is unphysical and cannot be obtained. This is generally true for two neighbouring cells that have to fulfil velocity constraints from different origins.

Now consider the case depicted in figure 3.7. Here the gap between the rotors is resolved. There is a cell that has no velocity constraint situated between the cells considered above. It is now possible to have a velocity in the three cells that allow the top and bottom cell to fulfil their constraints and still obtain a divergence-free flow field.

Returning to the test case of the lobe pump, this general conclusion can be observed astutely. In figure 3.8 the cells with center within the rotors are depicted on the unrefined structured grid of 4196 cells. It is clearly observed that the gaps are not sufficiently resolved. The cells depicted are coloured with contours of rotational velocity (around the rotor centers). The rotational velocity imposed is 460 rpm. If the velocity constraint is enforced correctly, at least all cells on the rotor surfaces should have a rotational velocity of 460 rpm. However, the rotational velocity ranges from 410 to 490 rpm on the rotor surface. This means that the immersed boundaries no longer follow a rigid-body motion. This means that $\oint_{\partial\omega} \vec{v} \cdot d\vec{S} \neq 0$ and therefore $\oint_{\partial\omega} \rho\vec{v} \cdot d\vec{S} \neq 0$. The immersed boundaries are not impermeable. This results in a calculated mass flow rate that is too low.

With the penalty force defined as in (3.1), the failure to enforce the velocity constraint leads to huge pressure peaks in the flow domain (figure 3.9) located in the problem areas. This means that refining on pressure gradient refines the grid exactly there where it should be refined, namely in the under-resolved gaps (figure 3.10).

Figure 3.11 shows the analogue of figure 3.8 after refinement to 24750 cells. One immediately notices that the gaps are fully resolved. The rotational velocity ranges from 458 to 461 rpm on the rotor surfaces. This is an indication that the velocity constraint is sufficiently enforced. The mass flow rate calculated on this grid is the grid independent value.

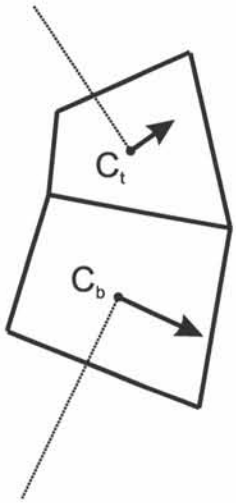

Figure 3.6: Neighbouring cells with different kinematic constraints

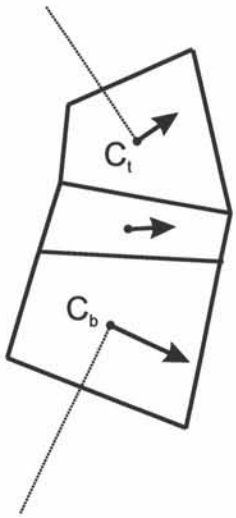

Figure 3.7: Neighbouring cells with different kinematic constraints with an intermediate cell

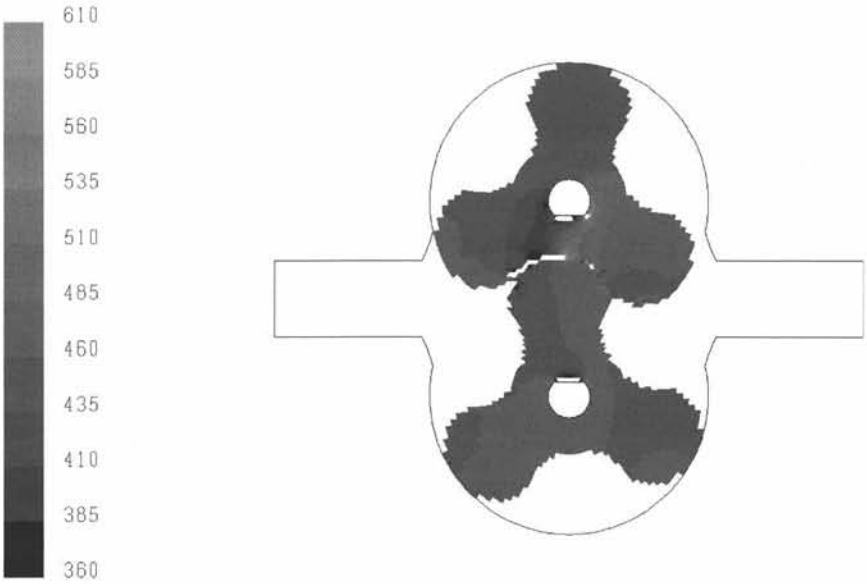

Figure 3.8: Rotational velocity as imposed on the unrefined grid of 4196 cells

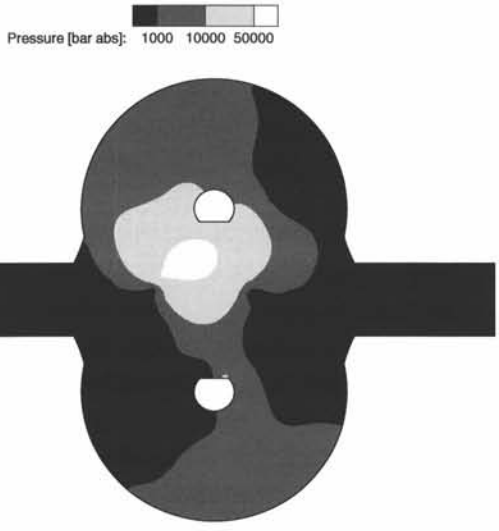

Figure 3.9: Pressure distribution on the unrefined grid of 4196 cells

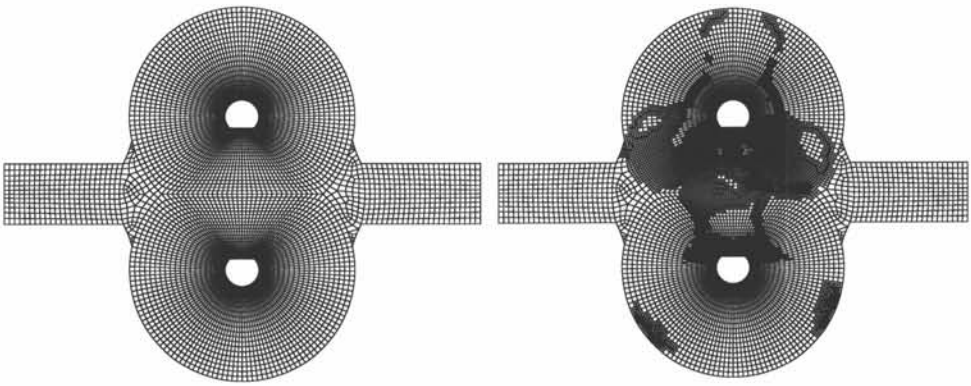

Figure 3.10: Refinement on pressure gradient of the grid of 4196 cells to 24750 cells

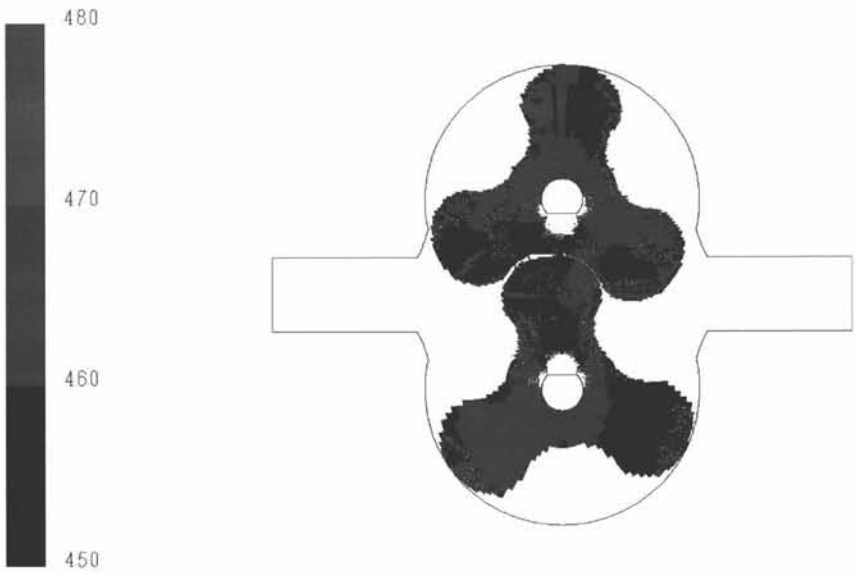

Figure 3.11: Rotational velocity as imposed on the refined grid of 24750 cells

3.1.2 Time dependent flow calculation

To assess the quality of the results, a time-dependent calculation is performed.

The same lobe pump geometry was used as in the previous sections. The diameter of the rotors is 122.5 mm. The rotational speed of the rotors is 460 rpm. The size of the gap between rotors and casing is 0.3 mm. The pumped fluid is silicon oil with a density of 880 kg/m^3. The pressure ratio between outlet and inlet is 2/1 bar abs.

The grid used consists of 22191 cells. This grid was not refined on pressure gradients. The rotor contact zone was determined a priori and the size of the gap between the rotors was estimated to be of the same order as the gap between rotors and casing. Based on these considerations a grid was constructed that is sufficiently fine near the rotor contact zone. The penalty factor C_0 was chosen to be 10^{12}. The resulting mass flow rate is shown in figure 3.12.

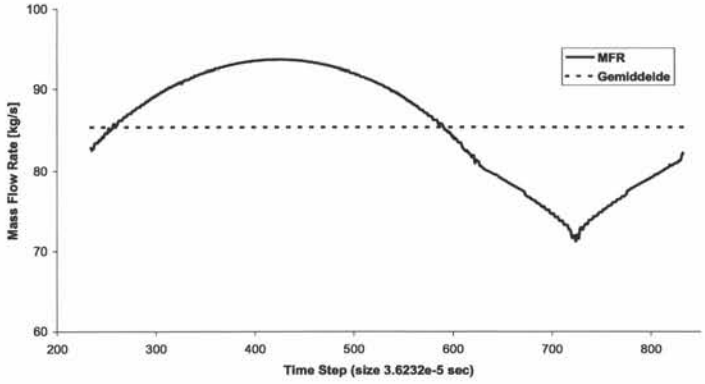

Figure 3.12: Mass flow rate as function of the time

The mean mass flow rate is 85.42 kg/s. The theoretical mass flow rate (without leakages) is 87.61 kg/s. This leads to a volumetric efficiency of 97.5 %, which is a realistic value. However, as there are no experimental data to compare with, only qualitative conclusions can be drawn. To allow some assessment, a moving grid calculation was performed on the same geometry. The result is shown in figure 3.13. This calculation was published in the Journal of Thermal Science [48]. The paper is attached as an appendix to this book. The mean mass flow rate calculated with the moving grid simulation is slightly lower, namely 84.10 kg/s.

This means that the mass flow rate as calculated with the fictitious domain calculation is realistic. The amount of fluid pumped through the inlet and the outlet port is probably nearly correct, and the method could be used to study phenomena occurring in these ports.

However, there is still a significant difference in the prediction of the leakage flows. The fictitious domain calculation predicts a leakage flow of 2.2 kg/s, while the ALE calculation predicts 3.5 kg/s. This is 60% more!

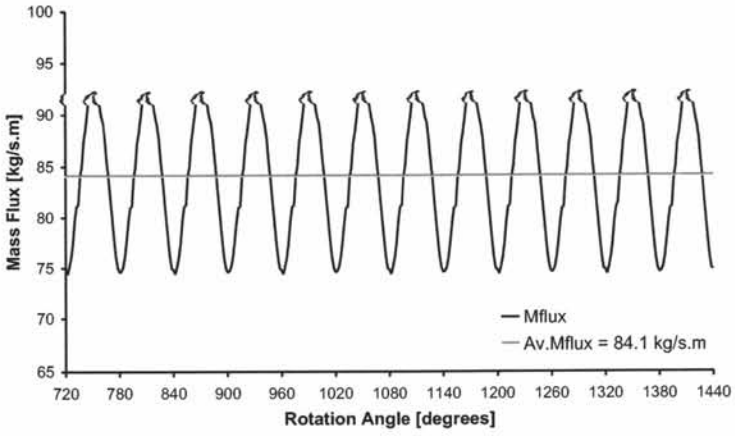

Figure 3.13: Mass flow rate as function of the rotation angle, obtained through ALE calculation

In figure 3.14 contours of pressure are depicted in the flow domain for the fictitious domain calculation. One immediately notices the large pressure peaks in the rotor contact zone. These peaks are the result of the large penalty forces that are necessary to enforce the velocity constraint in this zone. The velocity on the rotor surface conforms a rigid-body rotation around two fixed points. In the rotor contact zone this results in large gradients of velocity, which in turn result in large pressure gradients. On the other hand, the leakage flows are mainly dependent on the pressure gradients in the gaps. It is only natural that the leakage flows are wrongly estimated in the presence of large unphysical pressure peaks such as seen here. Therefore, the moving grid calculation is better suited for flow calculations meant to assess the leakages.

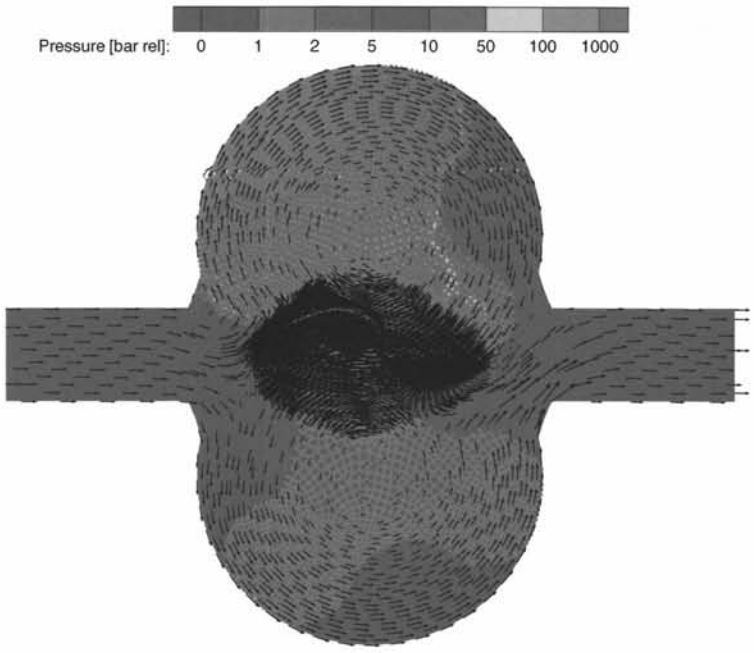

Figure 3.14: Pressure distribution and velocity vectors in the lobe pump (time dependent simulation)

3.1.3 Conclusion

The penalty force fictitious domain method implemented in a rough form as described above, can be used to simulate flow with impermeable immersed rotors in rotary positive displacement pumps. However, there are two major remarks.

The grid used must be sufficiently fine near the immersed boundary. Each cell cut by the immersed boundary, must be neighboured by a free cell (not cut by another immersed boundary). This is a necessary condition so that a divergence-free flow field can exist while conforming the velocity constraints on the immersed boundaries. If this condition is not fulfilled, the velocity constraint on the immersed boundary cannot be enforced. Constructing such a grid was not too difficult for the case of the lobe pump presented. However, it can be a complex task to determine the zones that need a fine grid, especially in three-dimensional geometries. On top, the grids rapidly become very large.

The second remark is that the introduction of the penalty forces leads to an unphysical pressure distribution in the flow field. From the case study presented, it is concluded that the influence of the penalty forces is large where two or more immersed boundaries come close together. The unphysical pressure distribution makes the method unusable for the study of leakage flows.

In general for all fictitious domain methods, the exact implementation of the velocity constraint on the immersed boundary is not possible. Mathematically, the exact implementation of the velocity constraint on the immersed boundary would locally decouple the velocity field from the pressure field. This means that locally at the immersed boundary, the pressure field no longer follows from the velocity field. This is very clear for the penalty force method, where an exact enforcement of the velocity constraint would put the penalty force to zero, immediately cancelling the exact enforcement of the constraint. In general, when linearizing the flow equations, this leads to degeneration of the flow matrix, making an exact solution impossible [26]. This means that the velocity constraint can only be enforced approximated. For most cases of open flow, impermeability of the immersed boundary can be obtained without introducing much unphysical behaviour and the consequences of the previously stated are small. However, when studying leakage flows between two moving immersed boundaries in the presence of relatively large pressure gradients, it can result in a notable error.

3.2 Compressible flow

The implementation of a Penalty-Force Fictitious Domain Method discussed above was also tested for compressible flow. In a first step the technique was tried unaltered on a tooth compressor geometry.

3.2.1 Tooth compressor geometry

A tooth compressor is a positive-displacement compressor. Figure 3.15 shows a typical geometry. A more in-depth description of tooth compressors is given in the next chapter. For the moment it suffices to emphasize that the pressure rise in the compressor is the result of the reduction of volume of the working chamber. This working chamber is formed by the compressor casing and the rotor surfaces. As these rotor surfaces are fictitious in this calculation, a good implementation of the boundary conditions, especially the impermeability, is of utmost importance.

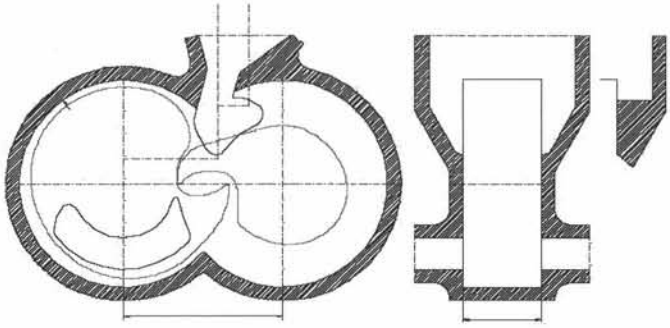

Figure 3.15: Tooth compressor geometry

Figure 3.16 shows the grid and the fictitious rotors in the simulations. The grid is three-dimensional unstructured. As can be noticed, for this first simulation, the grid used is relatively coarse to limit computing time.

Figure 3.17 shows contours of pressure in the flow domain at the moment just before the working chamber makes contact with the outlet port. This is the moment when the pressure rise is the highest (the volume reduction is maximal). Nevertheless, almost no pressure rise results from the volume reduction in this fictitious domain simulation. Obviously, something is wrong with the implementation of the boundary conditions on the rotor surfaces.

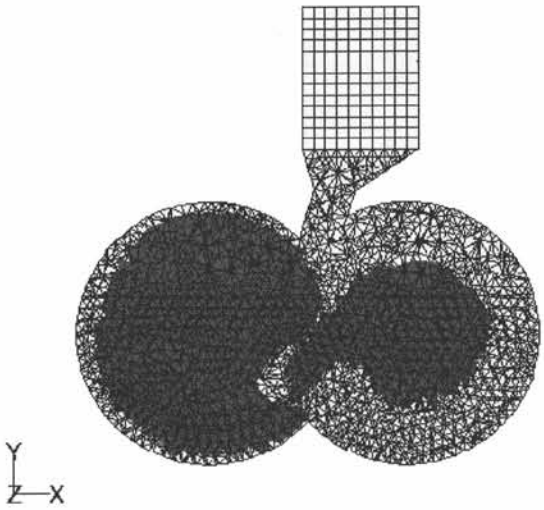

Figure 3.16: Unstructured grid in the tooth compressor geometry

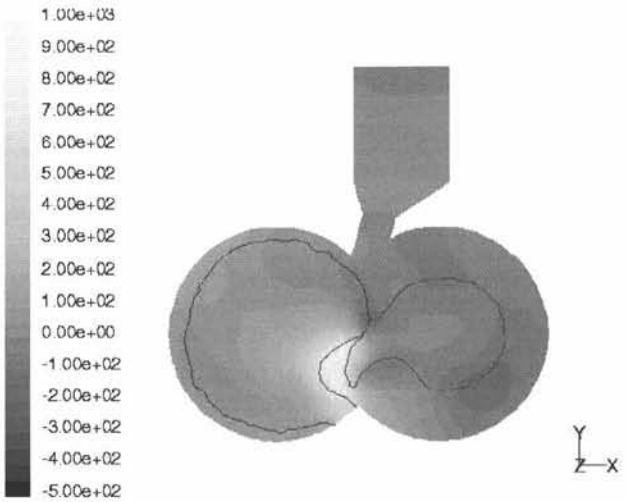

Figure 3.17: Contours of pressure in the tooth compressor geometry

3.2.2 Background to the extension to compressible flow

The boundary condition that has to be enforced on the immersed boundary is a moving wall. This means that the fluid velocity at the immersed boundary has to be the velocity of the boundary, and that the immersed boundary has to be impermeable.

$$\vec{v} = \vec{v}_{wall} \quad \text{at} \quad \partial\omega_I \tag{3.3}$$

$$\rho\,(\vec{v} - \vec{v}_{wall}) = 0 \quad \text{at} \quad \partial\omega_I \tag{3.4}$$

When correctly enforced, the kinematical restraint (3.3) also guarantees impermeability.

In compressible flow, the ideal-gas law couples density, pressure and temperature

$$p = \rho RT \tag{3.5}$$

Thus, the three equations expressing conservation of mass, momentum and energy form a coupled system of equations.

At the immersed boundary, another boundary condition has to be fulfilled expressing the influence of the wall on the energy equation. For instance an adiabatic wall :

$$\nabla T \cdot d\vec{S} = 0 \tag{3.6}$$

This boundary condition could be enforced by introducing a 'penalty energy source' in the energy equation analogous to the penalty force in the momentum equation.

In any way, the enforcement or neglection of the energy boundary condition has no direct impact on the impermeability boundary condition.

In theory, it should be possible to enforce impermeability by simply enforcing the kinematic restraint, similarly to the incompressible flow fictitious domain method.

3.2.3 Piston compressor geometry

To study the problems involved in the extension of the fictitious domain method described above to compressible flow, an easier geometry is chosen. The compression of air in a piston compressor is simulated.

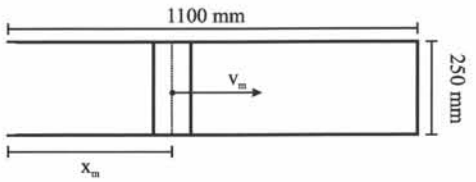

Figure 3.18: Piston compressor geometry

A two-dimensional calculation of an adiabatic piston compressor was performed (cf. figure 3.18). The calculation domain is a rectangle of 1100 mm by 250 mm. A grid of 550x25 cells was applied. The domain is closed at the righthand side and is open at the lefthand side. A piston of 100 mm width is emulated through the PFFD method described in section 3.1, which means that at each time step the piston extends over about 50 cells.

The position x_m of the piston centre is given by polynomial (3.7). The velocity of the piston (e.g. v_{rigid} in (3.1)) is defined by expression (3.8). Physically, (3.7) and (3.8) express a piston displacement of 1/3 m in one second, with a maximum piston velocity of 0.5 m/s at the half-way point. The enclosed volume is halved during the compression.

$$x_m = \frac{1}{3} + 0.05 + t^2 - \frac{2}{3}t^3 \tag{3.7}$$

$$v_m = \frac{dx_m}{dt} = 2t - 2t^2 \tag{3.8}$$

The working fluid is air, initialised throughout the domain at 1 bar abs. The ideal-gas law is used to relate density, pressure and temperature. The atmospheric pressure is considered to be 1 bar. To simplify the calculations, the left edge is given a pressure-inlet boundary condition with pressure equal to 1 bar abs.

Figure 3.19 shows pressure contours in the fluid domain for several flow times. Figure 3.20 shows the evolution of the pressure during the compression. At the end of the compression, the volume of the chamber is halved and the temperature has risen from 300 K to 319 K. The pressure corresponding with this temperature rise should be 2.13 bar abs. For an adiabatic compression, the pressure should be 2.64 bar abs. In figures 3.19 and 3.20 one can see that the pressure is much lower than both these values. As pressure, volume and temperature are known at each flow time, one can calculate the mass that resides in the compression chamber. This mass is plotted vs. flow time in figure 3.20. Obviously the piston is not impermeable.

3.2.4 Conclusion

A definite mass loss is observed in the simulation of a piston compressor.

This error can have two origins.

Firstly, the FLUENT code is a co-located code. The calculation of numerical mass fluxes on co-located grids always introduces a small error. Although the mass flux is physically of the form $\dot{\vec{m}} = \vec{u} \cdot \rho \cdot A$, in co-located codes an extra term is added:

$$\dot{\vec{m}} = \vec{u} \cdot \rho \cdot A + \frac{1}{u_{ref}} \cdot \frac{\partial p}{\partial x} \cdot \Delta x \cdot A \tag{3.9}$$

This extra term is added to suppress pressure wiggles in the flow field.

If the pressure rates in the fluid are dynamic, thus caused by differences in kinetic energy, the factor $\frac{1}{u_{ref}}$ guarantees that this extra term is small. Furthermore the grid size Δx in the extra term ensures consistency.

However, if the pressure rates are not dynamic, as is the case for volumetric compression, the extra term can become large and introduce a serious error in the calculation of the mass fluxes.

A second error is made when spatially discretizing the impermeability boundary condition (3.4). This error will be large if the gradient in ρ is large, or when the gradient ∇p is large.

Both errors scale with the grid size Δx. But for the presented calculation

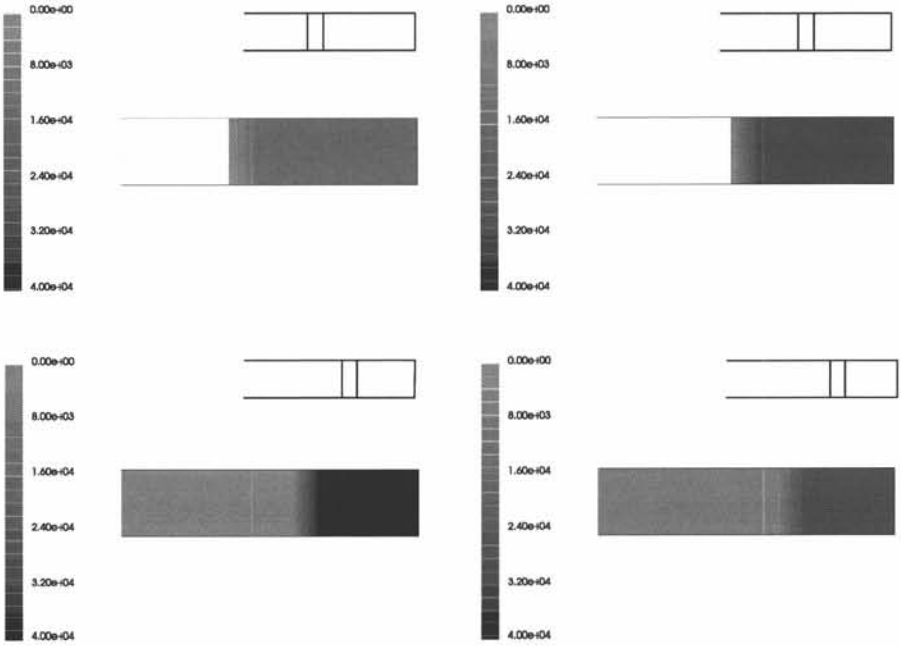

Figure 3.19: Contours of pressure in the piston compressor

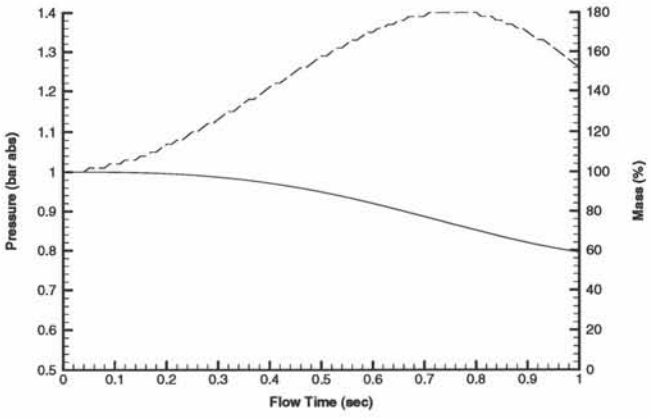

Figure 3.20: Evolution of pressure (dashed line) and mass (full line) in the compressing cylinder

of flow in a piston compressor, the used grid already was relatively small. Yet the mass loss in one compression stroke was around 40 %!.

It is to be expected that to reduce the error to an acceptable value, an unfeasibly fine grid would be needed.

3.3 Conclusion

A simple form of the Penalty Force Fictitious Domain Method has been tested.

The test case for incompressible flow yields good general results. The mass flow rate calculated through a lobe pump is close to reality. Nevertheless, to obtain this result, a very fine mesh is necessary. This fine mesh and the introduction of a large body force result in large calculation times. Furthermore, in the vicinity of the immersed boundary, the flow field is disturbed by the penalty force. As it is generally impossible to obtain a sharp interface at the immersed boundary, this method is not suited for the investigation of leakage flows in rotary positive-displacement pumps. It could however be used to study the performance of the inlet and outlet ports.

Fictitious domain methods in theory can be easily extended to compressible fluid flows. However, in practice, it proves to be very cumbersome to enforce the impermeability constraint correctly. An extremely fine grid is needed. Preliminary results obtained in this study show such important deviations from reality that further research in this method for rotary positive-displacement compressors is deemed inopportune.

Chapter 4

ALE Calculations : Generation of the Basic Grid

In chapter 2, two methods were presented that could be used to perform computational fluid dynamics calculations of flow through rotary positive-displacement machines.

In the previous chapter, the fictitious domain methods were handled. It was shown that these methods are not suited for the simulations this research is aimed at. In the remainder of this book, the possibilities and the implementation of the Arbitrary Lagrangian-Eulerian (ALE) method is documented.

4.1 Introduction

The Arbitrary Lagrangian-Eulerian or ALE method in se consists of performing a numerical flow calculation using the ALE formulation of the flow equations (4.1)-(4.3). This formulation expresses conservation of mass, momentum and energy, just like the standard (Eulerian) formulation. The difference is that in the ALE formulation the boundary velocity of the control volumes (the grid cells) is explicitly incorporated.

conservation of mass

$$\frac{\partial}{\partial t}\int \rho dV - \int \rho\left(\vec{u}-\vec{u}_b\right)\cdot d\vec{S} = 0 \tag{4.1}$$

conservation of momentum

$$\frac{\partial}{\partial t}\int \rho\vec{u}dV + \int \rho\vec{u}\left(\vec{u}-\vec{u}_b\right)\cdot d\vec{S} = \int -p\cdot d\vec{S} + \int \vec{\vec{\tau}}\cdot d\vec{S} \tag{4.2}$$

conservation of energy

$$\frac{\partial}{\partial t}\int \rho E dV + \int \rho E\left(\vec{u}-\vec{u}_b\right)\cdot d\vec{S} = \int -p\vec{u}\cdot d\vec{S} + \int \left(\vec{u}\cdot\vec{\vec{\tau}}\right)\cdot d\vec{S} \tag{4.3}$$

This adaptation allows the grid to move freely, with a velocity independent from the flow field. As this velocity $\vec{u}_b$ appears as an extra unknown in the flow equations, an extra equation is added to the set.

$$\frac{\partial}{\partial t}\int dV + \int \vec{u_b}\cdot d\vec{S} = 0 \tag{4.4}$$

This is the space conservation law. It is in fact also a conservation law, expressing conservation of volume.

It must be stressed that this formulation is physically and mathematically correct. The same arsenal of numerical techniques available to classical flow calculations can be used on the equations (4.1)-(4.3). The same numerical accuracy can be reached. The space conservation law (4.4) is decoupled from the other equations. It is usually solved separately. From research reported in literature [20, 9], it is shown that the accuracy of the solution is not critically dependent on the numerical solution of this extra equation. Several discretization techniques, with or without truncation term, are available and give good results.

Therefore, from a numerical solver point of view, there are no great complications in implementing the ALE formulation of the flow equations instead of the classical Eulerian formulation. There is no notable difference in numerical accuracy. At present and at the start of this research, several commercial CFD codes offer the ALE formulation of the flow equations as an option. For

the research reported in this book, it is opted to make use of a commercial CFD code capable of ALE calculations. Further intricacies concerning the implementation of the ALE equations in a numerical solver will in this book only be touched on as need be for the understanding of this research. For a deeper insight reference is made to general literature.

Using the ALE formulation of the flow equations it is possible to perform flow calculations in domains with moving boundaries by manipulating the grid in the flow domain. This moving grid must conform to two limitations.

Firstly, it must be possible to uniquely discretize the flow equations in time. Any discretization in time can be rewritten to the form

$$\begin{bmatrix} p \\ \vec{u} \\ T \\ \vec{u}_b \end{bmatrix}^{n+1} \cdot A = \begin{bmatrix} p \\ \vec{u} \\ T \\ \vec{u}_b \end{bmatrix}^{n} \cdot B + \begin{bmatrix} p \\ \vec{u} \\ T \\ \vec{u}_b \end{bmatrix}^{n-1} \cdot C + \ldots \tag{4.5}$$

In (4.5) the superscript n+1, n, n-1, ... denotes the value of the flow parameters plus the grid cell boundary velocity $\vec{u}_b$ at time step n+1, n, n-1, ... respectively.

Obviously, for this discretization to make sense, it is necessary that the flow parameters be taken from the same grid cells. This means that the definition of the grid cells may not be changed. The grid topology must be maintained. Such actions that change the grid topology are the generation of new cells, the deletion of cells and flipping cell faces (figure 4.1). These are forbidden. In practice, the only action allowed on the grid is moving the grid nodes. The movement of the nodes is however completely free.

The second limitation on the grid manipulation stems from the spatial discretization. At each time step, the grid must be of good quality for the spatial discretization to be sufficiently numerically accurate.

A grid of good quality is fine (high grid resolution) where the flow parameters have high gradients. The faces of the cells are as much as possible orthogonal to each other (orthogonality of the grid). The change of volume between neighbouring grid cells should be small. A cell should have roughly the same size along all three dimensions; its aspect ratio should be close to one. What is acceptable depends on the flow solver, but an aspect ratio of 20 is generally considered to be too large. Ideally, the grid should be aligned with the flow field.

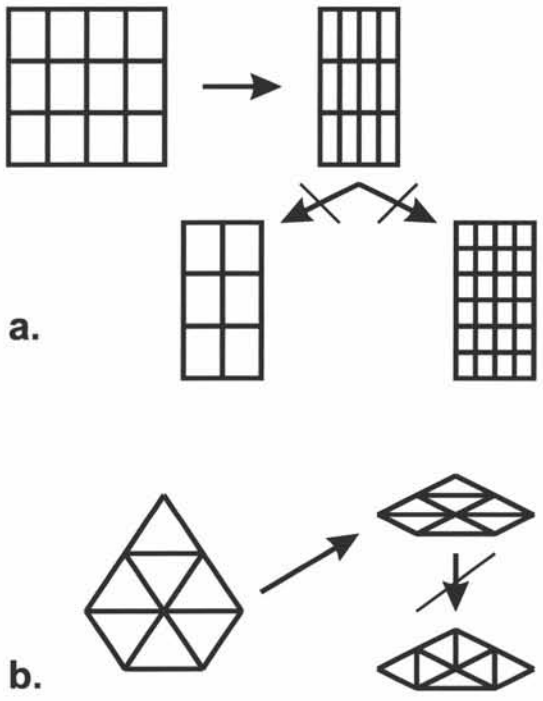

Figure 4.1: Grid movement with and without maintaining grid topology; a. generation and deletion of cells; b. flipping cell faces

In practice, an ideal grid does not exist. A trade-off has to be made between the considerations above. The quality of the grid is a general term used to express the suitability of this trade-off for the calculation at hand.

If one performs an ALE calculation in a domain with moving boundaries, the difficulty of the calculation is shifted to the manipulation of the grid during the simulation. In the remainder of this book an algorithm will be presented to allow ALE calculations in rotary positive-displacement machines. The goal is a robust algorithm that can be used on all rotary positive-displacement geometries. The algorithm will be validated by performing flow calculations in a tooth compressor and a screw compressor and by subsequently comparing results with experiments.

4.2 Requirements for the grid generation

Figure 4.2 is an exploded view illustration of a tooth compressor geometry. The inlet and outlet ports can be recognized, as well as the casing with the two rotors. All rotary positive-displacement machines have this basic layout. The flow domains range from mainly two-dimensional for a lobe pump to complex three-dimensional for a screw compressor.

The flow domain naturally splits into four blocks, namely the inlet and outlet ports and a block associated with each rotor. It is opted to let the calculation grid reflect this. A block-structured grid will be used with four blocks joined together using grid interfaces. The use of such interfaces is standard in most commercial CFD codes and will not be elaborated on.

As the boundaries of the inlet and the outlet ports do not move, they can be furnished with a grid using any of the available commercial grid generators. Due to the normally complex nature of their geometry, the possible use of a powerful unstructured grid generator is very welcome.

The only portion of the grid with moving boundaries, are the two blocks associated with the rotors. These blocks constitute the casing of the machine. Figure 4.3 shows the casing without inlet and outlet. This is the portion of the grid that is handled by the grid manipulation algorithm.

It is opted to mesh the casing with a grid that is structured and hexagonal. In the direction of the rotation axis it is build up by stacking slices of

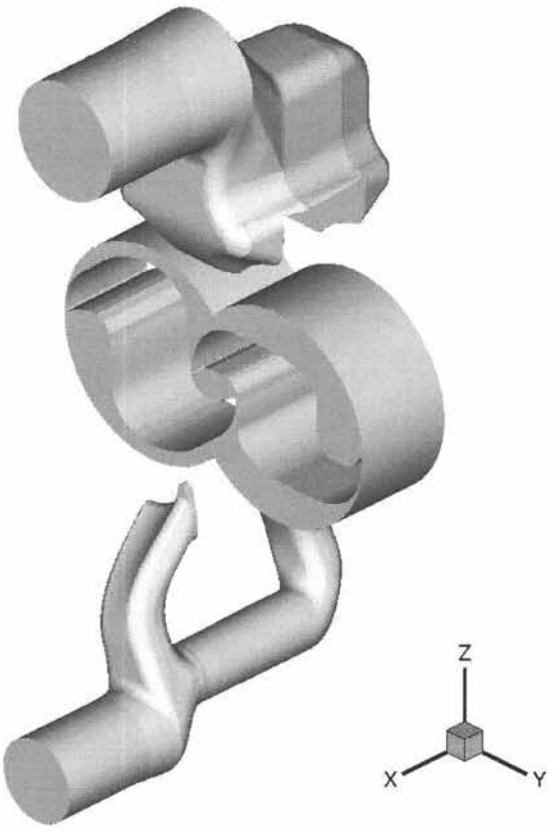

Figure 4.2: Exploded view of a tooth compressor geometry

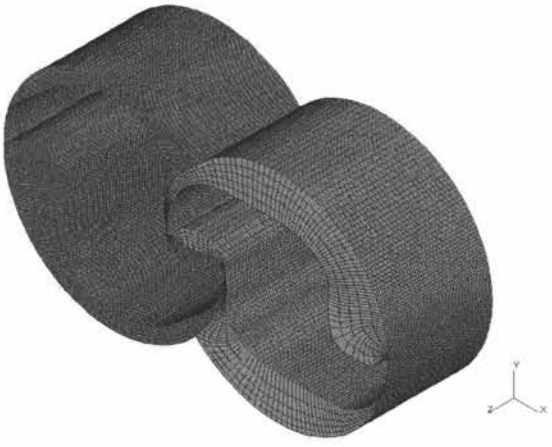

Figure 4.3: Casing of a tooth compressor

two-dimensional rectangular grids. The two-dimensional grids are structured and rectangular. The use of a rectangular structured grid has two distinct advantages. Firstly, the data structure needed to store the grid is much less complicated for a structured grid than for an unstructured grid. In a structured grid, each node can be defined by two sets of coordinates (i,j) and (x,y) (cf. figure 4.4). The coordinates x and y are dimensional coordinates along the X-axis and Y-axis. The coordinates i and j determine the position of the node in a grid cell matrix. Every grid cell is defined by the four nodes (i-1,j), (i,j),(i,j-1),(i-1,j-1). This makes it possible to store the entire grid in a matrix for which the element on row i and column j is the set of coordinates (x,y) of node (i,j).

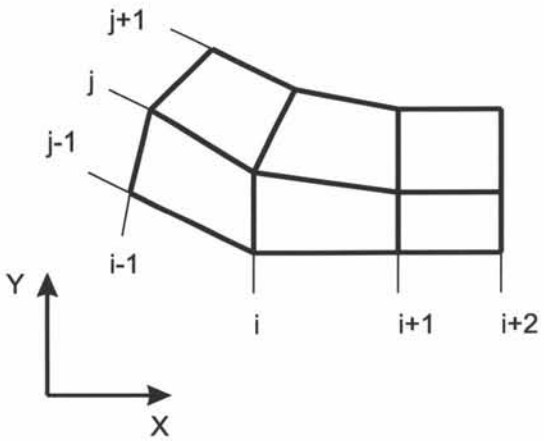

Figure 4.4: Definition of a grid cell in a structured grid

The data structure of an unstructured grid is very different. In a 2D unstructured grid, each grid cell only knows which faces define it. Each face knows which two cells it defines and which two nodes it is defined by. Each node knows its own position (x,y). Obviously, this data structure is much more complex. The advantage of such a data structure is that a grid can be generated in a domain by an algorithm that need not oversee the entire domain. It is possible to device algorithms that start meshing at one boundary and move forward until the entire domain is meshed. In general, unstructured grid generators are more powerful in meshing complex geometries.

A second (and more important) advantage of using a structured rectangular grid is the possibility to align the grid with the local flow field. In rotary positive-displacement machines it is very important to simulate the leakage flows accurately. By aligning the grid with the flow field in the gaps between rotors and between rotors and casing, the numerical accuracy of the flow cal-

culations is improved in these areas.

The stacking of the two-dimensional grids in slices perpendicular with the rotor axis maintains the structured character of the two-dimensional grid in the third dimension. More importantly, the effect of a rotation of the rotors is a rotation of the rotor profile in the two-dimensional slices. Thus the grid problem is reduced to manipulating the two-dimensional grid in the slices as the rotor profile rotates.

A final advantage of structured rectangular grids concerns the grid topology. Two structured grids with the same number of nodes in the directions I, J and K (for instance tangential, radial and axial) have the same grid topology. After all, every grid cell in a structured rectangular grid is defined by the nodes (i-1,j,k), (i,j,k),(i,j-1,k),(i-1,j-1,k),(i-1,j,k+1), (i,j,k+1),(i,j-1,k+1),(i-1,j-1,k+1). This means that the numerical solver does not know the difference between moving the nodes of a structured rectangular grid, and replacing this grid alltogether with a new grid with the same number of nodes in direction I, J and K.

Thus the grid problem at hand is further reduced to generating a good structured rectangular 2D grid for every rotation of the rotor profile in the slices. By a good grid is meant a grid that is orthogonal, aligned with the flow field in the gaps, has no great changes in cell volume between neighbouring cells and has no cells with excessive aspect ratios.

In the remainder of this chapter the generation of a basic grid is discussed. This basic grid has most of the qualities mentioned above. It is the basis for the grids that are used for the calculation of flow through a tooth compressor and a screw compressor.

4.3 Basic grid generation

The generation of the basic grid and its application to a preliminary calculation of flow a in tooth compressor was published in the Journal of Computational Methods in Applied Mechanical Engineering [49].

4.3.1 Background

To illustrate the generation of the basic grid the geometry of a double-tooth compressor will be used. More details on these compressors will be given in the chapter 6. Figure 4.2 shows the three-dimensional geometry of the tooth compressor. Figure 4.5 shows the two-dimensional calculation domain that has to be furnished with a structured rectangular grid.

The generated grid should be orthogonal and aligned with the gaps between rotors and between rotors and casing.

With this in mind, a potential solution has some very favourable characteristics. The solution of the Laplace equation $\nabla^2\Phi = 0$ with as boundary condition a constant potential Φ on the boundaries of the domain, is shown in figure 4.6.

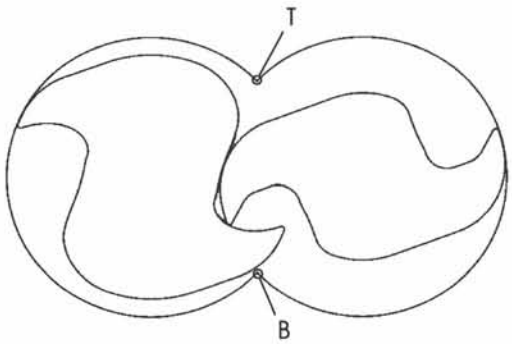

Figure 4.5: The 2D domain to be meshed

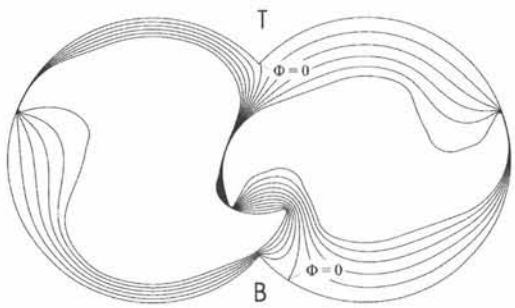

Figure 4.6: Potential solution in the domain of figure 4.5; $\Phi = 0$ on the casing, $\Phi = 1$ on the left rotor, $\Phi = -1$ on the right rotor

The iso-potential lines in the solution of the Laplace problem never cross. Because of the constant boundary conditions, they are naturally aligned with the walls of the flow domain in the gaps. In every point of the domain, the iso-potential lines are also perpendicular with the gradient lines (lines tangent to the gradient $\nabla\Phi$). Last, but not least, the Laplace solution also displays a natural smoothness.

These characteristics of a Laplace potential solution were first exploited in grid generation by Winslow in 1967 [52]. Winslow used a Laplace formulation to generate a smooth and aligned triangular grid for the calculation of quasi-linear Poisson equations in non-rectangular domains. Winslow desired a mesh in an arbitrarily shaped polygonal domain. The mesh had to be composed of regions with zones of different average mesh spacings, with the mesh spacings varying smoothly. He derived a method by "formulating the zoning problem as a potential problem, with the mesh lines playing the role of equipotentials" [52].

The triangle mesh is mapped onto a regular equilateral triangle array composed of three sets of straight lines intersecting at 60 degrees (cf. figure 4.7). Any two sets of these straight lines are sufficient to completely define the mesh. Let the mapping of the two sets chosen be associated with the functions $\chi(x, y)$ and $\psi(x, y)$. Winslow demands that these two functions satisfy the Laplace equations

$$\begin{aligned} \nabla^2\chi &= 0 \\ \nabla^2\psi &= 0 \end{aligned} \tag{4.6}$$

The boundary conditions to these equations are determined by imposing a node distribution on the physical boundaries. After solving (4.6) the intersecting iso-potential lines $\chi = constant$ and $\psi = constant$ form the triangle mesh, together with the third set drawn through the intersection points. Winslow found the resulting triangular mesh to be smooth and of good overall quality.

Winslow solved equations (4.6) by inverting them and writing them in terms of $x(\chi, \psi)$ and $y(\chi, \psi)$, using the relations

$$\begin{aligned} \chi_x &= -\tfrac{1}{J} \cdot y_\psi \quad & \psi_x &= \tfrac{1}{J} \cdot y_\chi \\ \chi_y &= -\tfrac{1}{J} \cdot x_\psi \quad & \psi_y &= \tfrac{1}{J} \cdot x_\chi \end{aligned} \tag{4.7}$$

The Jacobian $J = x_\psi y_\chi - x_\chi y_\psi$.

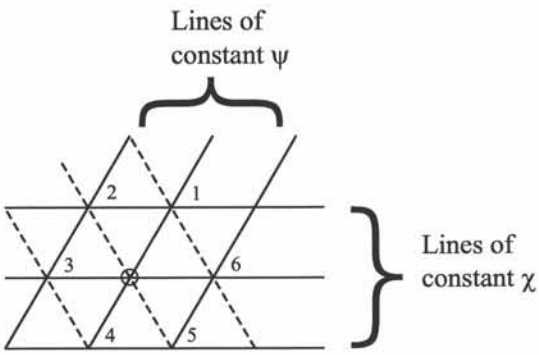

Figure 4.7: A vertex and its six neighbours in triangular $\chi - \psi$ space

(4.6) is transformed into the inverse Laplace equations

$$\begin{aligned} \alpha x_{\chi\chi} - 2\beta x_{\chi\psi} + \gamma x_{\psi\psi} &= 0 \\ \alpha y_{\chi\chi} - 2\beta y_{\chi\psi} + \gamma y_{\psi\psi} &= 0 \end{aligned} \tag{4.8}$$

with α, β and γ

$$\alpha = x_\psi^2 + y_\psi^2 \tag{4.9}$$

$$\beta = x_\chi x_\psi + y_\chi y_\psi \tag{4.10}$$

$$\gamma = x_\chi^2 + y_\chi^2 \tag{4.11}$$

In (4.7) to (4.11) a_b is a notation for $\frac{\partial a}{\partial b}$. The solution of the transformed equations (4.8) gives the coordinates of the nodes of the triangular grid directly, without actually solving the original Laplace potential equation.

The method is readily extendable to rectangular grids. The rectangular mesh is mapped on a regular equilateral rectangular array composed of two sets of straight lines intersecting at 90 degrees (cf. figure 4.8). The mapping of these two sets is associated with the functions $\chi(x, y)$ and $\psi(x, y)$, which satisfy the Laplace functions (4.6). After inverting, the same set of equations (4.8) is obtained. The solution of (4.8) again directly gives the coordinates of the grid nodes. Each cell of the rectangular grid is defined by the nodes (χ,ψ), $(\chi+1,\psi)$, $(\chi+1,\psi+1)$ and $(\chi,\psi+1)$.

To solve equation (4.8) numerically, finite-difference expressions have to be generated for the derivatives occurring in (4.8) to (4.11). As these expressions refer to the parameter domain, they are of course different for rectangular and

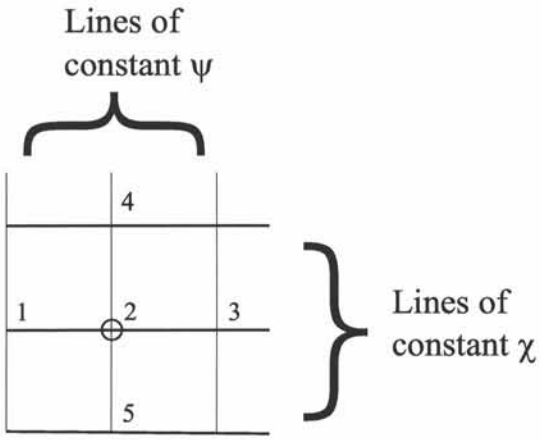

Figure 4.8: A vertex and its four neighbours in rectangular $\chi - \psi$ space

triangular grids. Winslow uses finite-difference expressions obtained by the line integral method using Gauss' theorem. For instance for x_χ he obtained :

$$x_\chi = \frac{1}{6}\left[(x_2 + 2x_1 + x_6) - (x_3 + 2x_4 + x_5)\right] \tag{4.12}$$

with $x_1 ... x_6$ as in figure 4.7.

For the rectangular grid one could for instance use central differencing :

$$x_\chi = \frac{1}{2\Delta x}\left(x_5 - x_4\right) \tag{4.13}$$

Winslow's method is widely used, especially for exterior flow problems. It has been elaborated on by Brackbill and Saltzman [15] and Thompson et al [44] to allow more control over the mesh spacing. Thompson developed a method for generating body-fitted coordinates in multiply connected domains. Brackbill made the method adaptive to singular problems.

These methods all enjoyed a large popularity. They are very useful in "giving an accurate numerical representation of the boundary geometry" [15]. Because of the use of the Laplace potential solution a grid is obtained that is smooth and aligned with the physical boundaries.

In none of these methods the potential solution is explicitly calculated. The positioning of the nodes just directly reflects this solution. This is of course more efficient from a computing standpoint. But it makes it difficult to control how the potential solution is used for the grid generation.

For the grid generation in geometries of a complexity as considered in this research, more control over the use of the potential solution in the grid generation process is needed than can be offered by any of the methods based on Winslow's technique. Therefore it is opted to calculate the solution of the Laplace potential solution explicitly in the grid domain. Based on this solution, the domain is fitted with a rectangular structured grid.

4.3.2 The Laplace potential solution

To obtain the Laplace potential solution the domain is fitted with a triangular grid. It cannot be stressed enough that this grid has this sole purpose. It has absolutely no relation to the grid used for the flow calculation.

The domain considered is shown in figure 4.5. It is a two-dimensional slice of the casing of the tooth compressor shown in figure 4.3. The points indicated with T and B in figure 4.5 are the top and the bottom cusp of the casing. The inlet and outlet ports are neglected, as they will be meshed separately with a stationary grid.

The specifications the triangular grid has to fulfill are the following. It is a stationary grid. It is not used for flow calculations, but just to solve the Laplace problem. Therefore there is no reason for it to be aligned to anything, but as the potential problem is an elliptic problem, the grid should fulfill the Delaunay condition. The grid spacing should be sufficiently fine to get a good resolution of the potential solution everywhere in the domain. The final rectangular grid used in the flow simulation will be based on this solution. Irregularities resulting from a lack of resolution in the potential problem will be reflected in the rectangular grid as less smooth zones. In specific, this means the grid should be very fine in the gaps between the rotors and between the rotors and the casing.

For this purpose an unstructured triangular grid generator is chosen. Unstructured triangular grid generators are in general more powerful at gridding complex domains. It is inherent to unstructured grids that they have no preferred direction. This is not a problem, as the grid shouldn't be aligned along

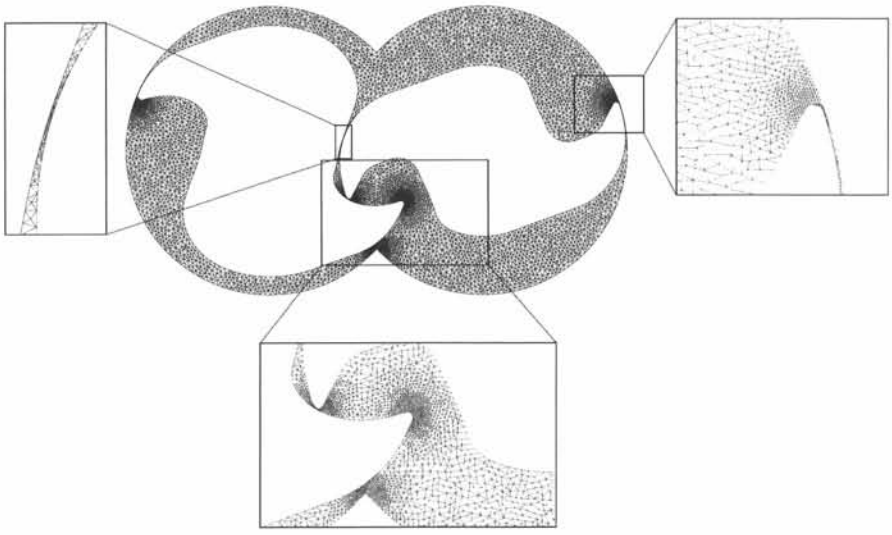

Figure 4.9: Unstructured triangular grid in the domain of figure 4.5

a certain direction. A very important advantage of triangular grids is that they can be smoothly locally refined with relative ease. This is necessary to keep the grid size from becoming huge, while still having sufficient fine grid spacing in the gaps.

The grid generator used is an in-house algorithm developed by Riemslagh and Vierendeels [34]. It generates a triangular grid that fulfills the Delaunay condition. The grid is refined around the tips of the rotors and in the gap between the rotors. By refining the grid around the rotor tips, one is ensured that the grid is fine in the gaps between rotor and casing. The grid generator uses a smoothing algorithm to improve the quality of the grid. Figure 4.9 shows the unstructured triangular grid.

On this triangular grid, the Laplace potential equation

$$\nabla^2 \Phi = 0 \tag{4.14}$$

is solved.

To define the potential problem uniquely, boundary conditions have to be determined on the boundaries of the domain.

As a first step, assume constant boundary conditions. A constant potential $\Phi = 0$ is imposed on the casing, and $\Phi = 1$ and $\Phi = -1$ on the left,

respectively right rotor surface. The solution of this problem is depicted on figure 4.10. On this plot, the nice characteristics of the potential solution from a grid generation point of view are clear. The iso-potential lines never cross. The direction of the gradient is perpendicular with the iso-potential lines in every point. The lines tangential to the gradient $\nabla\Phi$ are called gradient lines. Because of the constant boundary condition on the casing and the rotors, the gradient lines are also orthogonal with the boundaries.

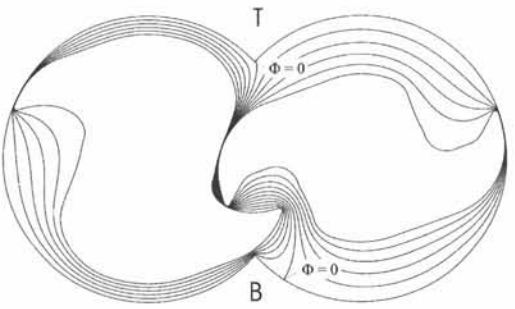

Figure 4.10: Potential solution with constant boundary conditions in the domain of figure 4.5

In a straightforward manner, a grid might be constructed using potential lines and gradient lines of the solution shown in figure 4.10 as grid lines.

The iso-potential line $\Phi = 0$ (indicated on figure 4.10) is used as a division line to split the domain in two blocks associated with each rotor. The nodes on the casing and the division line are distributed equidistantly. The nodes with constant tangential index i are placed on the gradient lines drawn from the nodes on the casing and the division line. The node distribution on the gradient lines is equidistant. Because of the constant boundary conditions, this means that nodes with equal radial index j are located on the same iso-potential line. This completely defines a structured rectangular grid.

This grid is of good quality in most of the domain. It is orthogonal and well aligned in the gaps. It has an overall smooth character. There however is a problem zone where the grid is absolutely terrible. Near the cusps, the grid quality is very bad. The reason for this is the constant boundary condition on the casing. Because the entire casing is in effect an iso-potential line of potential line 0, there is no guarantee that the iso-potential line $\Phi = 0$, which is used as a division line will start and end in the cusps. If this is not the case, the grid quality near the cusp is poor. Figure 4.11 shows what happens to the grid if the division line is not drawn from cusp to cusp. In that case the grid is

'pulled over the cusp'. In the best case, the grid looses its smoothness. But it is likely for cells with negative volume to arise, which makes the grid invalid.

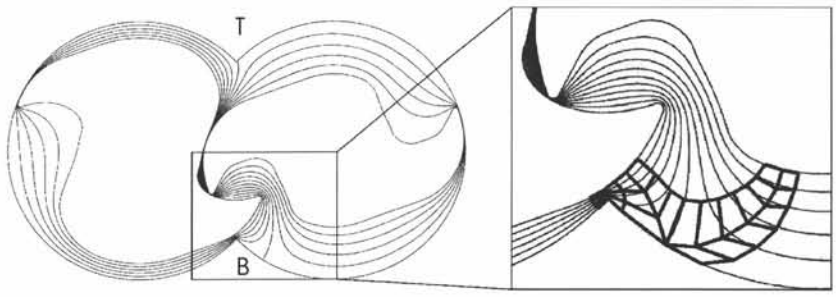

Figure 4.11: When the division line is not drawn from cusp to cusp, the grid is pulled over the cusp

To remedy this, the constant boundary condition on the casing is abandoned. On the left, respectively right rotor surface a constant potential $\Phi = 1$ and $\Phi = -1$ is still imposed. On the casing a potential Φ is imposed that changes linearly from Φ_T to Φ_B. Φ_T is the potential in the top cusp and Φ_B is the potential in the bottom cusp. The values Φ_T and Φ_B are a parameter to the problem. The condition that has to be fulfilled for the chosen Φ_B and Φ_T is that the tangent to the iso-potential line emerging from the cusp has to be comprised within the tangents to the casing (cf. figure 4.12). After all, whatever the definition of the division line, at its start and end it will be tangent to the iso-potential line emerging from the cusp. By ensuring that this tangent is comprised within the tangents to the casing, it is prevented that the grid would be pulled over the cusp. The value of Φ_B and Φ_T is determined iteratively. The potential problem is solved for different values of Φ_B and Φ_T. The rate of change of the angle between the iso-potential line and the tangent of the casing in the cusp is evaluated versus the rate of change of the value Φ_B and Φ_T. Based on this rate of change a new estimate is made for Φ_B and Φ_T. Thus is iterated until the condition mentioned above is met.

In figure 4.13, the solution of the Laplace equation with the new boundary conditions is shown. The most important difference is that as the casing is no longer an iso-potential, the gradient lines are no longer orthogonal with the casing. However, the iso-potential lines are still pretty much aligned with the boundaries of the domain. The deviation from orthogonality in the rectangular grid will be small and the grid will still be very well aligned with the flow field in the gaps.

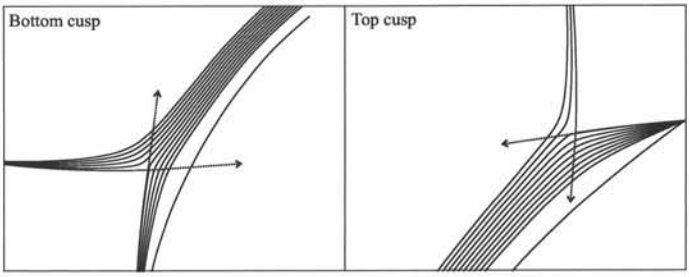

Figure 4.12: The tangent to the iso-potential line emerging from the cusp has to be comprised within the tangents to the casing

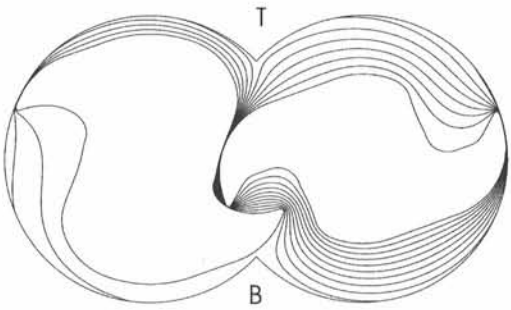

Figure 4.13: Potential solution with varying boundary conditions in the domain of figure 4.5

4.3.3 The basic grid

The domain in figure 4.5 has to be split in two blocks, each associated with a rotor. If the division line is not drawn from cusp to cusp, the grid quality will be poor near the cusps. As the potential in the top and the bottom cusp is Φ_T and Φ_B respectively, it is not possible to use an iso-potential line to divide the domain. However, an iso-potential line has the distinct advantage of rougly following the rotor contours in the gap between both rotors.

It is opted to use an iso-potential for the middle section of the division line. Near the top and bottom cusp, the division line follows a transitional path along which the potential changes smoothly to the values Φ_T and Φ_B (cf figure 4.14).

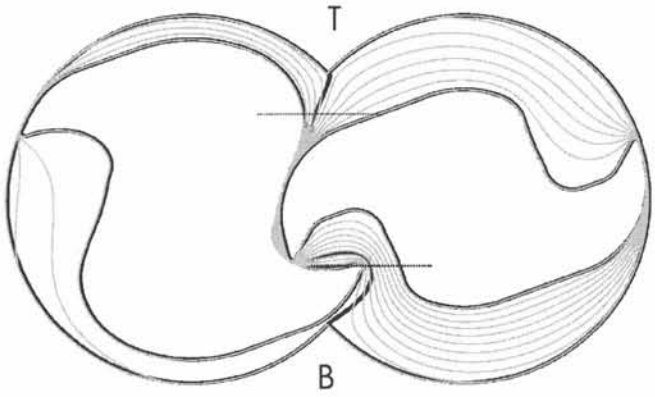

Figure 4.14: Division line and potential solution in the domain of figure 4.5

The iso-potential of the middle section of the division line can in essence be chosen freely.
A potential Φ_D is chosen that will avoid jumps in grid cell volume across the division line in the rectangular grid. The potential on the rotor surfaces is constant. Therefore it can be proven that along a gradient line, the distances between equipotentials relate as the values of these equipotentials :

$$\text{along } \nabla\Phi : \qquad \frac{\int_{\Phi_1}^{\Phi_2} d\vec{r}}{\int_{\Phi_1}^{\Phi_3} d\vec{r}} = \frac{\Phi_2 - \Phi_1}{\Phi_3 - \Phi_1} \tag{4.15}$$

With (4.15) in mind, the potential Φ_D is determined to be :

$$\Phi_D = -1 + 2\frac{nrl}{nrl + nrr} \tag{4.16}$$

with nrl and nrr the number of radial nodes in the left, respectively right grid block. This value of Φ_D guarantees that wherever assumption (4.15) holds, the distance along the gradient line between radially equidistantly spaced nodes is the same from the left rotor to the right, without a jump across the division line.

Near the cusps, the division line follows a transitional path along which the potential changes from Φ_D to Φ_T or Φ_B.

Consider a reference system defined as follows. The Y-axis is drawn from the bottom cusp to the top cusp. The X-axis completes a right-handed orthogonal coordinate system. For generality, the Y-axis is made dimensionless with the distance between both cusps. y-values range from 0 (bottom cusp) to 1 (top cusp).

Near the bottom cusp B, the transitional part of the division line is defined for y-values from 0 to Y_B. Near the top cusp, it is defined for y-values from Y_T to 1. Assume that for the transitional parts the relation $\Phi(x)$ between Φ and x is unique and can be uniquely inversed for constant y. Then for these parts the division line can be defined by a function $\Phi(y)$.

The transition to the middle (iso-potential) section of the division line has to be mathematically smooth to the first order. After all, the tangential direction in every point of the division line is :

$$\frac{\left(\frac{dx}{dy}, 1\right)}{\left\|\left(\frac{dx}{dy}, 1\right)\right\|} = \frac{\left(\frac{dx}{d\Phi}\frac{d\Phi(y)}{dy}, 1\right)}{\left\|\left(\frac{dx}{d\Phi}\frac{d\Phi(y)}{dy}, 1\right)\right\|} \tag{4.17}$$

If $\Phi(y)$ is not smooth to the first order, $\frac{dx}{dy}$ in (4.17) is not continuous and there is a nudge in the division line. This nudge in the division line can create a zone in the rectangular grid that is less smooth.

Therefore, the transitional part is modeled after a cosine, as this guarantees a function $\Phi(y)$ that is smooth to the first order.

The definition of the division line is :

$$\begin{array}{ll} y \leq 0, & \Phi = \Phi_B \\ 0 < y \leq Y_B, & \Phi(y) = a_B \cdot \Phi_B + (1 - a_B) \cdot \Phi_D \\ Y_B < y < Y_T, & \Phi = \Phi_D \\ Y_T \leq y < 1, & \Phi(y) = a_T \cdot \Phi_T + (1 - a_T) \cdot \Phi_D \\ y \geq 1, & \Phi = \Phi_T \end{array} \tag{4.18}$$

$$\text{with } a_B = 0.5 \cdot (1 + \cos(\tfrac{y}{Y_B} \cdot \pi))$$
$$\text{and } a_T = 0.5 \cdot (1 + \cos(\tfrac{(1-y)}{(1-Y_T)} \cdot \pi))$$

The values of the parameters Y_T and Y_B still have to be defined. They determine how far the transitional part extends in the division line definition. An important thing to keep in mind here is that for as long as the division line follows the transitional path, there is a jump in cell volume across the division line in the rectangular grid. From this viewpoint, the transitional part should be as limited as possible. On the other hand, if the transitional part is small, the derivative $\frac{\partial \Phi}{\partial y}$ is large in the transitional part. This derivative in essence expresses the rate of change of the potential on the division line to the change in y-coordinate. If it is high, the curvature of the division line can become large, and the rectangular grid may loose some of its smoothness. From this point of view the transitional part of the division line shouldn't be too small.

In the situations depicted in figure 4.15 the two main influences on a well-chosen length of the transitional part can be recognized.
If the gradient Φ is large, the transitional part of the division line can be small.
If the difference between the cusp potential Φ_B and the potential Φ_D is large, the transitional part should grow.

It is opted to make length Δy (which is $(1 - Y_t)$ or Y_B) scale with the horizontal distance Δx from the cusp to the iso-potential line $\Phi = \Phi_D$:

$$Y_B = C_1 \, \Delta x \qquad \text{and} \qquad Y_T = 1 - C_1 \, \Delta x \tag{4.19}$$

In practice it is shown that a value of 1 for C_1 is a good choice. This completely defines the values of Y_T and Y_B. The definition of the division line is now final. In figure 4.14 the division line in the domain of figure 4.5 is depicted.

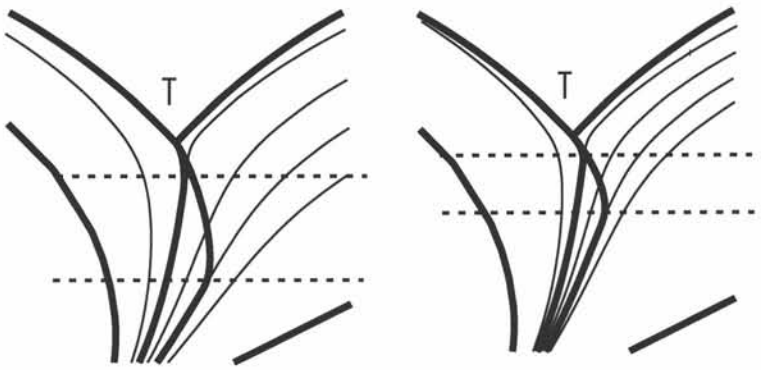

Figure 4.15: Possible transitional parts of the division line for a large and small value of $(\Phi_D - \Phi_T)$ near the top cusp; the extent of the transitional parts is indicated with a dashed line; left: low $\nabla\Phi$; right: high $\nabla\Phi$

The domain is thus split into two blocks. The left block is to be meshed with a grid of *ntl* nodes tangentially and *nrl* nodes radially and the right block with a grid of *ntr* x *nrr* nodes. *Ndiv* nodes are placed on the division line. Any node in one of these blocks is defined by its tangential coordinate i ($0 < i < ntl$ or $0 < i < ntr$) and its radial coordinate j ($0 < j < nrl$ or $0 < j < nrr$).

First $ntl - ndiv$ nodes are placed on the left casing and $ntr - ndiv$ nodes on the right casing and *ndiv* nodes on the division line. The spacing of the nodes is equidistant. These nodes all have radial coordinate $j = 0$. The remaining nodes are placed on gradient lines drawn from these nodes. Their spacing on the gradient lines is equidistant. All nodes placed on the same gradient line have the same tangential coordinate i.

In this manner, all nodes have been placed in the domain. The grid cells are defined by the tangential and radial coordinates (i,j) of the nodes. A grid cell is defined by the nodes (i,j), (i+1,j), (i+1,j+1) and (i,j+1).

This concludes the basic grid generation. Figure 4.16 shows the grid in the domain.

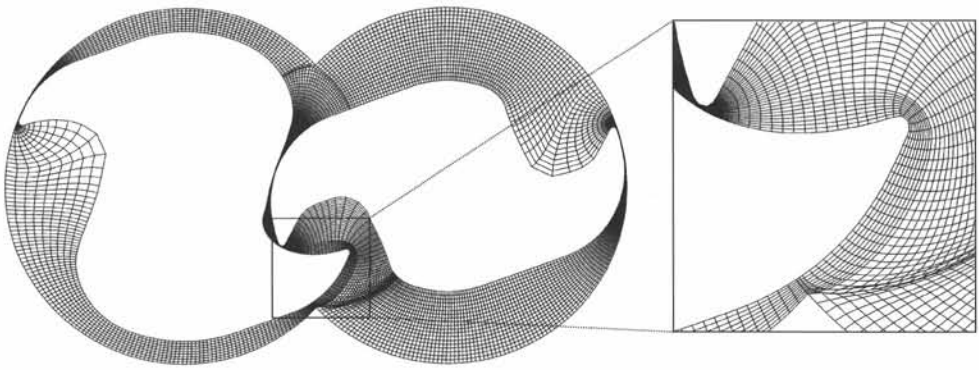

Figure 4.16: Basic grid generated in the domain of figure 4.5

4.4 Final remarks

A few remarks have to be made to conclude this chapter. Although the nodes on the casing and the division line are equidistant, the spacing is not the same for the left casing, the right casing and the division line, except for a specific choice of the values *ntl*, *ntr* and *ndiv*. This is a desired feature as it allows to obtain a higher grid resolution on the division line to better resolve the gap between the rotors.

Because of the definition of the middle part of the division line, there is no jump in cell volume across the division line. Across the transitional parts of the division line there however is a jump in cell volume (cf. blow-up in figure 4.16). This jump can be large. It may interfere with the quality of the grid.

As the boundary condition on the casing to the potential problem is not a constant, the casing is not an iso-potential line. For the same reason, placing the nodes equidistantly on the gradient lines does not put nodes with the same radial index j on iso-potential lines. However, as can be noticed on figure 4.16, the grid is still very much orthogonal and it is strongly aligned in the gaps.

Overall, the quality of the grid is quite good because of the favourable properties of the potential solution. There are some zones where the quality of the grid is beneath standard. In the next chapter, adaptations to the grid generation algorithm are discussed that will ensure a high-quality grid throughout the domain.

Chapter 5

ALE Calculations : Ameliorations to the Basic Grid

In chapter 4, the generation of a basic grid was discussed. This basic grid was generated based on the solution of the Laplace potential equation $\nabla^2\Phi = 0$, explicitly obtained in the domain. As a potential solution has some very favourable characteristics for grid generation, the overall quality of this basic grid was good. Nevertheless, there are zones in the basic grid where the grid quality deteriorates. In this chapter, improvements to the basic grid are suggested and implemented.

The grid generator and its application to a flow calculation in a screw compressor was presented at the 17th AIAA Computational Fluid Dynamics Conference in Toronto [47].

5.1 Grid spacing

Grid spacing is an important issue in meshes. There are three things to consider.

Firstly, the grid spacing should be fine enough to accurately resolve the flow field. It is obvious that flow phenomena of a scale that is the same or

smaller than the grid spacing cannot be resolved. In the calculated flow field these phenomena will not occur. If these phenomena are interesting to the researcher or, even worse, if they have a notable effect on the overall flow field, it is paramount that the grid resolution is high enough to capture them. A special place in this problem takes turbulence as a phenomenon. Turbulence definitely has an influence on the flow field if it occurs, as it seemingly alters the fluid viscosity. Yet turbulence ranges in scale from microscopic to macroscopic. Apart from very specific cases, its influence on the flow is modeled through the use of a turbulence model and the grid spacing does not have to resolve the smallest scales.

The grid spacing should also be fine enough to accurately resolve the geometry of the boundaries of the flow domain. After all, the boundaries of the flow domain are discretized in space. What in reality is a continuous boundary is in the calculation domain made up of a succession of line segments. If the curvature of the boundary is high, the grid spacing has to be fine for the approximation by line segments to be accurate.

When calculating flow through rotary positive-displacement machines, the most interesting and influential flow characteristic is the leakage flows. Therefore the grid spacing has to be fine in the gaps between rotors and between rotors and the casing. In the working chamber, the actual flow field is of little interest. Bear in mind that the work is transferred to the fluid by shrinking and expanding the working chamber. Mixing losses occurring in the working chamber are calculated correctly for any grid spacing. Even if the working chamber is considered to be just one control volume (one grid cell) the mixing losses can be calculated. There is no need for a fine grid in the working chamber. The tips of the rotors of the machine have to be geometrically accurately resolved. They determine the shape of the gap between rotors and casing and have a notable effect on the leakage flow through the gap between both rotors. This is especially true for screw compressors, as the rotor tips in screw compressors have features to minimize the gaps (cf figure 5.1). Therefore it is important that the grid spacing is fine around the rotor tips.

Another thing to consider in grid spacing is the numerical accuracy of the flow calculation. The best numerical accuracy is obtained on a lattice that is orthogonal with equal spacing in all dimensions and throughout the domain, and that is aligned with the flow field. Of course, these restrictions would make it impossible to mesh any realistic flow domain. Numerical schemes have evolved a lot and the restrictions for these four issues are a lot less stringent. Nevertheless, numerical schemes still have difficulties with them if they are

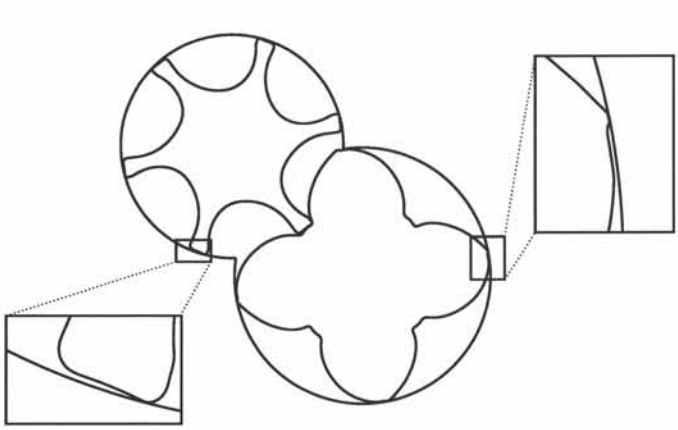

Figure 5.1: Small-scale features on screw rotor tips

too exuberant.

Because of the use of the potential solution, the basic grid is nearly orthogonal. It is also very well aligned with the flow field in the gaps. There is, however, a jump in grid cell volume across the division line near the cusps. And there are zones in the grid with elongated cells. The aspect ratio of these cells (the ratio of the longest edge to the shortest edge) is in some instances too large. This has to be improved on.

5.1.1 Jump in cell volume across the division line

Figure 5.2 shows the basic grid as generated according to the algorithm presented in the previous chapter. It consists of two blocks, each associated with a rotor. In each block, the volume of the grid cells changes gradually. However, near the cusps, there is a jump in cell volume across the division line (figure 5.3). This has a negative impact on the numerical accuracy of the calculations and therefore must be remedied.

The radial spacing of all nodes (the spacing between nodes with the same tangential index i) is equidistant. The middle section of the division line follows an iso-potential line with potential chosen specifically to avoid a jump in cell volume across it in case of equidistant spacing. Here there is no problem. Near

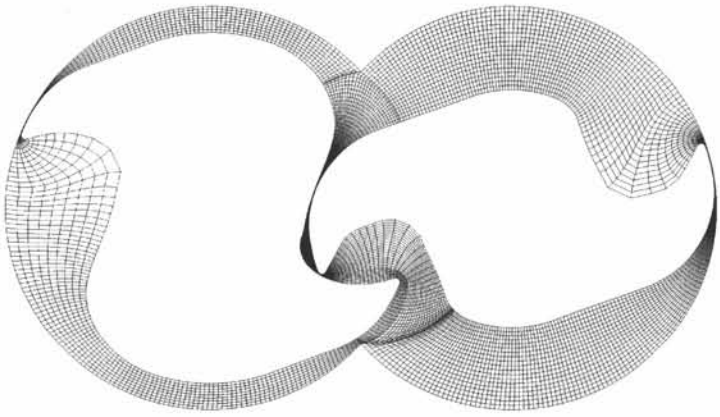

Figure 5.2: Basic grid as generated at the end of chapter 4

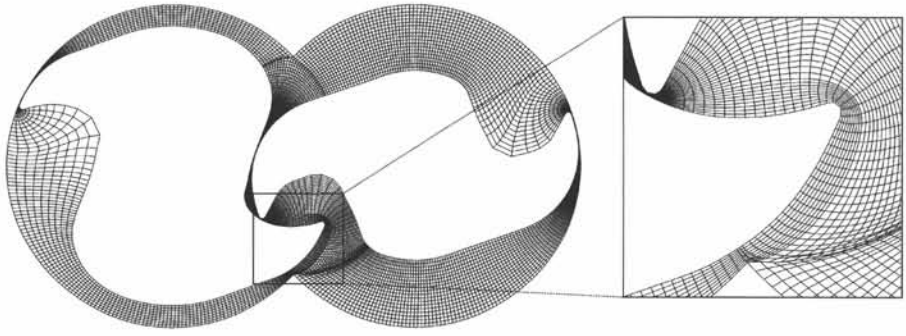

Figure 5.3: Jump in cell volume across the division line

the cusps, the division line follows a path along which the potential changes to the value in the cusp. It is across this part of the division line that a jump in cell volume is experienced (figure 5.4).

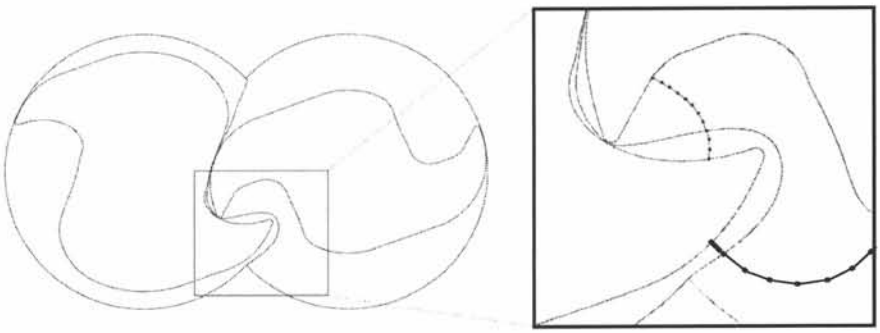

Figure 5.4: Equidistant radial spacing on gradient lines

To remedy the problem, the equidistant radial spacing is abandoned in favour of geometric spacing. Consider a node that is positioned on the transitional part of the division line. The other nodes with the same tangential index will be placed on a gradient line drawn from this node.

The geometrical distance along the gradient line to the left rotor L_L and the right rotor L_R is calculated. This distance is divided by the number of cells radially in each block. The result is the radial spacing in case of equidistant spacing. For the side of the division line for which this value is the smallest, the nodes are spaced equidistant on the gradient line. Call this spacing ΔL_{equi}. On the other side of the division line, the nodes are spaced on the gradient line according to a geometric series with factor q. This factor q is determined so that the distance along the gradient line from the node on the division line to the first node on the gradient line is $q.\Delta L_{equi}$.

$$\sum_{i=1}^{nrl} q^i \Delta L_{equi} = L_L \qquad \text{or} \qquad \sum_{i=1}^{nrr} q^i \Delta L_{equi} = L_R \tag{5.1}$$

This procedure is repeated for each node on the division line. The result is shown on figure 5.8. The spacing can be indicated by a set of factors $q_{i,L}$ and $q_{i,R}$. In this i is the tangential index of the nodes and L and R indicates whether the factor defines the spacing in the left block or the right block. An equidistant spacing is defined by a factor $q = 1$.

If equidistant radial spacing is maintained for nodes on gradient lines emerging from the casing, the grid is not very smooth. The spacing according to a geometric series should be eased out away from the cusps. On the other hand, the radial spacing in the gaps between rotor and casing should be equidistant. Therefore, the nodes on gradient lines drawn from nodes on the casing are also spaced according to a geometric series. The factor q_i changes linearly from the value it has in the cusp to 1 in the point on the casing closest to the rotor tip.

5.1.2 Grid resolution in the zone where the rotors mesh

In the zone where the rotors mesh the grid spacing should be finer around the interlocking teeth. It is important to accurately represent the rotor tips and the flow phenomena they induce. This means that the grid spacing must be fine around the tips of the interlocking teeth.

As explained in chapter 4, the rectangular grid is generated by distributing nodes equidistantly on the casing and the division line and then placing the remaining nodes on gradient lines drawn from these initial nodes. If the initial nodes were distributed in a different manner, this would have an effect on all nodes with the same tangential index i. In concrete, if the nodes on the division line were to be drawn closer together on the division line in the area of the rotor tips, the grid spacing would be finer around the tips. This means that to adapt the grid resolution in the zone where the rotors mesh, the nodes on the division line should not be distributed equidistantly. They should be spaced closer together near the rotor tips.

When searching for a quantitive criterion by which to redistribute the nodes on the division line, it is important to bear in mind that the division line is an iso-potential line, except for a small transitional part near each cusp. As the boundary condition for the potential problem on the rotor surfaces is a constant potential Φ, the iso-potential lines between both rotors roughly follow the contours of the rotor surfaces. Combining these two notions leads to suggest the division line curvature to be a good quantitive criterion by which to redistribute the division line nodes. Indeed, on figure 5.5 one can clearly see that the curvature is higher near the rotor tips.

Instead of using the curvature, the radius of curvature of the division line is used as a redistribution criterion. The radius of curvature is the inverse of the curvature. This means that the nodes on the division line have to be

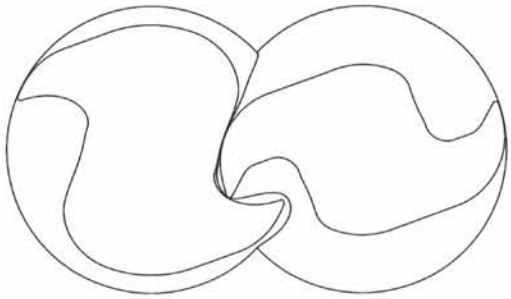

Figure 5.5: The division line between the two blocks

drawn towards where the radius of curvature is small.

Consider $R(s)$ to be the radius of curvature of the division line as a function of the arc length s along the division line. High radii indicate an almost straight division line. For all parts of the division line where the radius of curvature is higher than a certain treshold value, the node spacing should be the same. To achieve this, the function $R(s)$ is fed through a low-pass filter. All values of $R(s)$ higher than a certain treshold are limited to that treshold. The result is the function $r(s)$.

To actual redistribute the nodes, a function $F(s)$ is used. This function is applied to an equidistant node distribution

$$[s_0 ... s_{n-1}] \qquad \text{with} \qquad (s_{i+1} - s_i) = \Delta s = \frac{|division\ line|}{n} \tag{5.2}$$

The resulting values are the arc lengths to which the nodes are moved.

$F(s)$ has to comply with the following :

$$F(s) : s \in [s_0 ... s_{n-1}] \tag{5.3}$$

$$F(0) = 0$$

$$F(|division\ line|) = |division\ line|$$

A trivial example of a function $F(s)$ is $F(s) = s$. The result is again an equidistant node distribution.

The function $F(s)$ that will be used is determined by the radius of curvature $r(s)$. Its definition is :

$$\frac{dF(s)}{ds} = C_0 \cdot \rho(F(s)) \tag{5.4}$$

$$C_0 = \frac{\int_0^{|division\ line|} \rho(F(s)) \cdot ds}{|division\ line|}$$

The first line assures that the distance between the new position of the nodes $(dF(s))$ is directly related to the curvature of the division line. The second line defines the constant C_0 to scale $F(S)$ in order for $F(|division\ line|) = |division\ line|$.

Figure 5.5 shows the calculation domain and the division line. Figure 5.6 shows the radius of curvature $R(s)$ as a function of the arclength s and the radius of curvature $r(s)$ after low-pass filtering. Figure 5.7 illustrates the redistribution of the nodes. The top section shows the function $F(s)$ as defined by (5.4). The bottom section illustrates the equidistant node distribution used as starting point and the new distribution defined by $F(s)$. Figure 5.8 shows the result of this redistribution on the grid.

This method is very effective in augmenting the grid resolution near the tips of the meshing rotors. However, for grid generation in screw compressor geometries, the method turns out to be too violent. This problem will be handled more in depth in chapter 7 discussing flow calculation in a screw compressor geometry. Suffice to mention that the effect of the method just described needs to be damped.

To dampen the effect of the redistribution, underrelaxation is built in. Be $\left[s_0^{equi} ... s_{n-1}^{equi}\right]$ the equidistant node distribution and be $\left[s_0^{curv} ... s_{n-1}^{curv}\right]$ the distribution as defined by the function $F(s)$ above. The final distribution of the nodes is

$$\left[m \cdot s_0^{curv} + (1-m) \cdot s_0^{equi} ... m \cdot s_{n-1}^{curv} + (1-m) \cdot s_{n-1}^{equi}\right] \tag{5.5}$$

In (5.5) m acts as relaxation constant. For $m = 0$, the distribution is equidistant. For $m = 1$, the nodes are distributed as defined by $F(s)$.

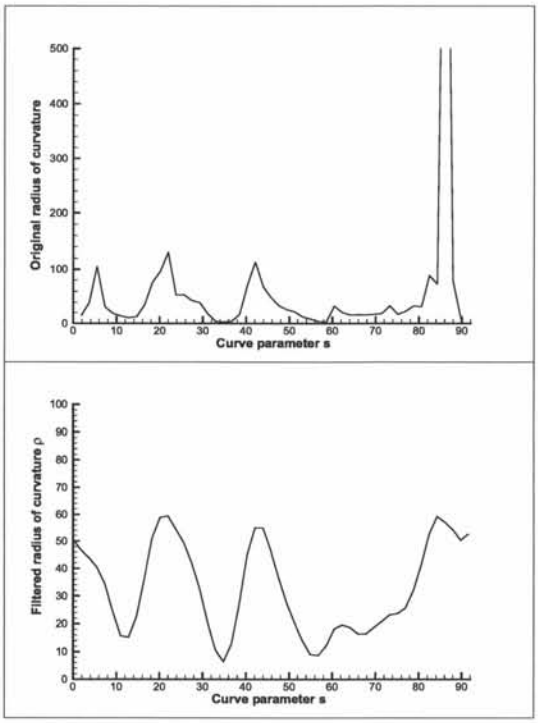

Figure 5.6: Radius of curvature of the division line before and after low-pass filtering

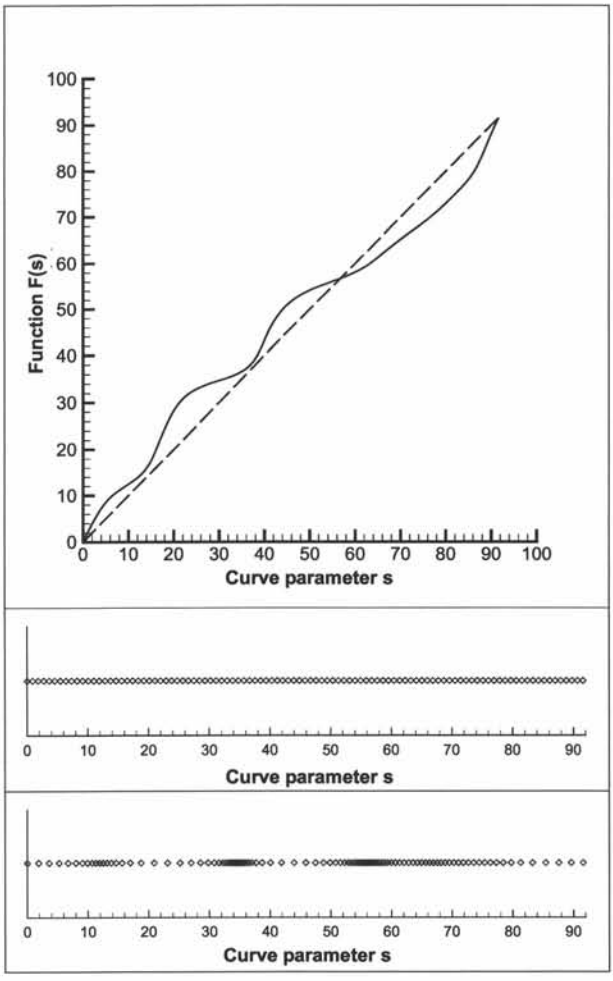

Figure 5.7: Redistribution of the nodes according to division line curvature

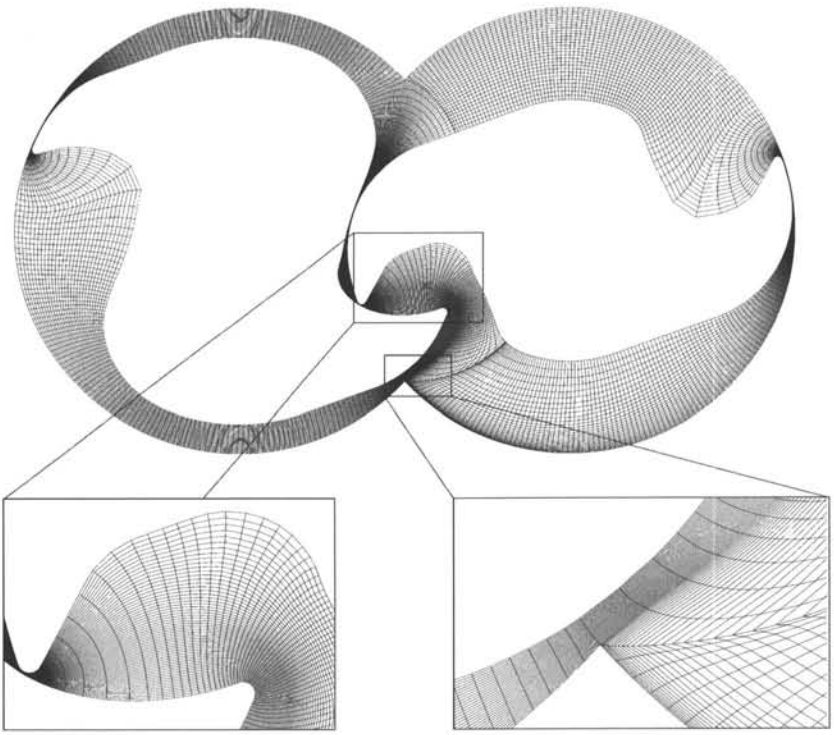

Figure 5.8: The effect on the structured grid of node redistribution on the division line and the gradient lines

5.1.3 Aspect ratio and grid resolution in the gap between rotors and casing

In the gap between rotors and casing the rectangular grid is aligned with the flow. Because of this alignment the aspect ratio of the cells can be relatively high (if the cells are elongated along the flow vectors). Nevertheless, if the gaps are extremely small the aspect ratio still becomes larger than desirable. This is often the case in screw compressor geometries. Aside from that, the tips of the rotors sometimes display geometric features to control the leakage flow that are of a very small scale (cf figure 5.1). These have to be captured by the grid and therefore a high tangential grid resolution is desired in the gaps.

In principle, both problems can be solved by raising the number of tangential nodes on the casing relative to the number of radial nodes. Figure 5.9 shows what happens if the number of tangential nodes is tripled while keeping the number of radial nodes constant.

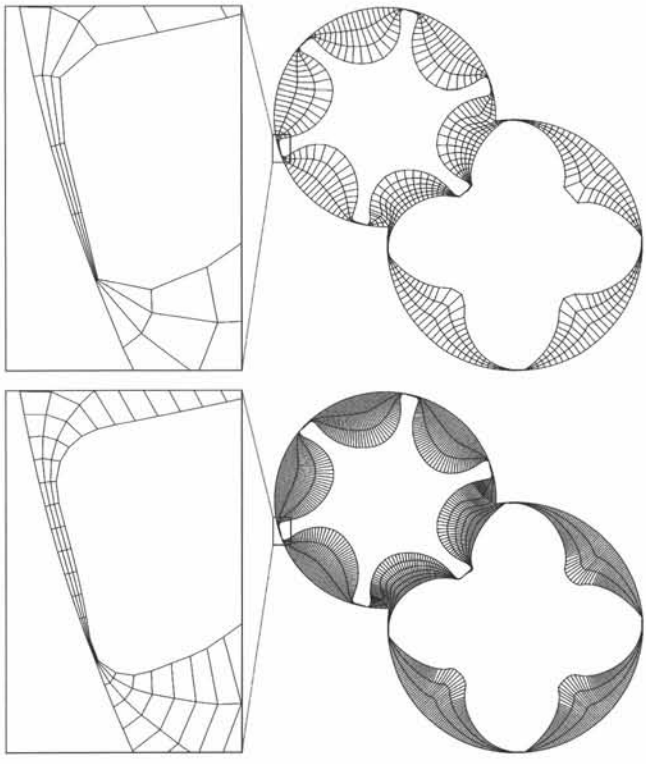

Figure 5.9: The effect of tripling the number of tangential nodes

Although the problems in the gap between rotor and casing are solved, a new zone with high aspect ratios is created in the cavity of the rotor profile (which will constitute the working chamber). The reason for this is the high ratio between the rotor diameter and gap width. A typical rotor diameter is of order 100 mm, while the gaps can be as small as 10 micron. The ratio between both is of order 10000. With such a geometry, it is impossible to eliminate all zones with high aspect ratios and maintain equidistant spacing on the casing.

Therefore the equidistant spacing is abandoned. The nodes on the casing have to be grouped closer together opposite the rotor tips. All nodes with the same tangential index i are still situated on a gradient line. Therefore grouping the nodes closer together on the casing raises the grid resolution in the rectangular grid, just as explained for the manipulation of the grid resolution in the zone of the meshing rotors in the previous section.

First, the points on the casing opposite the rotor tips are calculated. At these positions, a node will certainly be placed. Between these points, the same number of nodes is placed as if the distribution were equidistant. However, these nodes are spaced according to a quadratic function. This function is :

$$W + 4s \cdot \frac{A - W}{L} - 4s^2 \cdot \frac{A - W}{L^2} = 0 \tag{5.6}$$

In this, s is the arc length from one point on the casing to the next. L is the distance along the casing between these two points. Therefore $0 < s < L$. W is the wanted distance between two nodes at the point opposite the rotor tip. A is the maximum spacing between two nodes on the casing. This maximum spacing occurs in the middle between the two points opposite the rotor tips. By choosing the right value for A, the quadratic profile is adapted to the number of nodes and the distance L. The value of A is determined through iteration.

Figure 5.10 shows the quadratic function and its effect on the node spacing. Between the cusp and the first point opposite a rotor tip on the casing the nodes are distributed in an analogous fashion. The difference is that the profile used is not quadratic, but linear.

By choosing the number of tangential and radial nodes and the value W with some hindsight, the emergence of cells with high aspect ratios can be avoided throughout the rectangular grid. The quality of the grid is not strongly dependent on the exact choice of these values, so determining them is not a problem. In figure 5.11 the result of this procedure on the grid is shown. As can be observed, the quality of the grid is notably improved.

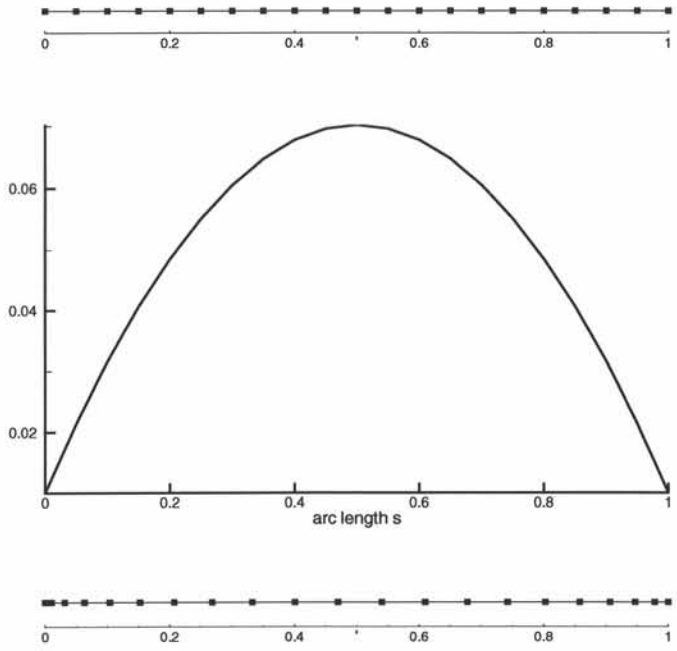

Figure 5.10: The quadratic function and its effect on the node spacing

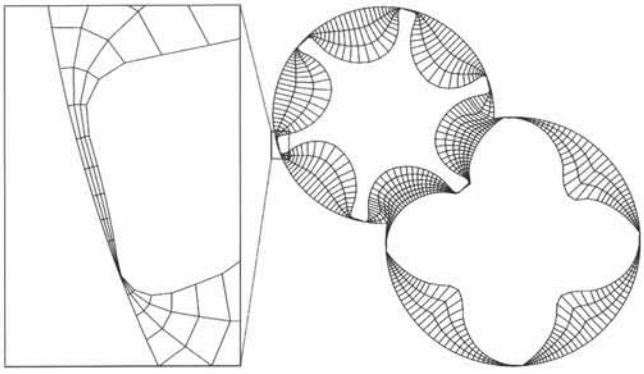

Figure 5.11: The effect of redistributing (sliding) the nodes on the casing

5.2 Local smoothing

Figure 5.12 shows the grid as it is generated with the algorithm described so far in a screw compressor geometry. It is a very good grid, especially in the various gaps. The grid is aligned with the flow field and orthogonal throughout the domain. There are no cells with excessive aspect ratios and there is nowhere a jump in cell volume. The grid is of high quality throughout the domain. Except for two zones. In these zones, local smoothing will be applied to finalize the grid generation process.

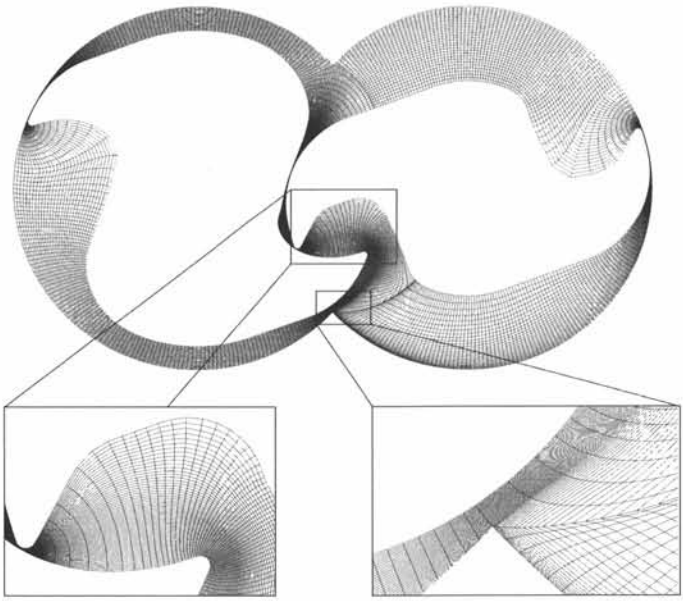

Figure 5.12: The grid as defined so far.

5.2.1 Near the cusps

Figure 5.13 shows the typical problems that can occur in the area of the cusps. There is a zone with cells with high aspect ratios. There are also cells that are skewed. This means that the angles between the cell edges are far from 90 degrees. Both problems can best be solved by applying some local smoothing. After all, the zones of inferior grid are small and localized. Furthermore these problems do not occur for all positions of the rotors.

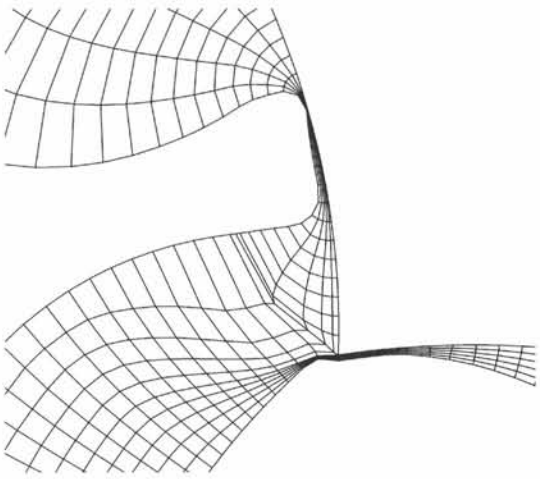

Figure 5.13: The problem area in the grid near the cusp

The zone with high aspect ratio cells is caused by the transitional part of the division line. In this segment the potential on the division line changes from the value on the main segment to the cusp value. If the rate of change of potential on this transitional segment is high, the gradient lines drawn from points on the division line are close together. This is illustrated on figure 5.13. As all nodes with equal tangential index are situated on a gradient line, and if the distance of the division line to rotor surface is relatively large, the resulting cells have high aspect ratios.

The definition of the transitional part of the division line has been determined in previous sections and cannot be adapted to solve this problem. A possible solution would be to detect the occurrence of such an event and then subsequently increase the spacing of the nodes on this segment of the division line. However, this would also influence the grid spacing in the other block of the grid (associated with the other rotor), which is not always desirable. Equally satisfying results can be obtained, with far less effort, by applying local tangential smoothing.

The tangential smoother is applied to a zone consisting of small number of nodes tangentially, starting from the cusp along the division line, and all nodes with these tangential indices radially. The number of nodes tangentially can of course be chosen freely. A good choice is a 40th fraction of the total number of tangential nodes, which typically is around 5 nodes.

The position of the nodes on the division line is maintained. The nodes on

the rotor surface with the same tangential indices are redistributed equidistantly. The other, internal, nodes are moved along the tangential lines originally defined. How much they are moved is determined by simple linear interpolation according to the distance along the gradient line.

The skewed cells are caused by the spacing of the nodes on the gradient line from the cusp (cf figure 5.13). In a more general sense, the skewed cells are caused by the potential solution and the boundary conditions to the potential problem. As explained in chapter 4, the boundary condition is a linearly varying potential, defined by the potential values in the cusps. These values were determined by demanding that the condition is fulfilled that the iso-potential line emerging from the cusp is comprised within the tangents to the casing in the cusp. In practice, this means that the tangent to the iso-potential line is almost equal to one of the tangents to the casing. In one block of the domain, the potential solution will be smooth and the grid in this block will experience no problems. However, in the other block the iso-potential lines are strongly curved. It is in fact this high curvature that is translated in the grid as skewed cells.

The problem of the skewed cells can be solved easily by moving the offending nodes on the gradient line drawn from the cusp. This is done by a radial smoother applied only to these nodes.

Consider i_c to be the tangential index of the node in the cusp. A series of splines is drawn through the nodes with tangential indices i_c+1, i_c+2, i_c+3, i_c-1, i_c-2 and i_c-3 for each radial index j. The nodes with tangential index i_c are then moved to the intersection point of these splines with the gradient line (cf figure 5.14). Figure 5.15 shows the result on the grid.

5.2.2 The rotor cavities

Because of the concave shape of the rotor cavities and because of the constant potential boundary condition on the rotor surfaces, the gradient lines fan out towards the rotor surface in these cavities. As all nodes are placed on gradient lines, the grid resolution is coarse in these zones. This is not a serious problem, as the rotor cavities make up the working chamber and no small-scale flow phenomena have to be captured in these zones.

However, the grid resolution can be so coarse that the geometric accuracy of the rotor surface is impaired. Therefore a tangential smoothing algorithm

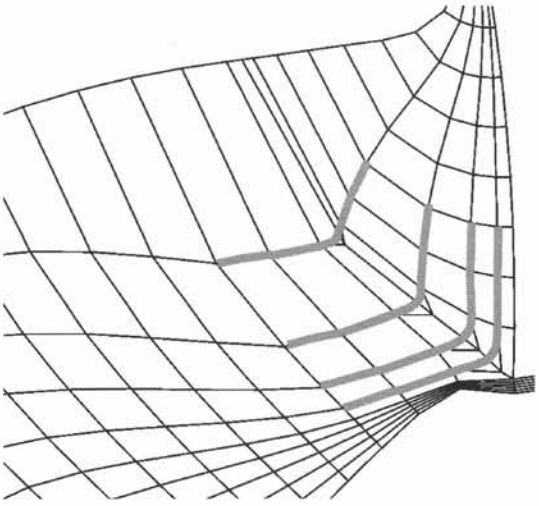

Figure 5.14: The principle of radial smoothing

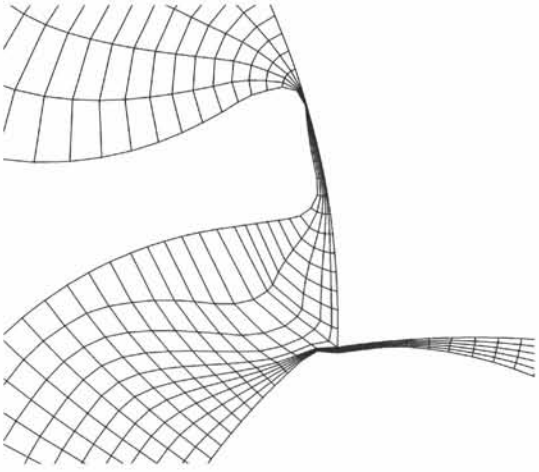

Figure 5.15: The problem area in the grid near the cusp after smoothing

as described in the previous chapter is applied to this zone. The node spacing on the casing is maintained. The nodes on the rotor surface are redistributed equidistantly and the internal nodes are moved along their tangential lines by linear interpolation. The result is shown in figure 5.16.

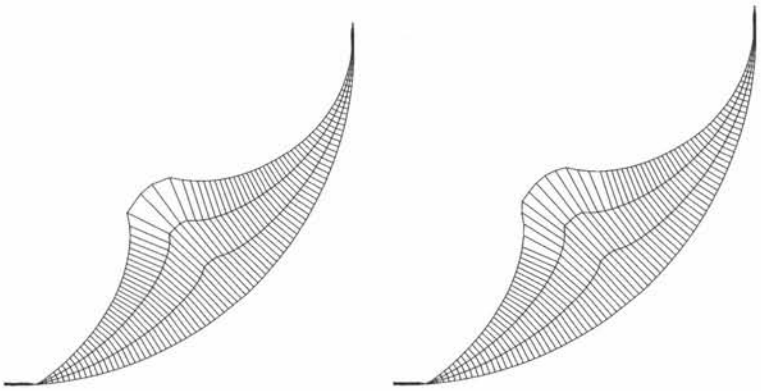

Figure 5.16: The grid in the rotor cavity before and after tangential smoothing

5.3 Conclusion

In chapters 4 and 5, a grid generation algorithm is described that can mesh a two-dimensional slice of a rotary positive-displacement machine with a structured rectangular grid. No concessions were made in the algorithm to a specific geometry and the grid generator can principally be applied to any rotary-positive displacement geometry.

Figure 5.17 shows the final grid in a tooth compressor geometry, including blow-ups of interesting zones and grid features. Figure 5.18 shows the same for a screw compressor geometry.

The rectangular grid is of high quality for any position of the rotors. The grid is orthogonal throughout the domain. There are no cells with excessively high aspect ratios and the grid cell volume changes moderately. The grid spacing is adjusted to the flow phenomena expected in the fluid flow. Geometric features of the domain boundaries that are of importance are captured by varying grid resolution. In specific in the gaps, which can be very fine, the grid is good.

In the next chapters, this grid generation algorithm will be used as part of a grid manipulation strategy. Flow calculations will be presented in a double-tooth compressor geometry and an oil-free screw compressor geometry. Numerical results will be compared with experiments.

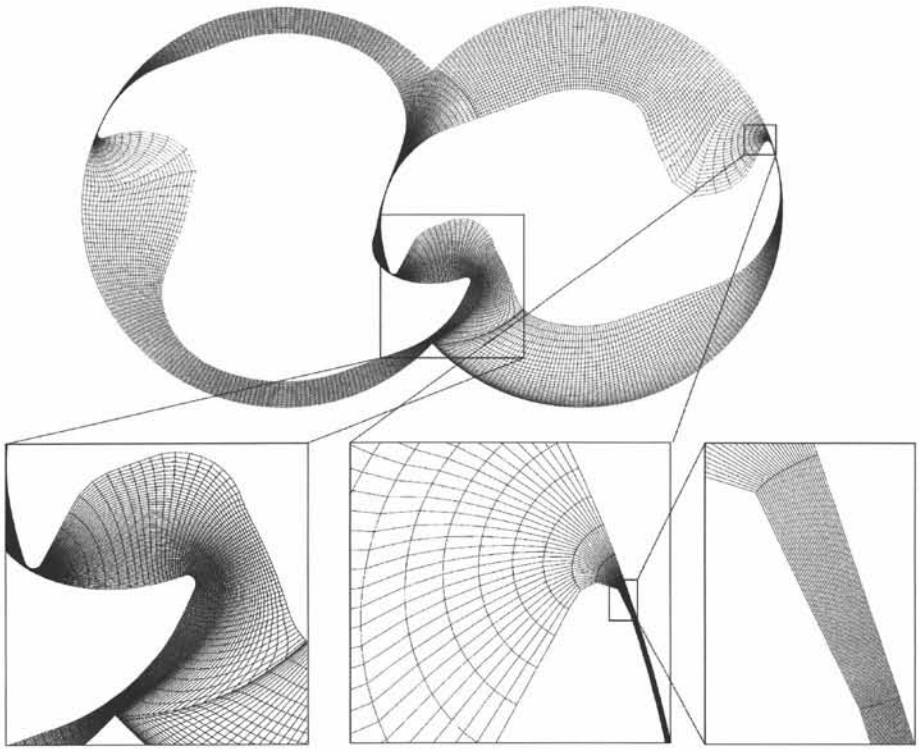

Figure 5.17: The final grid in the 2D tooth compressor geometry

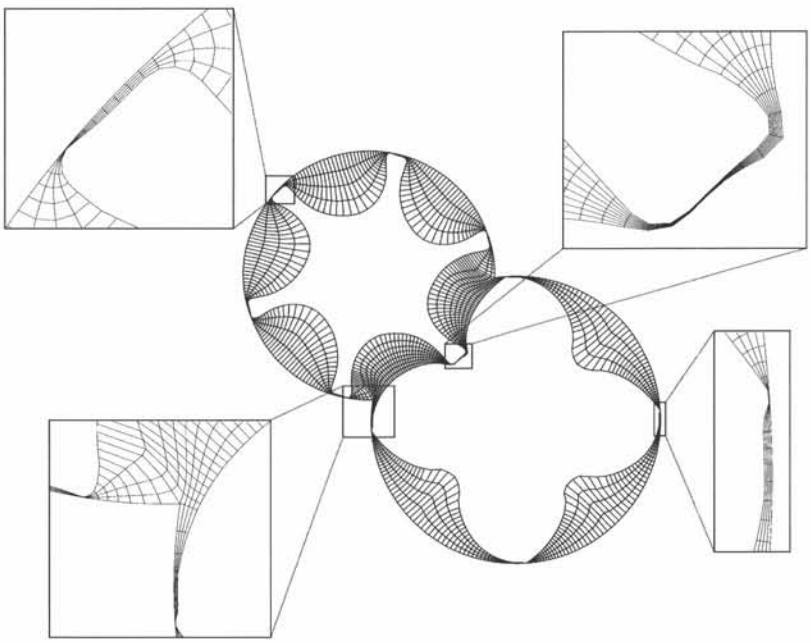

Figure 5.18: The final grid in the 2D screw compressor geometry

Chapter 6

ALE Calculations: Flow Calculation in a Double-Tooth Compressor

In the previous two chapters, a structured rectangular grid generator was described that can be used to mesh rotary positive-displacement machines. In the next two chapters, this grid generator is implemented in a grid manipulation algorithm to perform flow calculations in a tooth compressor geometry and a screw compressor geometry. These flow calculations and comparison of the results with experimental results will demonstrate the potential of the algorithm.

The first geometry, considered in this chapter, is a double-tooth compressor.

6.1 Background

Parts of this section are derived from the book 'Industrial Compressors' [28].

Rotary tooth compressors, also sometimes known as rotary lobe compressors, are two shaft rotary meshing action compressors. They have many similarities to oil-free screw compressors. They are a relatively new development and are manufactured by only a few companies. Their main application is the

supply of oil-free air. They are relatively small volume compressors. Thus they bring many of the advantages of oil-free screw compressors to a size range in which the oil-free screw compressors are either too expensive or too inefficient.

Tooth compressors have rotors with either one tooth or two teeth. A typical single tooth compressor rotor geometry is depicted in figure 6.1. A double-tooth compressor rotor geometry is shown in figure 6.2. The double-tooth geometry is inherently balanced, but the single-tooth design requires additional balancing on the shafts.

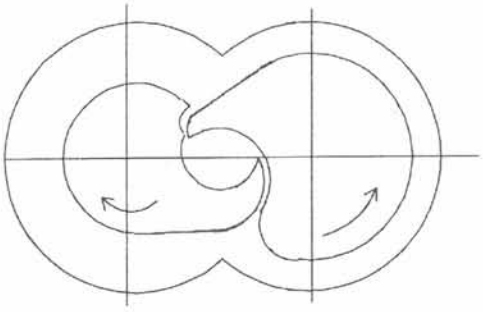

Figure 6.1: A typical single-tooth compressor geometry

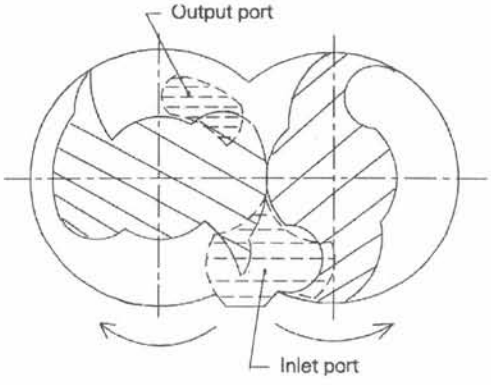

Figure 6.2: A typical double-tooth compressor geometry

The rotors of a tooth compressor are two-dimensional. They are extruded straight in the axial dimension. Therefore there are no axial forces on the shafts. The outlet port, and sometimes part of the inlet port, is positioned in the axial direction. Thus the geometry of the tooth compressor is three-dimensional (cf figure 6.3). A two-dimensional flow calculation is not possible because of the position of the outlet (and sometimes inlet) port.

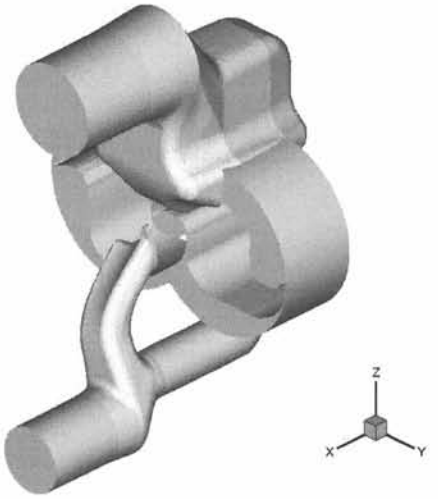

Figure 6.3: A typical double-tooth compressor geometry

Figures 6.4, 6.5 and 6.6 depict the compression cycle of the single tooth design of figure 6.1. Figure 6.4 outlines the suction cycle from start to end. The outlet section is added to this illustration, but it is still covered by the rotors. Immediately after the end of one suction cycle, the next cycle begins. The inlet mass flow is virtually continuous (but not constant !).

The end of the suction cycle determines the maximum volume of the working chamber. Next the working chamber is reduced in volume. Figure 6.5 shows the rotor position during the compression phase. The outlet port is still covered by the rotors. The gas is pressurized due to internal compression.

Figure 6.6 illustrates the situation where the outlet port is uncovered and gas is being discharged in the outlet. All the gas is displaced by the rotors. There is no clearance volume. Due to the internal compression phase the outlet mass flow is not continuous. Nevertheless, as the inlet and the outlet port can never be in direct contact, there is no need for valves.

As the outlet port is not uncovered immediately at the end of the suction phase, internal compression takes place. The amount of internal compression is determined by the shape of the inlet and outlet section. It is defined as an internal volume ratio or internal pressure ratio. Under- and overcompression may occur. Reference is made to chapter 1 for more information on this topic.

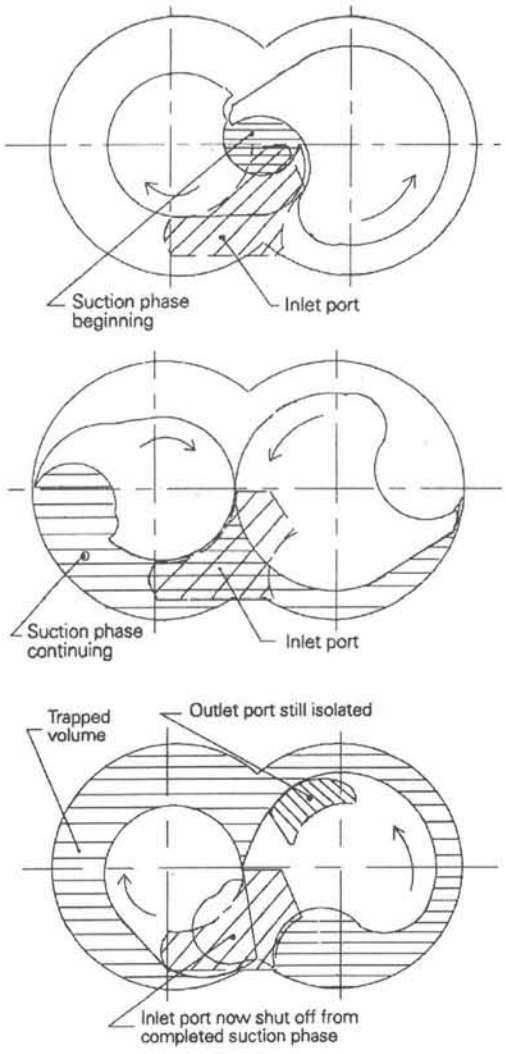

Figure 6.4: The suction cycle for the single-tooth compressor geometry in figure 6.1

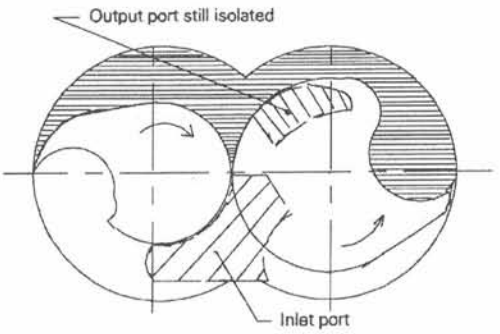

Figure 6.5: The internal compression stage for the single-tooth compressor geometry in figure 6.1

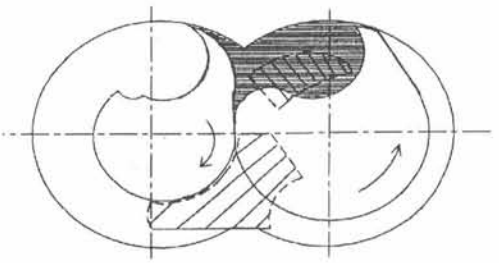

Figure 6.6: The discharge stage for the single-tooth compressor geometry in figure 6.1

Single-stage tooth compressors are marketed for a pressure rise from 1 bar (atmosphere) to up to around 3 bars. The discharge temperature is limited to about 500 K. In two-stage tooth compressors with intercooling, pressure can be raised up to about 10 bar.

Even though the tooth compressor is forgiving for liquid carry-over, the most common application is for oil-free air duty.

The oil-free duty has some implications. As no oil is injected in the compressing gas, the gas is not (effectively) cooled during compression. There is no lubrication and the various leakage paths are not sealed by oil. This means that the gaps between the rotors and between the rotors and the casing must be made as small as possible to reduce leakage. The deformation of the casing due to heating must be limited. The casing is cooled by water or oil to this purpose, yet the discharge temperature is still limited. The effect of this cooling on the compressing gas is negligible because of the very short residence time of the gas in the machine. As there is no lubrication, the two rotors may never make contact. Because of the very small gaps, both shafts have to be driven via a rigorous timing gear.

The most important repercussion from oil-free duty is however that the internal compression of the gas is not cooled. This seriously reduces the compression efficiency. To maintain a reasonable overall efficiency, the compressor is operated in a relatively small band around optimal efficiency.

A typical speed range for tooth compressors is 3000 to 6000 rpm. Single-tooth compressors have a larger displacement per revolution than double-tooth compressors. However, double-tooth rotors are inherently balanced, while single-tooth rotors are not. This limits single-tooth compressors to a flow rate of about 350 m^3/h to 800 m^3/h. Double-tooth compressors are capable of higher rotational speeds and can have a flow rate of up to about 2500 m^3/h.

6.2 The grid manipulation algorithm

The geometry of the tooth compressor through which flow will be calculated, is shown in figure 6.3. It is a double-tooth geometry. The evolution of the working chamber as the rotors rotate is illustrated in figure 6.7.

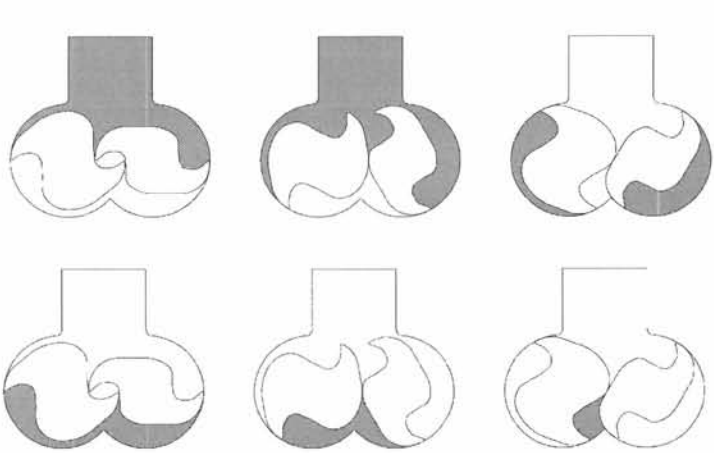

Figure 6.7: The evolution of the working chamber for the double-tooth compressor geometry in figure 6.3

The grid in the flow domain consists of four blocks. An exploded view is shown in figure 6.8. The grid in the inlet port and the outlet port is stationary. It is not handled by the grid manipulation algorithm. Only the two blocks of the grid making up the casing of the machine will be deformed. These two blocks are depicted in figure 6.9.

Geometrically, the casing is the extrusion of a two-dimensional slice in the axial dimension. The three-dimensional structured grid can be generated in an analogue fashion. First a number of slices of the casing are made orthogonal to the rotation axes. These slices are meshed with a two-dimensional block-structured rectangular grid using the grid generator described in the previous chapters. In fact, these grids are identical, except for the numbering of the nodes, so the grid generator has to be applied only once. Next these two-dimensional grids are connected, thus creating hexagonal grid cells. The resulting grid is shown in figure 6.10.

Now consider a rotation of the rotors. The grid in the casing has to be adapted. The three-dimensional grid is block-structured and structured in each block. This means that if a new grid is generated for the new position of the rotors with the same number of radial, tangential and axial nodes, this new grid has the same topology as the old grid. It is possible to replace the old grid with the new grid for the new rotor positions. To the flow solver, it seems as if the nodes have been moved to a new position accommodating the rotor rotation without changing grid topology. The effect is thus the same as actually moving the nodes. This method allows the solver to calculate the flow using the ALE formulation of the flow equations.

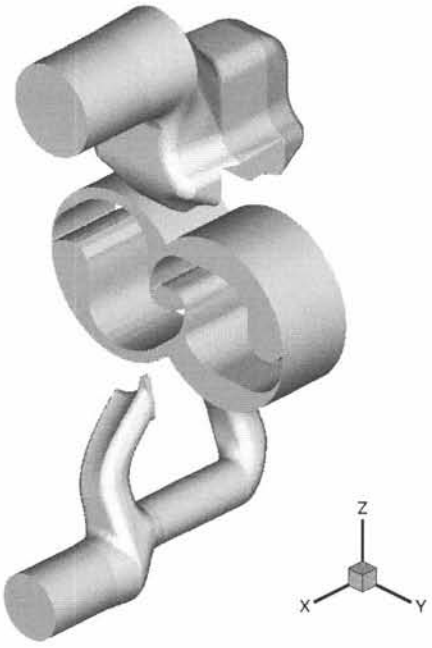

Figure 6.8: Exploded view of the double-tooth compressor geometry in figure 6.3

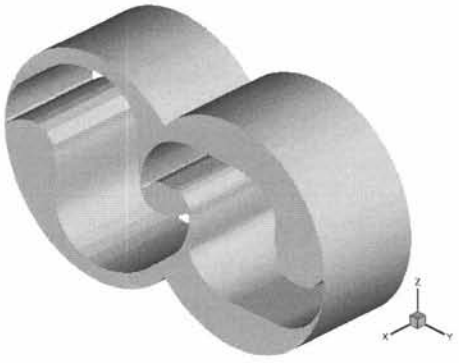

Figure 6.9: The casing of the double-tooth compressor geometry in figure 6.3

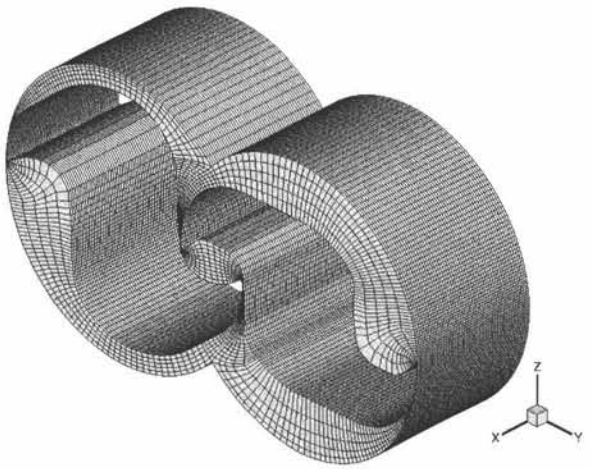

Figure 6.10: Hexagonal structured grid in the casing of the double-tooth compressor geometry in figure 6.3

This means that the grid manipulation algorithm can consist of generating a new two-dimensional grid in a casing slice for each time step and then rebuilding the three-dimensional grid from the 2D grid. Thus the problem of moving a three-dimensional grid is reduced to generating a two-dimensional grid for each rotation.

However, the numerical effort can be reduced even further. Assume that before the flow calculations are started, a set of two-dimensional grids is generated for each degree rotation of the rotors. Call these grids the root grids. As the geometry is a double-tooth compressor, this set would consist of only 180 grids. For each time step in the calculations, the two-dimensional grid corresponding with that rotor rotation could be obtained through linear interpolation between two consecutive root grids. Because the rotation of the rotor profiles between two root grids is small (1 degree), it is safe to assume that there is little grid quality degradation and the quality of the interpolated grid is not impaired. However, the interpolated grid is not geometrically correct. After all, a rotation of a point around a center is not the same as the linear interpolation between two points rotated around that center. Therefore, the boundaries of the flow domain are not exactly imposed. The error is the largest for an interpolation midway between two root grids. It is possible to estimate this error. Figure 6.11 is used as an illustration.

Consider A_0 to be a point A rotated around C over $\alpha/2$ degrees. B is the point A rotated over α degrees around C. Point A_l is the linear interpolation between A and B.

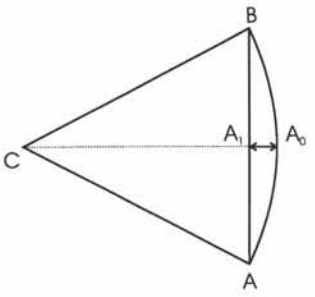

Figure 6.11: Rotation around a centre versus linear interpolation

The difference between A_0 and A_l can be readily determined. It is :

$$\|CA\| \cdot \left(cos\frac{\alpha}{2} - \frac{1}{2}\left(cos\,\alpha + cos\,0\right);\ sin\frac{\alpha}{2} - \frac{1}{2}\left(sin\,\alpha + sin\,0\right)\right) \qquad (6.1)$$

For α being 1 degree, the error relative to the radius $\|CA\|$ is 0.0038 %. This is a very small error, compared to other errors made during spatial and temporal discretization. Therefore, the conclusion is that the interpolated grids may be used as if they were directly made by the grid generator.

6.3 Calculation : set-up

The geometry that is used for the validation calculation is depicted in figure 6.3. It is a double-tooth compressor, consisting of a casing with two rotors, an inlet port and an outlet port. The rotor diameter is 57.9 mm and the casing has a depth of 50.86 mm. The rotational speed of the rotors for the case calculated is 5500 rpm. The gas to be compressed is air. It is pressurized from 1 bar abs (atmosphere) at the inlet to 3 bar abs at the outlet. There is no oil injection, so the internal compression is not cooled. The casing is cooled via a series of canals through which water is fed.

The three-dimensional grid consists of 4 blocks, namely the inlet port, the outlet port and two blocks in the casing.

The inlet and the outlet port geometry are real and unsimplified. It is a quite complex geometry, but the boundaries, and therefore the grid, are stationary. These blocks are meshed using an unstructured tetrahedral mesher available in the commercial package ProAm (CD Adapco). The grid is not adapted near the walls for boundary layer calculation. Near the actual inlet and outlet section, the grid is hexagonal to better suit the boundary condition that will be imposed. The grid in the inlet port and the outlet port is depicted in figure 6.12. The grid in the inlet port consists of 324482 cells. The grid in the outlet port has 220249 cells.

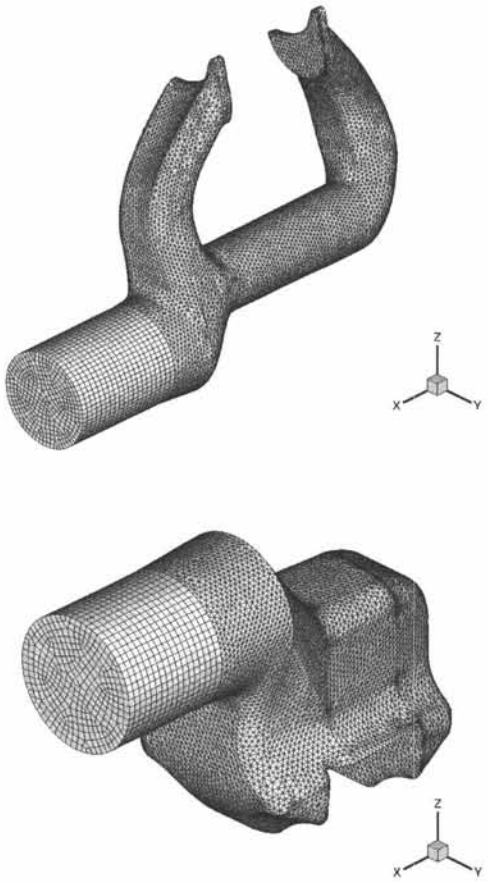

Figure 6.12: 3D grid in the inlet and outlet ports

The grid in the casing is structured and rectangular. It is constructed using the 2D grid generator described in chapters 4 and 5 as explained in the previous section. The two-dimensional domain is shown in figure 6.13. As the

tooth compressor delivers oil-free air, there is no oil lubrication between the rotors. The tooth compressor is fitted with a timing gear to ensure that the rotors never make contact. There is at all times a gap between both rotors. From a grid generation standpoint this is a good thing. It makes it easier to maintain grid topology.

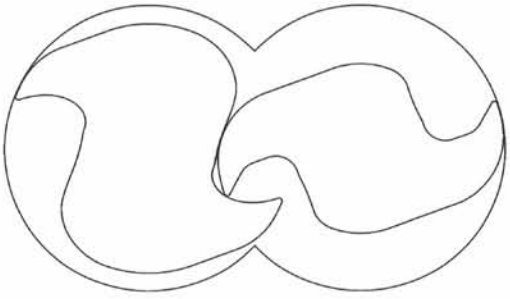

Figure 6.13: 2D slice of the casing

The two-dimensional grid in the casing is generated using the algorithm described in the previous chapters. The nodes on the division line between both blocks are distributed according to the curvature of the division line with an underrelaxation factor of 0.8. The distribution is a mix of purely according to curvature (80 %) and equidistant spacing (20 %). The nodes on the casing are fixed. They do not slide tangentially to locally raise the grid resolution near the rotor tips. In this case, there is no need for the tangential redistribution as described in chapter 5. The gaps between the rotors and the casing are relatively wide (as compared to an oil-free screw compressor) and the rotor tips have no small-scale geometric features to control the gap leakage flows. This means that the gaps can be sufficiently resolved using an equidistant tangential spacing on the casing. As this calculation is a first step in validation, this feature has not been added to the grid generation. The local smoothing described in chapter 5 is applied. Near the cusps, skewed cells and cells with high aspect ratios may occur. Smoothing is necessary. The cavity of the rotor profiles is strongly concave. Local tangential smoothing is needed to ensure geometric accuracy.

Each block of the grid is made up of 6 nodes radially and 200 nodes tangentially. A grid with 6 nodes radially is sufficient to capture the profile of the leakage flow in the gaps between rotors and casing. This leakage flow is a mixture of a pressure driven Poiseuille flow and a Couette flow between two almost parallel walls. The rotor tip speed is around 30 m/s, while the fluid velocity in the gaps is expected to be around 200 m/s. The parabolic profile of the Poiseuille flow will be predominant. An illustration of what the velocity

profile might look like is shown in figure 6.14. Six grid points in the gap is sufficient to capture the velocity profile.

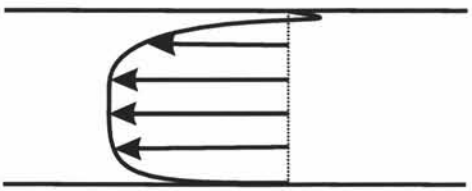

Figure 6.14: Illustration of pressure-driven Poisseuille flow

140 nodes tangentially equidistantly distributed on the casing can resolve all geometric features of the gap between rotors and casing. With six nodes radially, the aspect ratio in the gaps is also acceptable. As the gaps are not extremely small, the aspect ratio of the cells in the cavity of the rotor profiles (the working chamber) is also acceptable. Of the 200 tangential nodes of each block, 60 nodes are placed on the division line between both blocks. This number of nodes is enough to resolve the meshing area of the rotors. Figure 6.15 illustrates this.

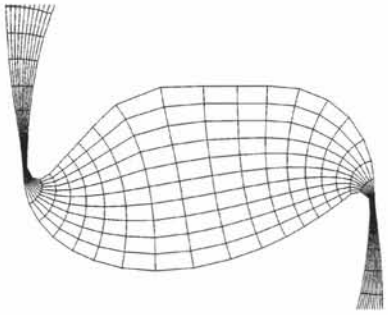

Figure 6.15: 2D grid in the rotor meshing area

The quality of the 2D grids constructed along these lines is good. As an illustration, consider the grid generated for a rotor rotation of 0 degrees (cf figure 6.16).

In figure 6.17, the aspect ratio of all grid cells is depicted. The maximum aspect ratio is 70. The cells with highest aspect ratios appear in the gaps between rotors and casing. It is not a problem to have higher aspect ratios in these cells, as they are aligned with the flow. In the rest of the domain, the aspect ratios are well within acceptable limits.

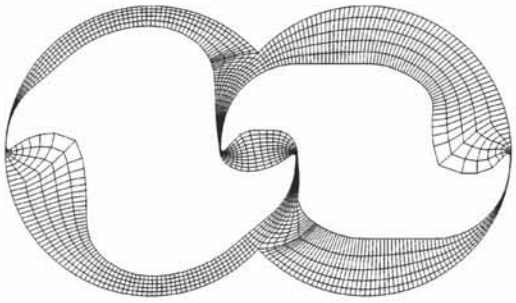

Figure 6.16: 2D grid in the casing; rotation zero degrees

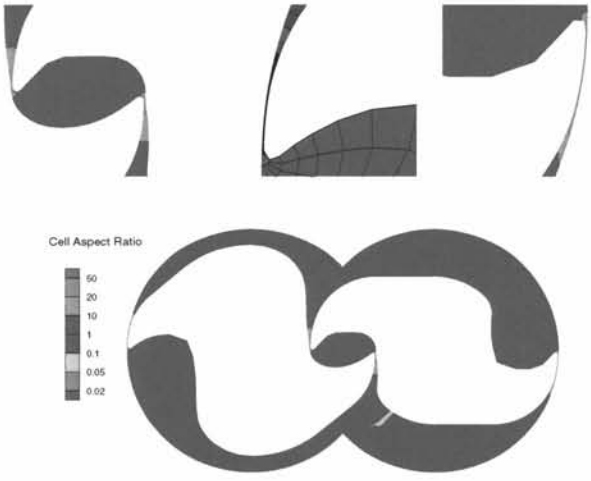

Figure 6.17: 2D grid in the casing; contours of aspect ratio

In figure 6.18, the volume (area) of the grid cells is shown. The volume of the cells changes gradually throughout the domain. The cells with the largest volume are located in the cavity of the profiles. The grid spacing is finer near the rotor tips and where the leakage flows will form. The grid resolution is well adapted to the geometry of the domain and to the flow phenomena that are expected to occur.

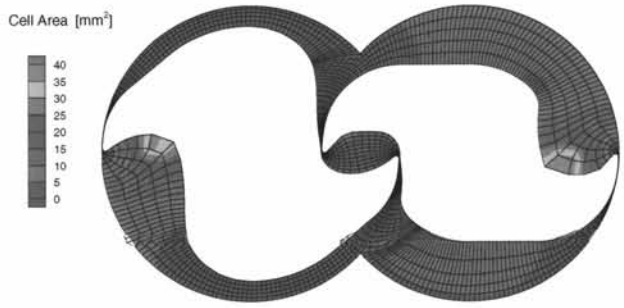

Figure 6.18: 2D grid in the casing; contours of cell volume

Figure 6.19 shows contours of grid node movement for a rotor rotational of 1 degree. For a rotational speed of 5500 rpm, the maximum grid node velocity is of order 150 m/s. It is located in the cavity of the profiles. At 5500 rpm, the tip speed of the rotor is around 30 m/s. In the gaps, the leakage flow is expected to reach a velocity of around 200 m/s. The grid velocity is right within this range. Therefore, the grid velocity will not introduce eigenvalues of a different magnitude in the flow equation matrix. The movement of the grid will not affect the stiffness of the matrix.

Figure 6.19: 2D grid in the casing; contours of node displacement

Based on these considerations, the grids are suited for the calculation at hand. A set of 180 root grids, each one degree rotation apart, is generated.

The two-dimensional rectangular grids were generated on a Compaq DS20 machine using one processor. The generation time is mainly dependant on the number of iterations needed to determine adequate potential boundary conditions on the casing. A typical generation time breaks down as follows. It takes circa 400 seconds to generate the triangular unstructured grid on which the potential solution is solved. A typical grid consists of 28594 nodes. It is locally refined near the cusps, near the rotor tips and in the gap between both rotors. The solution of the potential equation, including determining the boundary conditions, takes circa 500 seconds. The actual generation of the rectangular grid takes about 50 seconds. This makes a total construction time of around 950 seconds or 15'50". Note that although the grid generation is here broken up in three steps for clarity, the generation is in effect completely automatic. As a comparison, the solution of one time step of the flow equations takes 141 seconds. The calculation is performed on one and a half linux boxes of 2.4 GHz dual-processors (so 3 processors).

Based on the two-dimensional rectangular grid, a three-dimensional hexagonal grid is created in the casing by stacking two-dimensional grids equidistantly. In the axial direction, the grid consists of 49 cells. This assures an aspect ratio in the axial direction of around one. The grid in the casing thus has a total of 2x5x200x49 = 9800 cells.

The grid in the casing is joined together with the grid blocks in the inlet and the outlet port using arbitrary sliding interfaces. This means that the blocks are allowed to slide over each other. At each time step, the grid faces that make up the interface are determined and fluid flow is allowed through them from one block to the other. The other cell faces of the sliding interface are considered to be a wall and get the appropriate boundary condition. The interface is arbitrary in the sense that the cell faces of the interface do not have to be positioned one on one. A cell face can be part interface and part wall and the boundary condition applied to it will be adjusted to accommodate. The arbitrary sliding interface is a feature of many commercial CFD packages, and also the one used for this simulation. It will not be handled more in depth here. For further interest, reference is made to general literature, and more specific the user guide of the CFD package used [1].

By joining all grid blocks together, the final 3D grid is finished. It is depicted in figure 6.20. The total number of cells in the grid is 644731.

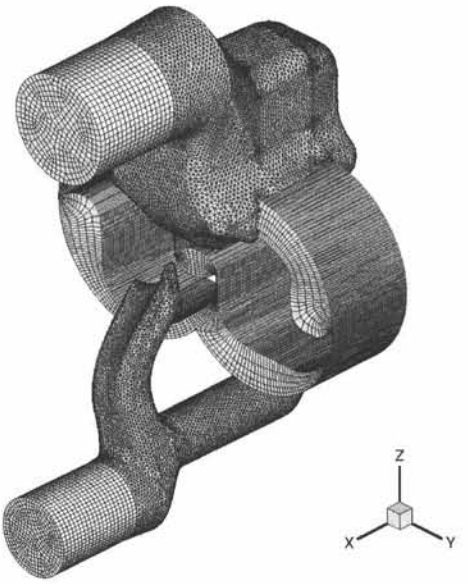

Figure 6.20: 3D grid in the double-tooth geometry of figure 6.3

The flow calculations are performed by a commercial CFD code that has been extended with a user-defined function that handles the grid movement. The package used is Computational Dynamic's StarCD, version 3.20. StarCD is a co-located cell-centered finite-volume code. It is developed for structured hexagonal grids. However, it is capable of using tetrahedral grids as well. StarCD is capable of ALE calculations. The ALE formulation of the flow equations, including the space conservation law, is discretised without truncation. The spatial discretization scheme that is used for the calculations is the Monotone Advection and Reconstruction Scheme (MARS). This is a monoticity-preserving TVD limiter scheme developed for the StarCD code. The temporal discretization is fully implicit. The set of algebraic equations obtained through these discretization schemes is solved using a modified PISO predictor-corrector scheme.

For the calculation, some simplifications have been applied to the case.

Firstly, some thermal effects are neglected. The expansion of the rotors and the casing due to heating is not incorporated. This would involve a large fluid-structure interaction calculation. The only important characteristic that is affected by the deformation is the size of the gaps. In the calculation it is considered to be constant. As the gap size should be measured under load conditions, it is not possible to accurately determine it through experiments.

The value used is in fact an educated guess. As the gap size influences the leakage flows and thus the efficiency of the compressor, this is definitely a drawback. However, the calculation presented here is meant as a validation of the grid manipulation algorithm. It should be kept in mind though that a small deviation from experimental results is to be expected.

Furthermore, the walls are considered adiabatic. This is true in reality for the rotor surfaces, but the casing is cooled by a water mantle. However, this cooling is aimed at reducing the heat deformation of the casing, not at cooling the compressing gas. In fact, the residence time of the gas in the casing is so short (10.9 msec for 5500 rpm) that it is not possible to extract heat from the gas through external cooling. Therefore this approximation is valid.

A third and final approximation is that no turbulence model is used. This is mainly done to cut calculation time, but can be justified.

In the compression chambers the compression is achieved through a reduction in volume. The flow patterns are mainly driven by pressure gradients that are the result of the volume change of the working chamber and the sudden expulsion of pressurized gas in the outlet port. The influence of turbulence on the flow field here is smaller than one might expect at first. It should be noted that in a conservative CFD code, energetically all mixture losses in the fluid flow are inherently implied in the flow equations, even without a turbulence model. The only energy loss that is not correctly covered, is the friction loss between the fluid and the walls. This loss is very small compared to all other energies exchanged.

A similar train of thought can be adhered for the outlet port, and to lesser extent the inlet port. The flow patterns here are also mainly driven by pressure gradients caused by the expulsion, respectively the suction, of fluid in the compression chamber.

The leakage flows through the gaps between rotor and casing and between the rotors mutually are even laminar. Due to the small size of the clearances, the Reynolds number is surprisingly small and the flow can safely be considered to be laminar.

The compressor operates without oil injection. Therefore the fluid is single-phase and there is no need for a multi-phase model in the calculations. The rotational speed is 5500 rpm. As compressed fluid, air is defined as an ideal gas. The boundary condition at the inlet and the outlet is a pressure boundary.

At the inlet a pressure is imposed of 1 bar absolute. The temperature of the entering gas is 293 K. At the outlet, a pressure of 3 bar is imposed. The temperature of re-entering fluid is determined to be 415 K. This is an educated guess based on the expected efficiency of the machine. In practice, the pressure imposed at the outlet at start-up is 1 bar absolute. It is linearly raised to 3 bar absolute during the first 360 degrees rotation to avoid too strong shock waves running up and down the outlet port at start-up.

Thus the validation calculation is completely defined.

6.4 Calculation : results

The calculation result presented here is meant as a validation of the grid manipulation strategy. As a numerical result, only the volumetric efficiency is compared with experiments. However, the results do illustrate the convergence of the flow solver and the conservation of mass, energy and momentum. As such, it is possible to conclude that the moving grid provided to the CFD package is of sufficient quality to perform ALE calculations in the tooth compressor geometry considered. The results presented here also serve as an illustration of the data that becomes available through the use of CFD.

In figure 6.21 the mass flow rate throught the inlet and the outlet of the machine is plotted. One can clearly distinguish the compression cycle with a length of 180 degrees.

The volumetric efficiency corresponding with the plotted mass flow rate is 48%. This is much lower than the experimental result, which is 73.7%. The leakage flows are severely overestimated. This means that probably the gap sizes have been estimated too large. A parametric study could give indications for a more realistic gap size. However, the simulation presented here is merely to illustrate that the grid manipulation algorithm allows such calculations. Therefore this parametric study is not performed.

The adiabatic efficiency obtained numerically is 45.8%. This value is very low, yet this is no surprise as the numerically obtained volumetric efficiency is also very low. As discussed previously, leakage flows have a very large negative impact on the compression efficiency.

In figure 6.22 the power consumption is plotted. Both rotors consume

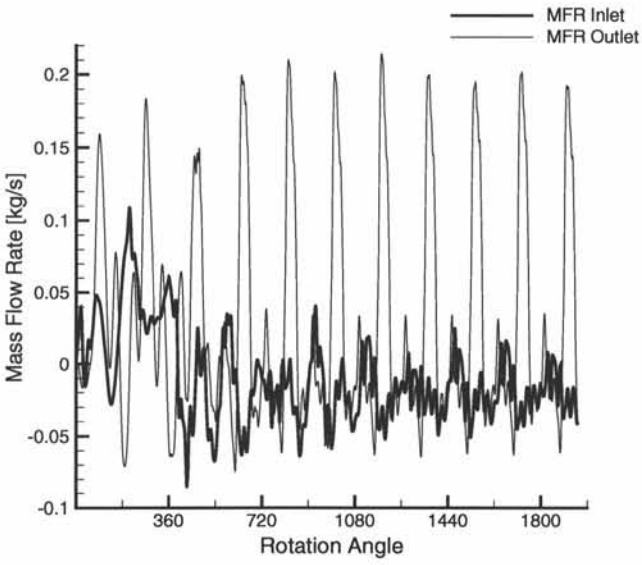

Figure 6.21: Evolution of mass flow rate through the inlet and the outlet

more or less the same amount of power. As no oil is injected into the working chambers, rotor contact has to be avoided at all cost. This is realized by driving both rotors via a timing gear. The data from plot 6.22 could be used to dimension this timing gear, as from this plot can be derived how much power must be transfered by the timing gear.

In figure 6.23 and figure 6.24 the radial force excercised by the gas and the direction by which this force is oriented on the right, respectively left, rotor is plotted.

Note that although the compressor simulated is a double-tooth compressor, and thus inherently balanced, the pressure of the compressed gas nevertheless results in a pulsing load on the axes. The radial bearings on the axes must be dimensioned to withstand this pulsing load.

The axial force is plotted in figure 6.25. Due to the symmetry (of the housing) of the compressor, this force is very close to zero.

In figure 6.26 the contours of pressure are plotted in a plane perpendicular to the axis. The rotation at that moment is 1942 degrees.

In figure 6.27 the contours of pressure are plotted in the outlet port. One can clearly distinguish a pressure wave running down the outlet port.

In figure 6.28 a plot is shown of velocity vectors in the same plane and at the same time as in figure 6.26. Blow-ups are added of the gap between rotors and of the area around the rotor tips.

6.5 Conclusion

From the calculation presented it is concluded that the grid manipulation strategy as described above is sufficiently robust. The two-dimensional grid generator presented in chapters 4 and 5 stood up to the test. The moving grid presented to the compressible flow solver is of good quality, allowing an ALE calculation in a geometry of the complexity of a tooth compressor. In the next chapter, the grid manipulation is tested on the most challenging geometry of all rotary positive-displacement machines, namely an oil-free screw compressor.

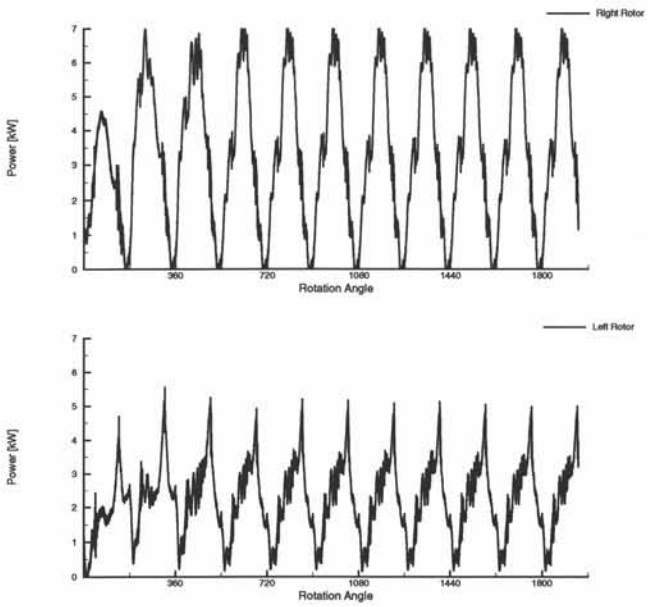

Figure 6.22: Evolution of power consumed by the right and the left rotor

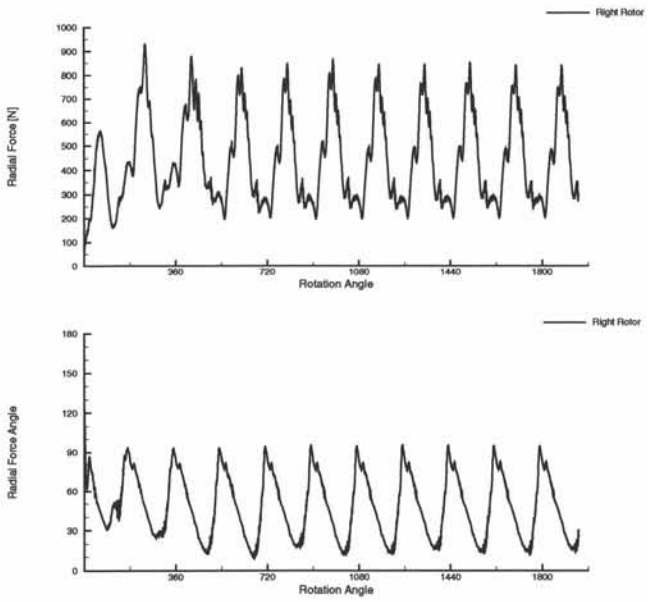

Figure 6.23: Evolution of radial force on the right rotor; magnitude and direction angle

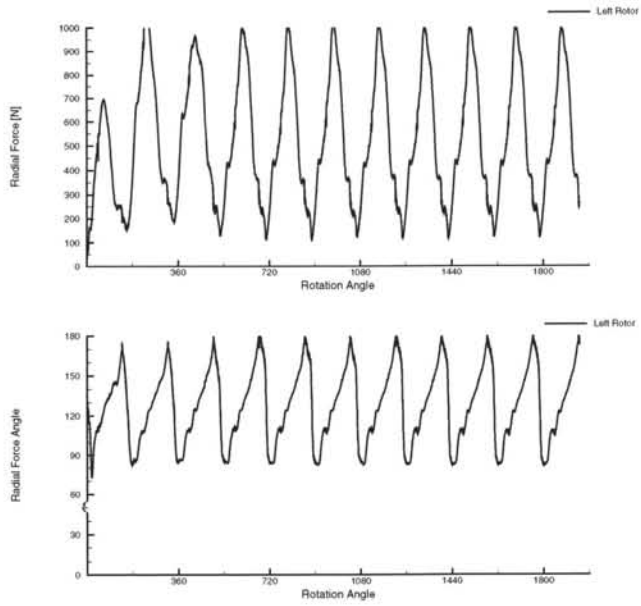

Figure 6.24: Evolution of radial force on the left rotor; magnitude and direction angle

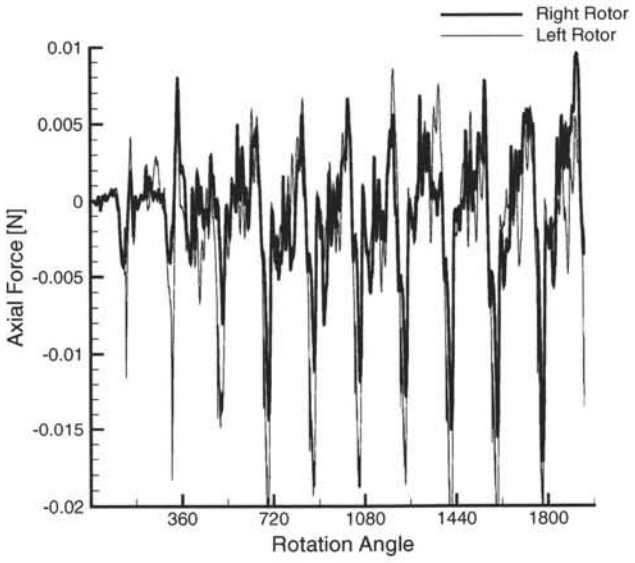

Figure 6.25: Evolution of axial force on the left and the right rotor

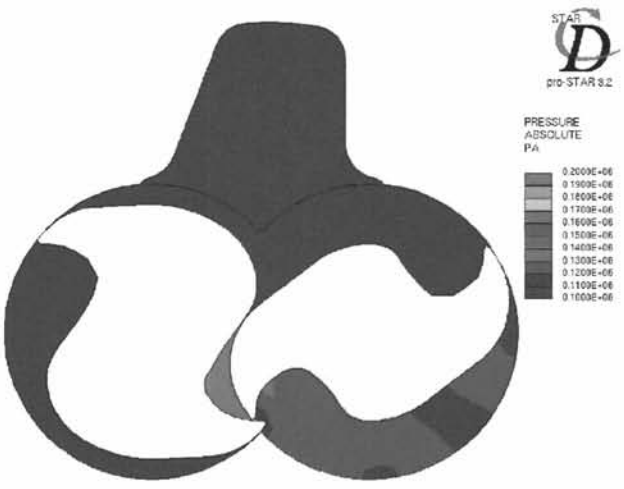

Figure 6.26: Contours of pressure in the working chamber; rotation 1942 degrees

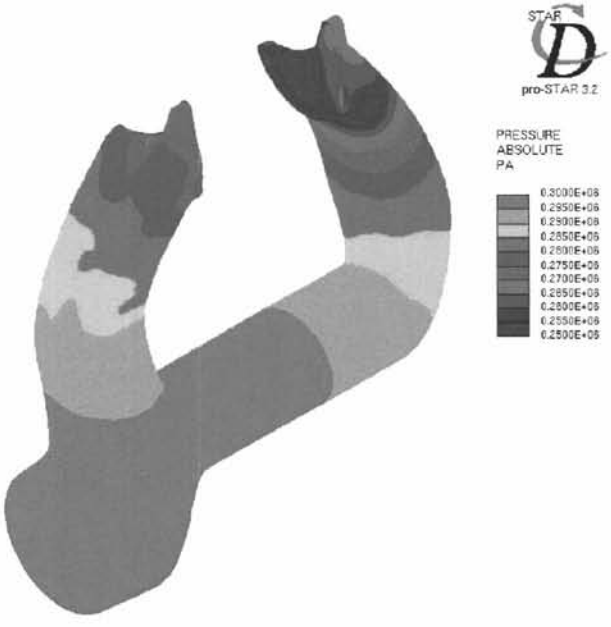

Figure 6.27: Contours of pressure in the outlet port; rotation 1942 degrees

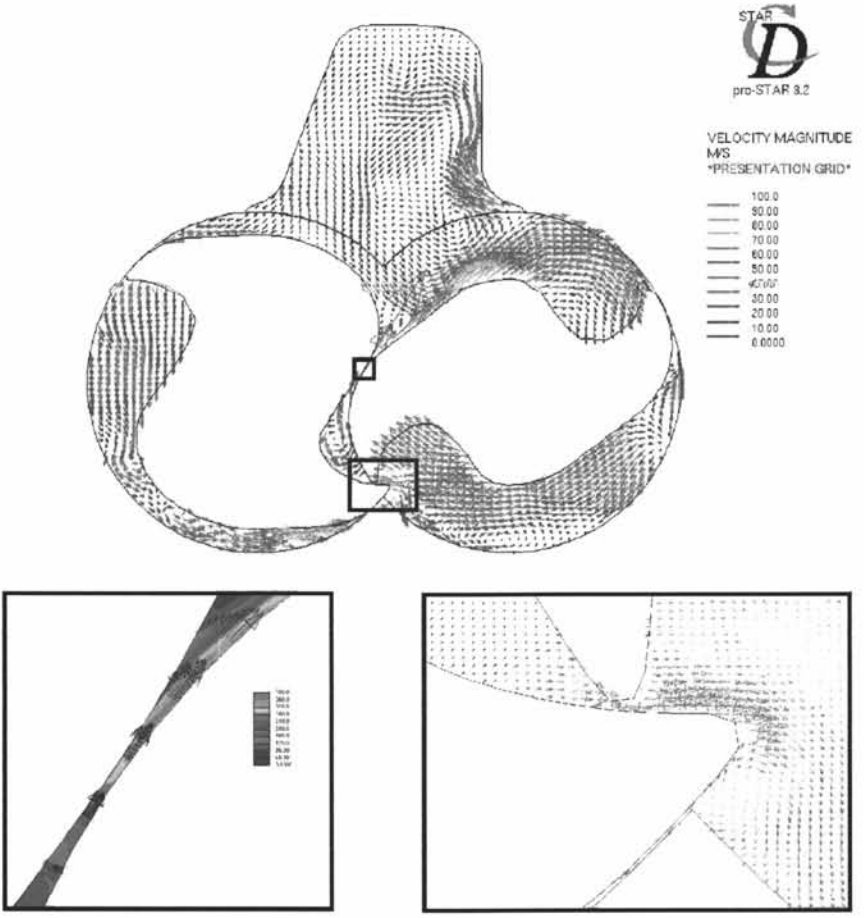

Figure 6.28: Velocity vectors in the working chamber; rotation 1942 degrees

Chapter 7

ALE Calculations: Flow Calculation in an Oil-Free Screw Compressor

In chapters 4 and 5, a structured rectangular grid generator was described that can be used to mesh rotary positive-displacement machines. This grid generator was implemented in a grid manipulation strategy used to perform ALE calculations in a tooth compressor in the previous chapter.

In this chapter, the same grid manipulation strategy is used for calculations of flow in a screw compressor geometry. Of all rotary positive-displacement compressors, the screw compressor is the most commonly used. Its geometry is also the most complex. That is why this geometry was chosen for the final validation calculations.

7.1 Background

This section discusses twin-screw compressors [29]. As the single-rotor type of screw compressor is rarely used, the word 'twin' is usually omitted and the term 'screw compressor' is generally taken to apply to twin-screw compressors.

There are two different types of screw compressor, the oil-free or dry type and the oil-injected or wet type. The characteristics and designs of each type

are so different that they in effect can be considered to be different types of compressors. However, as they both use exactly the same principle of operation, some features are identical. These common features are discussed first.

The geometry chosen for the validation calculation is an oil-free screw compressor. This type of compressor is discussed at length. Nevertheless, to be complete, the wet type is discussed as well.

7.1.1 History

Compared to other types of compressors, the history and technology of screw compressors is relatively young. The idea of a twin rotor machine with helical lobes had been first conceived by Krigar in 1878. However, this machine had no internal compression. So in fact it was an advanced form of blower.

In the 1930s a Swedish engineer, Alf Lysholm, tried to design a compressor that was rotary in action, could operate at higher speeds than piston compressors so it could be driven directly by a turbine, and that could not surge. His objective was to combine this new compressor with a gas turbine he was investigating to develop a gas turbine engine. He invented the twin-screw compressor, which had in principle the features he desired. However, the screw compressor needed to be of too large a size to handle the large volumes of air the gas turbine demanded. In the end this ruled out the screw compressor in gas turbine engines. Nevertheless, the development of the screw compressor idea for industrial applications was continued by the Swedish research organization Svenska Rotor Maskiner, usually identified by its initials SRM. The first license in the world for the commercial exploitation of the screw compressor principle was taken out by the British company James Howden of Glasgow in the year 1946. Since then licenses have been taken out by many other companies in Europe, America, Japan and Russia.

The first type developed was the oil-free or dry design. This was followed by the oil-injected air compressor first marketed in 1957. In 1961, the first oil-injected refrigeration and gas unit was brought to market. Progressive research and development has enabled the screw compressor to establish a position in the market where it is pre-eminent. Lately, the screw compressor applications and sizes have expanded into areas where previously other types of compressor were unchallenged. However, the research has in basis all been experimental. The application of CFD could notably further the development.

7.1.2 Principle of operation

As for any positive-displacement compressor, the operation can be split into three phases : suction, (internal) compression and expulsion.

Figure 7.1 shows a pair of meshing rotors. The left rotor is generally designated the male rotor and the right female rotor. The male rotor turns anti-clockwise. The working chamber is comprised between the rotors and the casing. For clarity, the casing is not depicted in the following figures.

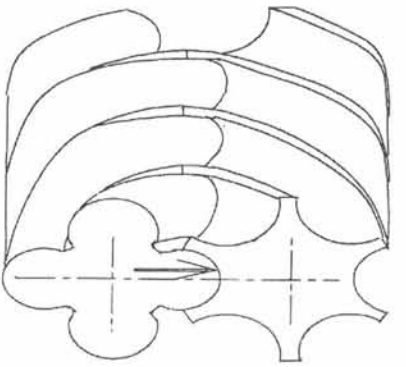

Figure 7.1: A typical pair of meshing screws

In figure 7.1, the pair of lobes considered is marked with an arrow. From this figure it is also clear that as the rotors turn, each pair of lobes start their cycle almost without intermittence after the previous pair. As for a tooth compressor, the inlet flow rate is continuous, yet not constant.

Figure 7.2 shows the meshing rotors after 90 degrees male rotation. When in the case of screw compressors rotation is mentioned, rotation of the male rotor is meant. From now on the term rotation will be used without reference to the male rotor.

Because of the rotation a space has been formed between the rotors. This spaced is hatched in figure 7.2. It is open to the inlet port and gas is drawn into the working chamber.

As the rotors rotate, the hatched spaced becomes larger (cf figures 7.3 and figure 7.4). The volume of the working chamber increases. During the suction phase the working chamber remains open to the inlet port and gas is drawn in. Figure 7.4 shows the position of the rotors and the working chamber at

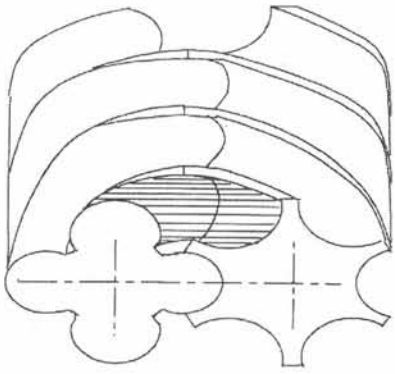

Figure 7.2: The rotors from figure 7.1 after 90 degrees rotation

the end of the suction phase.

As the rotors rotate further, the lobes start to re-mesh. From the point when the rotors remesh, the working chamber is isolated from the inlet port. The gas in the working chamber is trapped between the rotors and the casing. Figure 7.5 shows the evolution of the working chamber (hatched) as the rotors keep rotating. For clarity in these plots the rotors are viewed from the bottom, instead of from the top.

In figure 7.5, it is clear that as the rotors re-mesh, the volume of the working chamber is reduced. If this is allowed to continue until the end face profile is fully in mesh without providing an outlet for the trapped gas, there will be no volume left for the gas to occupy. As all rotating positive-displacement machines, screw compressors have no clearance volume.

The shape of the outlet section determines at which angle of rotation of the re-meshing rotors the gas is discharged into the outlet port. Thus the shape of the outlet section determines how much the working chamber is reduced in volume. The internal volume ratio of a screw compressor is geometrically determined. In figure 7.6, a typical axial and radial outlet section is depicted. Note that the inlet port and the outlet port are never in direct contact. There is no need for valves to guide the compression cycle.

Because of the internal compression, the outlet flow rate is not continuous. This was also the case for the tooth compressor. However, as the screw compressor depicted in figures 7.2, 7.3, 7.4 and 7.5 has 4 compression cycles per revolution and the tooth compressor only one or two, the outlet flow rate is less pulsed.

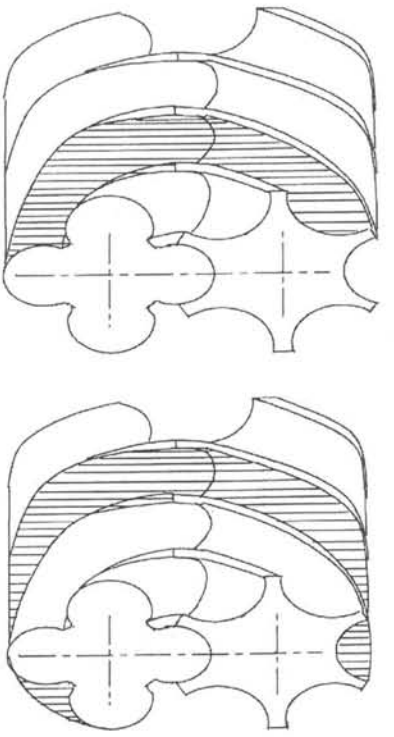

Figure 7.3: The rotors from figure 7.1 during the suction stage

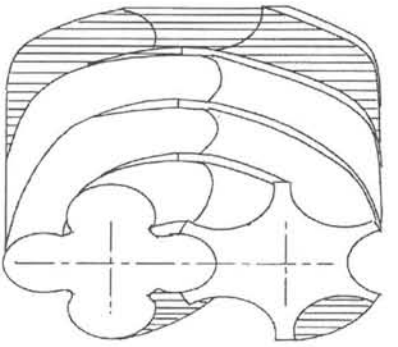

Figure 7.4: The rotors from figure 7.1 at the end of the suction stage

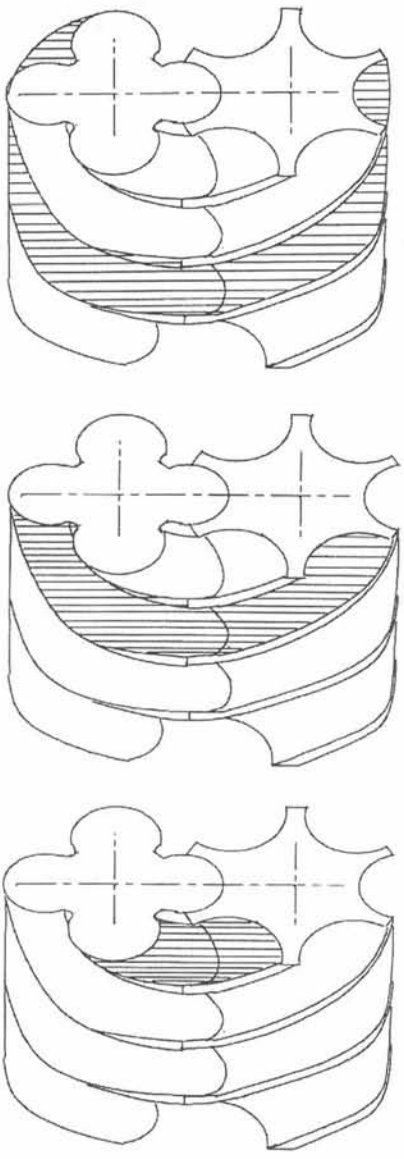

Figure 7.5: The rotors from figure 7.1 during the compression stage

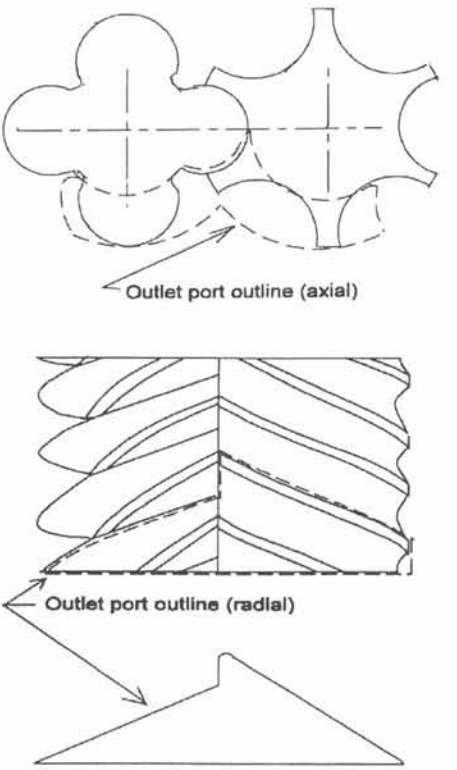

Figure 7.6: Outline of a typical radial and axial outlet section

In general, the shape of the outlet and the inlet port is fixed. This defines a fixed built-in internal volume ratio. The internal pressure ratio is directly linked with the volume ratio by the polytropic relation :

$$pV^{\kappa} = C^{onstant} \tag{7.1}$$

The value κ in (7.1) is dependant on the gas that is compressed and can vary. Thus the internal pressure ratio is also determined by the compressed gas.

If the pressure ratio between outlet and inlet is different from the internal pressure ratio, overcompression or undercompression occurs (chapter 1). These phenomena represent a loss in efficiency. A typical efficiency graph versus pressure ratio is shown in figure 7.7.

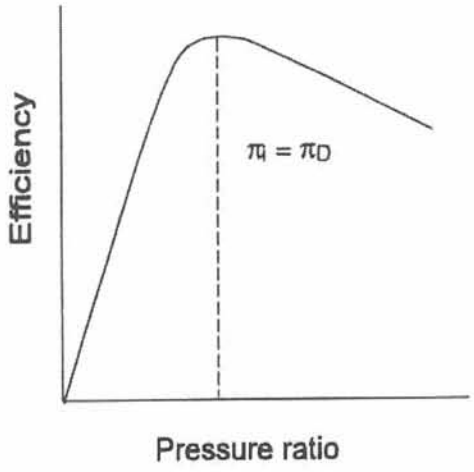

Figure 7.7: A typical efficiency versus pressure ratio graph; the dashed line indicates the working point where internal and external pressure ratio are equal

7.1.3 Geometry

The number of lobes that may be selected for each rotor is in theory unlimited. There are a number of factors involved in the selection, some of which are conflicting. The final choice is often a compromise.

Consider the rotor profiles in figure 7.8 as an illustration.

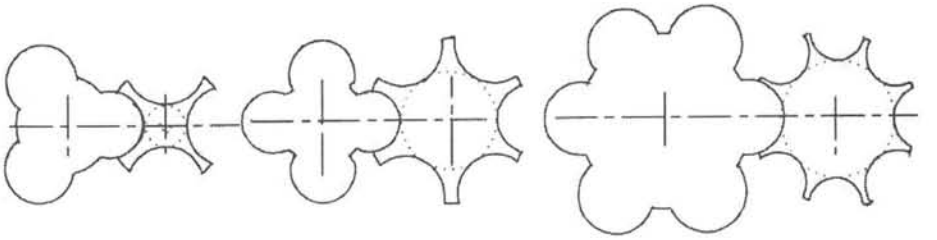

Figure 7.8: Different rotor profile combinations; fltr : 3+4, 4+6, 6+8

The 3+4 combination clearly has the largest swept volume. As there are only 7 rotor tips, the sealing line is relatively short. The sealing line is the length along which the rotors seal the gas between high and low pressure areas. A short sealing line therefore means a reduced leakage flow and a higher efficiency. Clearly, the 3+4 combination has the largest swept volume to sealing length ratio and will have the highest efficiency. On the other hand, consider the load that is exercised by the pressurized gas on the rotors. Figure 7.9 is an illustration of the pressure pattern and the resulting force on the rotors. This force leads to a bending moment on the rotors. In the 3+4 combination, the core radius of the female rotor is small. The bending moment on the female rotor will deform the rotors most in the 3+4 combination, thus limiting the allowable pressure raise.

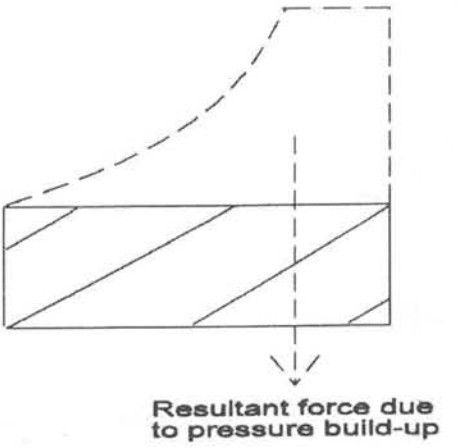

Figure 7.9: Illustration of pressure load along the screws

The 6+8 combination depicted on the far right in figure 7.8 has the largest core diameters for both the male and female rotors. The allowed pressure rise

in the compressor is high for this combination. However, the radius of swept volume to sealing length is relatively low. The efficiency of this combination is too low.

At present, most screw compressors are designed with a 4+6, 4+5 or 5+6 combination of lobes, as this is considered to be the best trade-off. A 4+6 combination is shown in the middle of figure 7.8. The 4+6 combination is favoured, because it is usually designed with both rotors having the same diameter. The achievable compressor efficiency of a 5+6 combination may be 0.5-1% higher, but this is not a real advantage as this falls within manufacturing tolerances.

The geometry used for the validation calculation is a 4+6 combination.

The ratio of the rotor length to the rotor diameter is another factor in the compressor design. In theory, a compressor of any length can be designed. As the swept volume of the rotors is directly proportional to the rotor length, one desires to build screw compressors as long as possible. The limit on the rotor length is the pressure load. As the rotor length increases, the resultant pressure force is more eccentric and the bending moment on the rotor increases. At the same time, the distance between the supporting points of the rotors gets larger, which in fact weakens the resistance to bending. Typical L/D values for full duty compressors are in the range 1.0-1.7.

The geometry used for the validation calculation has an L/D value of 1.69 based on the male rotor and 1.47 based on the female rotor.

Another factor in screw compressor design is the wrap angle. The wrap angle is the difference in rotation angle between the front and the end profile of the male rotor. It is the factor that determines at which rotation angle the working chamber stops expanding and starts reducing in volume.

Figure 7.10 shows the change of volume of the working chamber as the rotors unmesh and remesh, neglecting the influence of the wrapping angle (so for a theoretical infinite wrap angle). The volume changes for exactly 180 degrees, besides which it remains constant.

If the wrapping is exactly 360 degrees, the evolution of the working chamber volume consists of these two plots following back-to-back. If the wrapping angle is more than 360 degrees, the volume of the working chamber will remain unchanged for a part of the rotation. During this period, the rotors just churn in free air while the gas in the working chamber heats up. The efficiency of

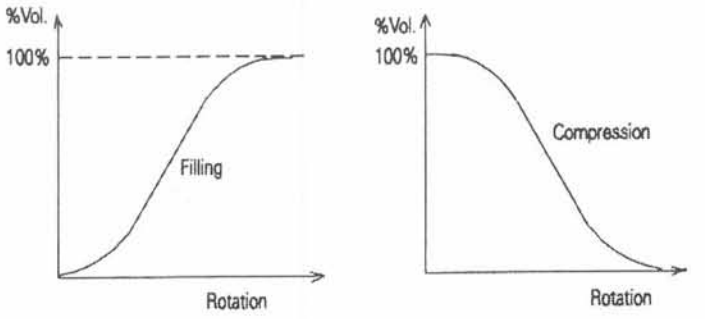

Figure 7.10: Change of volume during unmeshing and remeshing

the machine drops.

If the wrapping angle is less than 360 degrees, the working chamber is not at its theoretical maximum volume as it stops expanding and starts shrinking. The machine does not use its maximum volumetric capacity.

A trade-off of these two effects results in common values in the range of 250-350 degrees wrapping angle. In figure 7.11, a volume cycle with 300 degrees wrapping angle is shown. The small overlap in filling and compression theoretically causes some of the gas to be reversed, which is shown as the true theoretical swept volume curve.

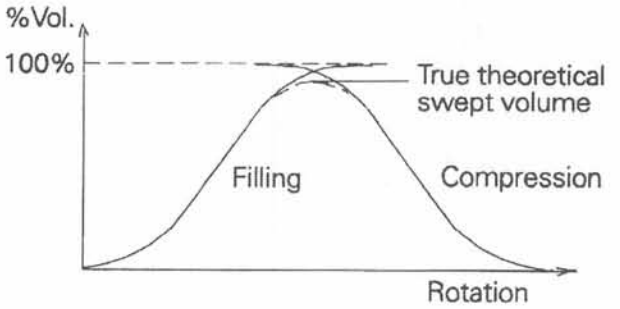

Figure 7.11: Volume versus rotation for a wrap angle of 300 degrees

The geometry used for the validation calculation has a wrapping angle of 350 degrees.

The final factor in screw compressor design is the rotor profile. The screw compressor is a machine that relies on small sealing clearances between rotors

and between rotors and casing. The shape of these clearances is determined by the rotor profile.

In a screw compressor, there are five types of leakage flows. The leakage through the air seals between a rotor shaft and the atmosphere will not be discussed. It suffices to mention that this is a minor leakage, which mainly impacts on the volumetric efficiency. The other four types of leakage flow are through the clearance between the rotor tips and the housing, through the clearance between the meshing rotors, through the clearance at the end planes of the compressor and through a particular gap, named the blowhole.

As the rotors have to rotate in a stationary housing, there has to be a clearance between the rotor tips and the housing. Through this clearance, gas flows from one chamber to another at lower pressure and temperature. This leakage flow impacts on the compression efficiency.

A second leakage flow is through the clearance between the meshing rotors. Between the meshing rotors, a fictitious three-dimensional line can be drawn where the clearance between both rotors is minimal. It is at this line that gas will leak from the compression chambers. The gas leaks from the compression chambers straight to the inlet at atmospheric pressure. This leakage mainly impacts on the volumetric efficiency. However, as the leaked gas is at a higher than atmospheric pressure and temperature, there is also an effect on the compression efficiency.

A third leakage occurs at the end planes. The rotors rotate in a stationary housing, so a clearance is necessary at the end planes. Through this clearance gas will leak from one chamber to another and to the inlet. This leak occurs both at the inlet side and at the outlet side. The leak at the inlet side is not very important, since there is no pressure build-up. This leak has a small effect on the volumetric efficiency. The leak at the outlet side is more important, as here the chambers are at or near the end of their compression cycle. The leakage flow has effect on both the volumetric and the compression efficiency.

Finally, there is also leakage through the blowhole of the screw compressor. The blowhole is a triangular gap between the rotor tips and the housing. It is shown in figure 7.12. Because of manufacturing reasons, it is impossible to have a sealing line between the rotors that reaches to the cusp of the housing. The consequence of this is the blowhole. Through this blowhole gas can flow relatively easily from one compression chamber to the previous. The blowhole exists throughout the entire axis of the compressor, but is most important

at the outlet side. It has presumably the largest impact on the compression efficiency of the compressor of all leakage flows.

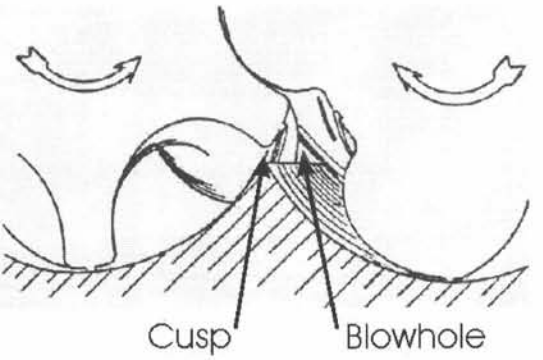

Figure 7.12: Illustration of the blowhole

The rotor profile has a large influence on the size and geometry of the blowhole. It also determines the length and shape of the sealing line between the rotors, and the actual geometry of the gap between rotors and casing.

Because of the large influence of the rotor profile on screw compressor efficiency, its exact shape is a secret closely guarded by the manufacturing companies. On sight, a distinction can be made between symmetrical and unsymmetrical profiles. Symmetrical profiles are mainly applied to oil-free compressors.

The geometry used for the validation calculation is oil-free and therefore has a symmetrical rotor profile.

7.2 Oil-free or dry screw compressors

Over the years screw compressors have developed into two distinct categories, depending on whether oil is injected into the compressing gas or not. Both operate on exactly the same principle described above, but differ in this one major feature. This difference does not only change the pressure-temperature relationship within the compressors, but also has a large impact on the compressor design. Each type of screw compressor has particular characteristics, which suit it to different types of duty and certain markets. The oil-free version is mainly aimed at delivering oil-free pressurized air starting from atmospheric conditions. The oil-injected version delivers pressurized air already

mixed with oil for pneumatic machinery. It also has an important application in refrigeration technology. In general, there is very little direct competition between both types.

7.2.1 General

For the dry screw compressor design, it is paramount that there is absolutely no contact between the compressing gas (mostly air) and oil, from whatever source. This puts a distinct stress on the implementation of the various seals and bearings in the compressor. These features of the compressor design are much more complex than for the oil-injected type.

As there is no oil to lubricate the contact zone of the two meshing rotors, special attention must be paid that both rotors never touch. If they do, the high temperatures and speeds will ensure serious damaging. To prevent both rotors from making contact, both shafts are driven via a rigorous (external) timing gear. Luckily, the rotor profiles are always such that most power is absorbed by the male rotor and almost no power by the female rotor. This prevents much power to be transferred through the timing gear, allowing it to be relatively small.

A more important consequence of the dry design is that the internal compression is virtually uncooled. The short residence time of the gas in the machine makes external cooling impossible. By consequence, the internal compression is accompanied by a large temperature rise. To avoid large deformations of the compressor casing, the casing is usually cooled. Nevertheless, the discharge temperature has to be limited, which in turn limits the pressure ratio. A typical maximum discharge temperature with casing cooling is 525 K, Without cooling, the discharge temperature has to be limited even further to about 475 K. In some heavy-duty designs, the rotors are also cooled to avoid deformation, yet this is rare.

7.2.2 Application ranges

7.2.2a Speed range :

As mentioned above, there are four leakage paths in a screw compressor along which gas leaks from high to low pressure. They are the clearances between

the meshing rotors, across the rotor tips, across the rotor end faces and the blowhole. These clearances do not change with the speed of the rotors. The leakage flow rate is, in theory, only determined by the pressure gradients in the machine and is constant versus varying rotor speed. In practice, a small influence of the rotor speed is observed, which can be safely neglected. On the other hand, the gas flow rate through the compressor is of course directly proportional with the rotor speed. This leads to a volume-speed characteristic as displayed in figure 7.13. Notice the negative flow rate at zero rotor speed. From this graph, it is clear why screw compressors are not operated at low speed. The efficiency would be too low. In the case of oil-free screw compressors, this also means that the discharge temperature would be too high.

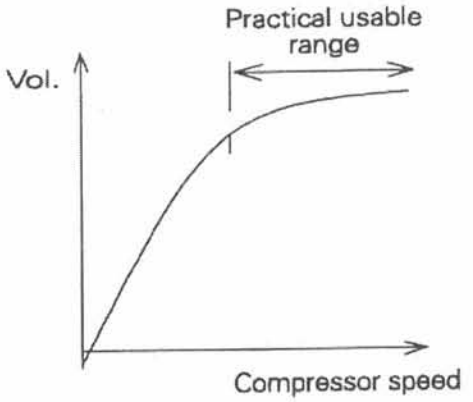

Figure 7.13: Typical volume-speed characteristic

Screw compressors also have a maximum operating speed. The centrifugal load on the lobes of the rotors imposes stress related maximum speeds. However, these values are never reached. Before reaching the stress related maximum speed, the losses associated with the higher flow rate through the inlet and outlet sections overcome the gain in volumetric efficiency that is obtained with higher speeds. After all, although the flow rate through the compressor is directly proportional with the rotor speed, the area of the inlet and outlet sections is unchanged. The higher flow rate through these sections generates higher losses. Very soon, what is gained in volumetric efficiency is dissipated by these losses. The overall result on the basis of adiabatic compression efficiency is shown in figure 7.14. The resulting range of (male) rotor tips speeds is typically 50-100 m/s.

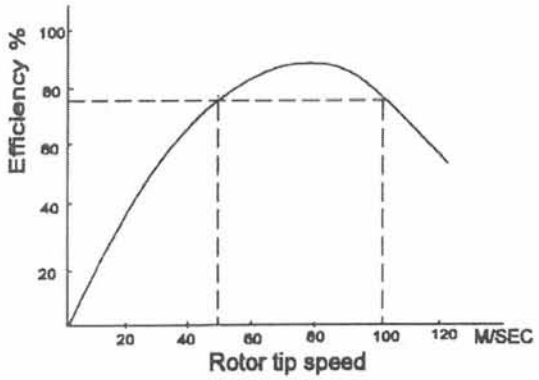

Figure 7.14: Typical adiabatic efficiency-speed characteristic for an oil-free screw compressor

For the geometry used for the validation calculation, this results in a rotational speed operating range of 7900-15800 rpm.

7.2.2b Pressure range :

The pressure load in a screw compressor will result in a radial force (as the pressurized gas is mainly situated on one side of the machine (cf. on the bottom in figures 7.2 to 7.5)), in an axial force (as the pressure is high on the outlet side of the machine) and in a bending moment (because of the eccentrical radial force). From these three, the deflection caused by the bending moment is the most critical. In oil-free screw compressors, however, the pressure ratio is in general not limited by these considerations, but by the maximum discharge temperature that has to be observed. Only when gas at high pressure is supplied at the inlet, or if the ratio L/D is excessively large, the discharge pressure is limited by the bending moment. Typically the maximum pressure ratio obtainable is of order 4.5/1. The maximum discharge pressure is in the range 10-20 bar. This puts the oil-free screw compressor in the medium range of compressors.

The geometry used in the validation calculations has an internal pressure ratio of just below 3/1.

7.2.2c Size range :

Oil-free screw compressors are produced by some ten companies in the world. Manufactured rotors range in diameter from around 100 mm to 800 mm. In volume terms these compressors compress volumes in the range 300 up to 80000 m^3/h. This puts the oil-free screw compressor in the medium range.

7.2.3 Efficiencies

The volumetric efficiency of an oil-free screw compressor versus rotational speed at constant pressure ratio was shown in figure 7.13. The graph is characterized by the fact that the leakage flow is constant for a constant pressure ratio. Figure 7.15 shows the volumetric efficiency versus pressure ratio.

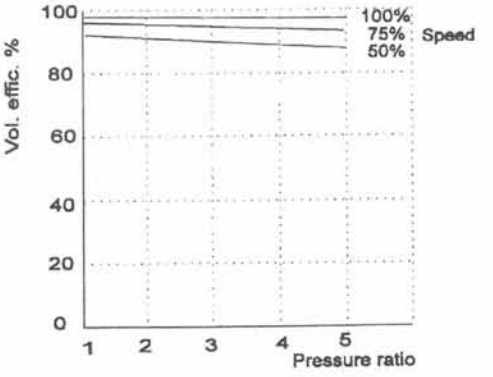

Figure 7.15: Typical volumetric efficiency-pressure ratio characteristic for an oil-free screw compressor

The variation in efficiency is small. Besides the pressure ratio and the speed, the volumetric efficiency is also influenced by the rotor size. As the production tolerance is relatively smaller for large machines, they achieve higher volumetric efficiencies. The adiabatic efficiency of an oil-free screw compressor versus rotor speed was shown in figure 7.14. At low speeds, the low volumetric efficiency also lowers the adiabatic efficiency. At high speeds, the various friction losses associated with higher fluid velocities overcome the gain in volumetric efficiency and the curve drops off. Figure 7.16 plots the compression efficiency versus pressure ratio. A maximum is observed for a pressure ratio equaling the internal pressure ratio. The curve drops off to the left and the right because of overcompression and undercompression losses.

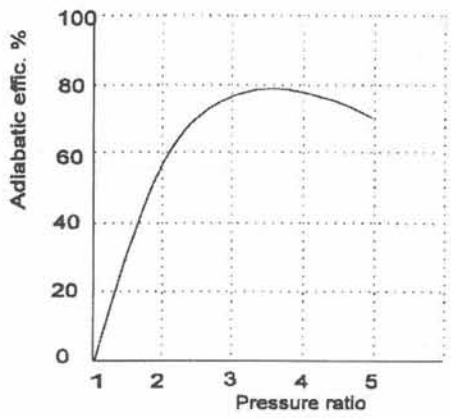

Figure 7.16: Typical adiabatic efficiency-pressure ratio characteristic for an oil-free screw compressor

A typical adiabatic efficiency for a large oil-free screw compressor is 80 % and slightly above. Smaller machines may have adiabatic efficiencies of at least 10 % less.

7.3 Oil-injected or wet screw compressors

The screw compressor considered in the validation calculation is of the dry type. Nevertheless, the wet type is also discussed to be complete.

The screw compressor has no clearance volume and therefore it is tolerant to liquid carry-over. This means that it is possible to inject a liquid in the compressing gas without negative consequences (as long as the amount injected is not such that the compressor is called upon to compress the liquid). It proves to be especially beneficial to inject the gas with oil. The addition of oil increases the pressure and pressure ratio capabilities, simplifies the compressor design, provides virtually total temperature control and reduces compressor speeds and noise levels.

7.3.1 Injected oil functions

7.3.1a Cooling :

This is the most important function. As the oil remains in liquid form, it has a large specific heat capacity and it is capable of absorbing a large portion of the heat generated during the compression of the gas. This cooling has a large positive effect on the efficiency of the compression. Besides that, it allows virtually total control of the discharge temperature. The obtainable pressure ratio is larger than for a dry screw compressor. And as the discharge temperature is controlled to a relatively low level, there is no need for a cooling jacket around the casing.

7.3.1b Sealing :

Most of the leakage paths discussed in the previous section are long thin clearances. The injected oil is very effective in sealing these. The only leakage that is not substantially lowered, is through the blowhole. This increases the volumetric and overall efficiency for the same duty, or permits larger pressure differences across the rotors.

7.3.1c Lubrication :

In the oil free screw compressor, the rotors had to be kept out of contact with each other. However, in the wet type there is plenty of oil present to lubricate the contact zone. Furthermore, as the female rotor absorbs only a small fraction of the compressor power, it is feasible to eliminate the timing gear and have the male rotor drive the female. If the same oil is used to lubricate the bearings, the shaft sealing is much less complicated. This in turn allows the rotor support bearings to be brought in much closer to the rotor body, improving the rotor stiffness and reducing deflection.

7.3.1d Silencing :

The rotation of rotor lobes past the inlet and outlet section and the meshing of the rotors generate a high noise level. However, this noise is mainly acoustic

(not structure-born) and the presence of the viscous oil is surprisingly effective in damping the noise.

7.3.2 Rotor profile

As mentioned above, the rotor profile has a large influence on the shape and size of several leakage paths, and the blowhole in specific.

In figure 7.17, the position and size of the blowhole is illustrated for a symmetric and an unsymmetric profile.

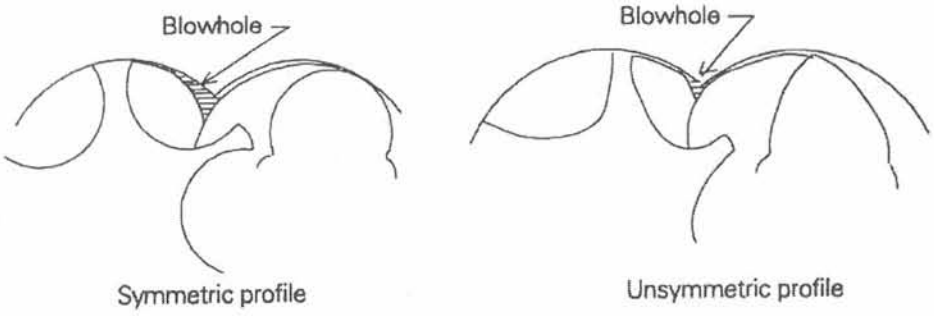

Figure 7.17: Effect of the rotor profile on the blowhole size; left : symmetric; right : unsymmetric profile

The fundamental difference between symmetric and unsymmetric profile rotors is that for the unsymmetric lobes the blowhole area is reduced to about one-tenth of the blowhole area with symmetric lobes. One way of describing this effect is to consider that the lobes of the unsymmetric profile 'lean' into the blowhole. Remember that the blowhole is the only leakage path that is not long and thin in shape, but an open hole, therefore being the only gap the injected oil has difficulty sealing. It is clear that the change to unsymmetric profiles implies a significant improvement in compressor performance in oil-injected screw compressors. In general, symmetric profiles are not used.

Figure 7.18 shows a sketch of an unsymmetric profile. It can be seen that on one side of the centerline, the lobe is much steeper.

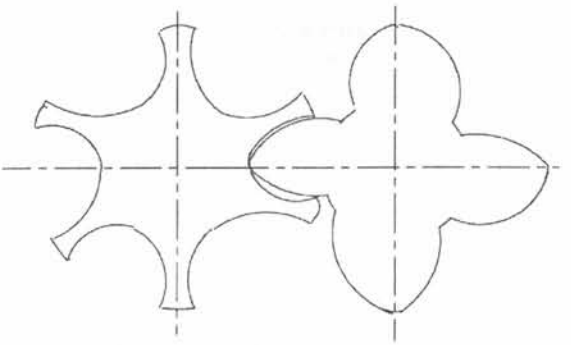

Figure 7.18: Sketch of an unsymmetric rotor profile

7.3.3 Ranges of application

7.3.3a Speed range :

For oil-free screw compressors, it was discussed that the leakage flow rate was constant versus the rotor speed, while the flow rate through the compressor was directly proportional with the rotor speed. The minimum operating speed was determined demanding that the back-flow was sufficiently low relative to the total flow rate. The same logic applies to oil-injected compressors. The only difference is that the oil effectively seals all but one leakage path (the blowhole), thus reducing the back-flow. Therefore the minimum operating speed can be much lower. A typical present-day value is a (male) rotor tip speed of 10 m/s (vs 50 m/s for the dry type).

The maximum operating speed for oil-free compressors was reached when the additional losses associated with the higher fluid velocity canceled out any gain in volumetric efficiency. This is the same for oil-injected compressors, but the presence of the viscous oil adds extra losses. A lot of energy gets dissipated as the oil is churned around by the rotors. A typical maximum (male) rotor tip speed lies between 50-60 m/s (vs 100 m/s for the dry type).

This leads to a compressed volume of 60-3000 m^3/h for air compressors. For refrigeration applications, larger compressors are manufactured that can displace up to 12000 m^3/h.

7.3.3b Temperature range :

The cooling capacity of the injected oil allows virtually total temperature control. However, there are some factors that impose practical limits. Most of the oil injected in the gas has to be separated from the gas after it leaves the compressor. This separated oil is cooled externally and re-fed to the compressor. If the discharge temperature is high, the oil cooler can be small. Less oil has to be injected and the viscous losses the oil introduces in the compression are lower. On the other hand, high temperatures mean larger expansion of the casing and the rotor. One does not want to re-introduce casing cooling ! Another limit, more technical of nature, is imposed by the degradation of the oil quality at high temperature. The allowed discharge temperature is a compromise between these factors. A typical value ranges from 375-400 K. The amount of injected oil needed to absorb the excess heat is 0.5-1.0 %vol.

7.3.3c Pressure range :

In oil-free screw compressors, the discharge temperature limited the possible pressure ratio. Because of the cooling capacity of the injected oil, this limit expires and the pressure range of wet screw compressors is determined by the pressure load. It was discussed above that the support bearings are closer to the rotor body, adding to the rigidity of the rotors. This means that the pressure load can be higher than for the dry type.

A typical maximum value for the internal pressure ratio is 8/1 to 9/1. The pressure ratio between outlet and inlet can be up to 13/1. Higher pressure ratios involve multi-staging for efficiency reasons. The maximum discharge pressure depends on the application. For oil-injected air compressors it ranges from 7 to 14 bar. Compressors used in refrigeration have maximum discharge pressures of up to 25 bar as the suction pressure is already high. Although these values are much higher than for the dry type, it is still considered to be medium compressor range.

7.3.4 Efficiencies

The graph of volumetric efficiency versus rotor speed is completely similar to the one for oil-free screw compressors. The only difference is that the range of applicable speeds starts at lower speeds, as the leakage is lower.

For the compression efficiency, a distinction has to be made between compressors for air duty and for refrigeration duty. A typical graph of adiabatic efficiency and volumetric efficiency versus pressure ratio is plotted in figure 7.19. It is very similar to the one for dry compressors (figures 7.15 and 7.16), except that the optimum working point is situated at a higher pressure ratio.

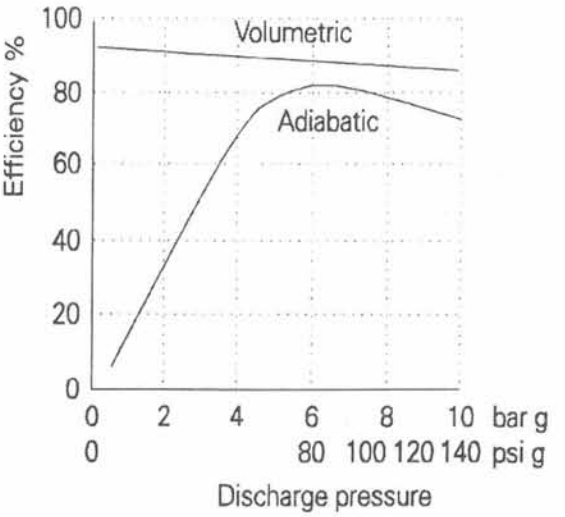

Figure 7.19: Typical adiabatic efficiency-pressure ratio characteristic for an oil-injected air compressor

Note that the compression efficiency is expressed as an adiabatic efficiency, always lower than one. The presence of cooling might lead one to expect that isothermal compression is possible. In reality, the compression heat is not externally removed, but remains present in the oil-air mixture. The oil is subsequently separated from the air and cooled. Although this procedure improves the compression efficiency, it does not to such an extent that isothermal efficiency is within reach.

The pressure ratios achieved in compressors used in refrigeration are much higher than for air duty. Figure 7.20 shows typical plots of the volumetric and adiabatic efficiencies for high and for extreme pressure ratios. They look similar to the previous ones, but especially at very high pressure ratios it is notable that the volumetric efficiency is not nearly constant, but actually follows a curve that falls away.

Furthermore, the suction pressure in these machines is usually not atmospheric. As the density is a function of the pressure, a different inlet pressure

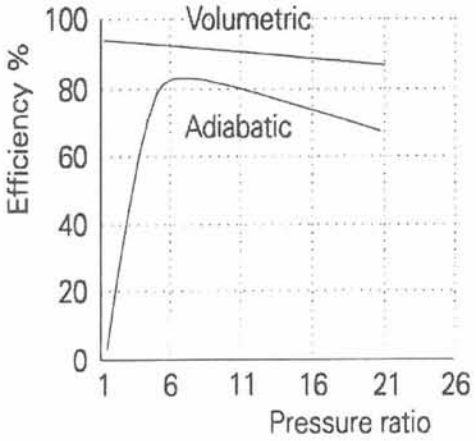

Figure 7.20: Typical adiabatic and volumetric efficiency versus pressure ratio characteristics for an oil-injected refrigeration screw compressor

results in different efficiencies. Figure 7.21 shows a typical graph of volumetric and adiabatic efficiency versus pressure ratio for different suction pressures.

7.4 Calculation : set-up

The validation calculations are performed on an oil-free screw compressor. This type of compressor was chosen, because the screw compressor is the most complex rotary-positive displacement machine from a CFD viewpoint. The dry type was chosen because the clearances in this type are smaller than in the wet type. This makes the grid generation more challenging. Another reason is that the compression is single-phase, thus eliminating the need for a multi-phase model in the CFD calculation.

The geometry used for the validation calculations is shown in figure 7.22. It consists of a casing, cooled by a water jacket, and an inlet and an outlet port. The depth of the casing is 204.35 mm. The rotor diameters are 139.1 mm (male) and 120.9 mm (female). The wrap angle is 350 degrees (female). The built-in internal pressure ratio is slightly lower than three for air. The rotational speed simulated ranges from 4000 rpm to 17000 rpm (male rotor). The suction pressure is atmospheric (1 bar abs, 293 K). As there is no lubrication between the meshing rotors, the compressor is fitted with a timing gear to avoid rotor contact.

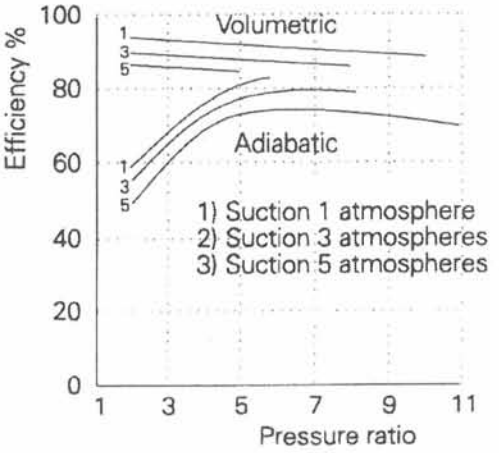

Figure 7.21: The effect of varying suction pressure on the efficiencies of an oil-injected screw compressor

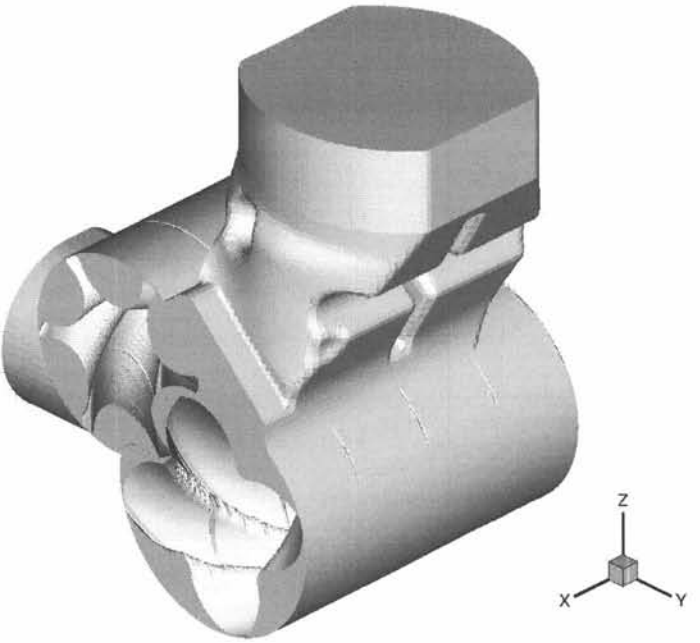

Figure 7.22: The screw compressor geometry used for validation calculations

7.4.1 The grid

The geometry naturally decomposes into three blocks, namely the inlet port, the outlet port and the casing. The grid reflects this natural decomposition. The grid is block-structured with four blocks, namely the inlet port, the outlet port and two blocks in the casing, each associated with one rotor.

The grid blocks in the inlet and the outlet port are stationary. They are not handled by the grid manipulation algorithm and are meshed using a powerful gridding algorithm available in the commercial package ProAm. Near the inlet and the outlet section, the grid is hexagonal to better suit the imposed boundary condition. The rest of the grid is a mix of hexagons and pyramids. The grid in the inlet and the outlet port is depicted in figure 7.23. The number of cells is 106511 in the inlet block and 74692 in the outlet block.

The grid in the casing is structured and hexagonal. It is build by stacking two-dimensional structured rectangular grids in slices of the casing. The procedure for the grid generation and manipulation is the same as described for the tooth compressor calculation (chapter 6).

There is however one extra complication. The rotors are helical or twisted in the axial direction. This does not interfere with the grid generation or manipulation as described in chapter 6, but it does put an extra stress on the three-dimensional grid. Because of the twist, the hexagonal cells are skewed. By this is meant, that in the axial direction, the faces of the cells are defined by four nodes that are no co-planar (cf figure 7.24). If the skewing is too large, the numerical accuracy of the solver is impaired. Luckily, the cells in the clearances between the rotors and the casing are but slightly skewed. The main problem area is situated in the cavity of the rotor profiles (the working chamber). The only effective means to control the skewness of the cells is altering the axial grid spacing in that a finer grid axially has less skewed cells.

As described in chapter 6, the use of a structured hexagonal grid allows the grid manipulation algorithm to reduce the problem of moving the grid nodes to the problem of generating a two-dimensional grid in a casing slice for every degree rotation of the rotor profiles. These 2D grids are constructed by the grid generator described in chapters 4-5.

The nodes on the division line, which divides the casing in two blocks, are distributed according to the curvature of the division line, but with an under-relaxation factor of 0.3. This means that the distribution is a mix of mainly

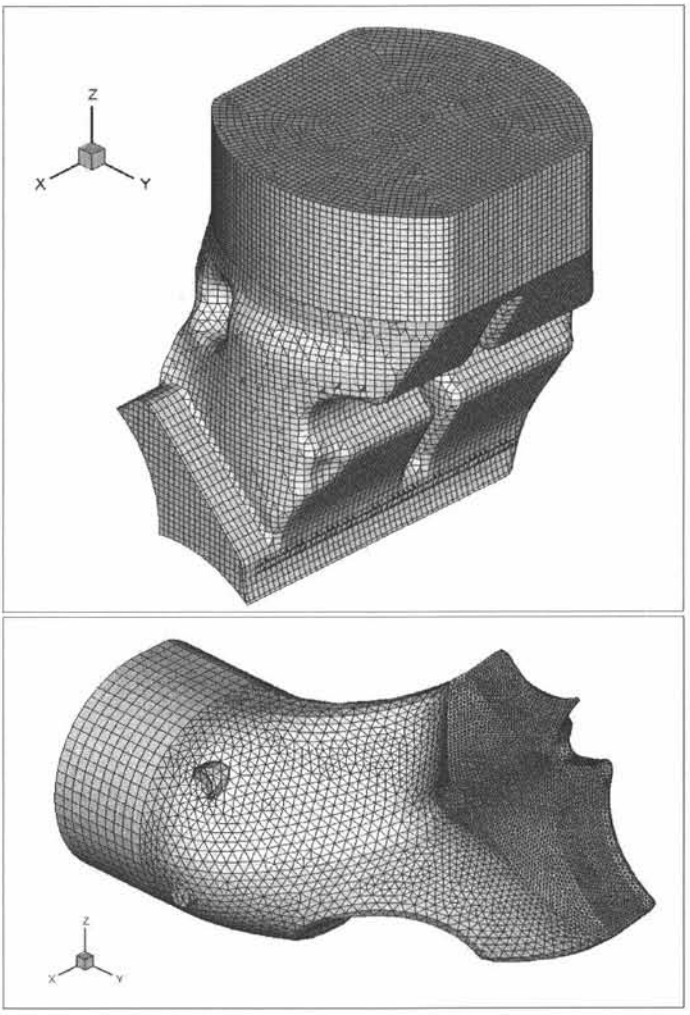

Figure 7.23: The 3D grid in the inlet and the outlet port

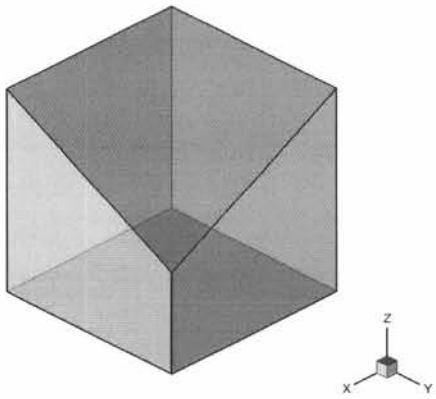

Figure 7.24: A skewed hexagonal cell; the four top nodes are not coplanar

equidistant (70%) and purely according to curvature (30%). The influence of the division line curvature is strongly attenuated. The reason for this is two-fold.

For the screw profile, the rotor tips do not protrude into the adjacent domain as much as is the case for the tooth compressor (cf figure 7.25). Because of this, the division line is less strongly curved and the curvature is not as good a criterion to locate the rotor tips. On the other hand, there is not as much need to draw the nodes towards the rotor tips. As the division line is relatively straight, even an equidistant distribution would result in a grid resolution that resolves the geometry of the rotors almost sufficiently.

More importantly, the nodes distributed according to curvature would move along the division line quite violently as the profile rotates. Bearing in mind that because of the twist in the rotors, the three-dimensional grid is build by stacking 2D grids with different rotation of the profiles, this would cause the grid cells in the meshing zone of the rotors to be severely skewed. To avoid problems associated with this skewing, it is imperative that the movement of the nodes on the division line is strongly damped by a low underrelaxation factor.

The nodes on the casing slide along the casing to achieve a locally higher grid resolution near the rotor tips. This is necessary on the one hand to keep the aspect ratio of the grid cells under control and on the other hand to ensure that the grid resolves the rotor tips accurately. Because of the large

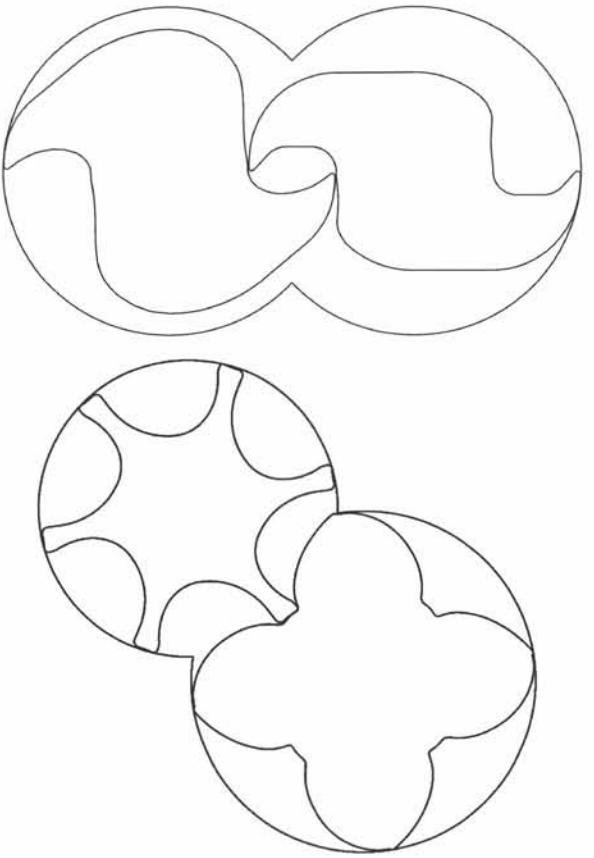

Figure 7.25: A 2D slice of the tooth compressor casing (top) and the screw compressor casing (bottom)

importance of lowering the leakage through all clearances, the clearances are extremely small and the rotor tips are fitted with tip seals. The size of the clearances is of order 30 micron, while the rotor diameter is about 3000 times that size. Figure 7.26 shows that by sliding the nodes on the casing, it is possible to obtain a grid that is fine enough in the gaps, yet has no cells with excessive aspect ratios.

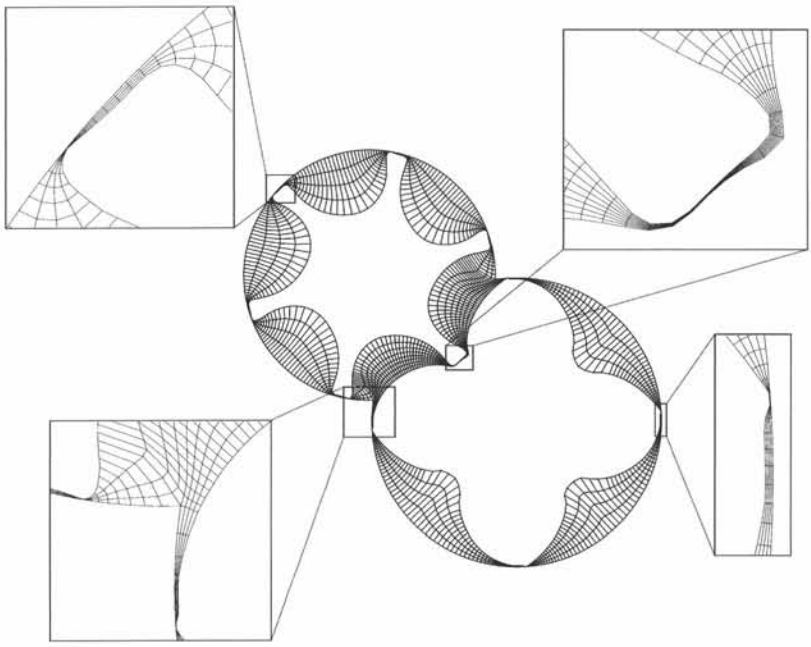

Figure 7.26: 2D grid in a slice of the screw compressor casing

The local smoothing described in chapter 5 is applied as well. In the rotor cavities, tangential smoothing is not needed for geometric reasons, as the cavity is not as concave as was the case for the tooth compressor rotors. However, the tangential smoothing helps reduce the skewness of the three-dimensional grid in these zones.

Each block of the grid is made up of 5 nodes radially and 240 nodes tangentially. Similarly as discussed in chapter 6, the leakage flow through the gap between rotors and casing is a mix of a pressure-driven Poisseuille flow and a Couette flow, in which the Poiseulle flow is predominant. The velocity profile will be parabolic and five radial nodes are sufficient in the gap. The same can be claimed for the gap between the meshing rotors, except that here there are 9 nodes radially, which is certainly enough.

Of the 240 tangential nodes, 80 are placed on the division line between

both blocks. As illustrated by figure 7.26, this is enough to resolve the zone where the rotors mesh.

The quality of the grid is illustrated by figures 7.28, 7.29 and 7.30. These figures show typical grid quality parameters. The rotor rotation is ten degrees (cf figure 7.27).

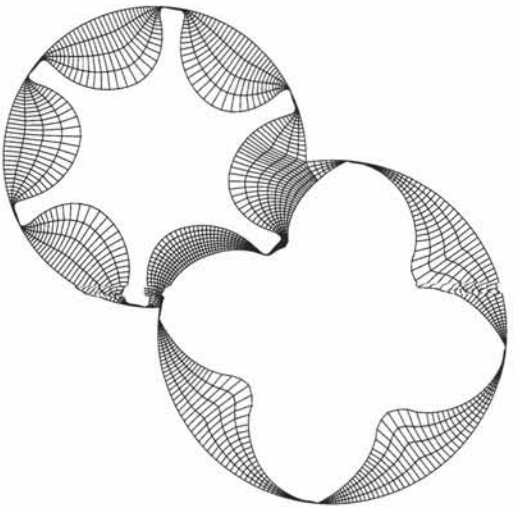

Figure 7.27: 2D grid in a slice of the screw compressor casing; rotation 10 degrees

Figure 7.28 shows the aspect ratio of the cells. The maximum aspect ratio is of order 100 and is located in the gaps between rotors and casing. In these zones, the grid is strongly aligned and a high aspect ratio is allowed. In the rest of the domain, the aspect ratio falls well within limits.

Figure 7.29 shows the volume (area) of the cells. The grid resolution changes smoothly throughout the domain. A higher grid resolution is obtained in the gaps between rotors and casing and between the meshing rotors. The exact position of the blowhole is not indicated on the figure, yet it is situated near the cusps. The grid resolution in these zones is sufficient to resolve the leakage flow. The coarsest grid is situated in the cavities of the profile.

Figure 7.30 shows contours of grid node movement. This is the displacement of the nodes if the rotor profile is rotated one degree. The largest node displacement is noticed in the cavities of the profile. This is why in the three-dimensional grid, the grid cells with the largest skewness are situated in this

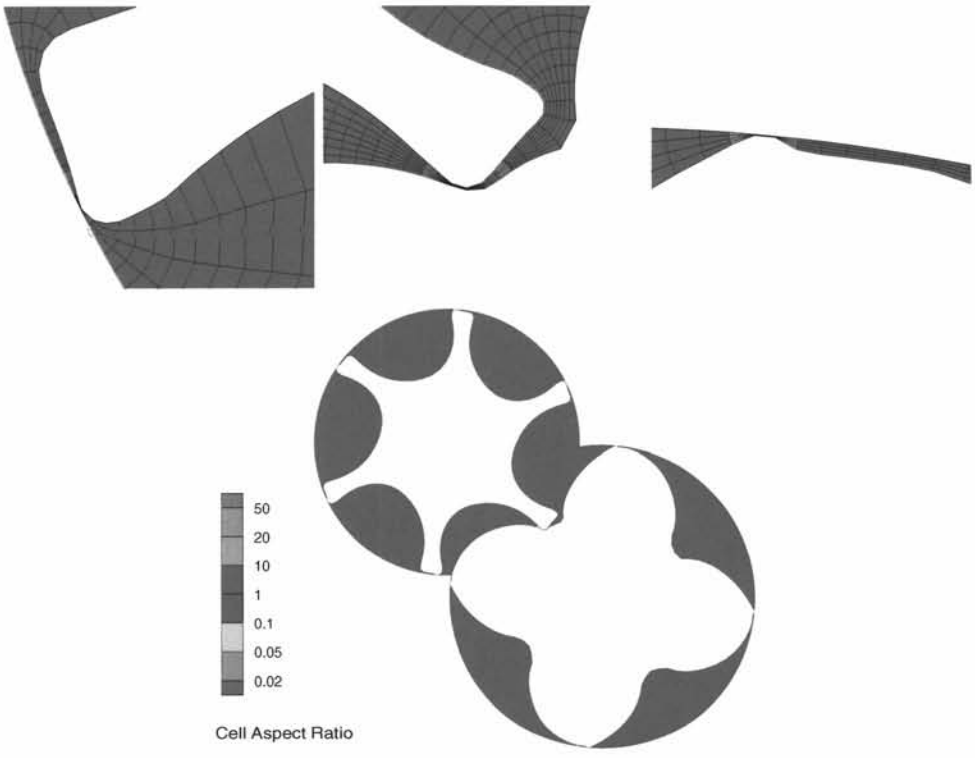

Figure 7.28: 2D grid in a slice of the screw compressor casing; aspect ratios; rotation 10 degrees

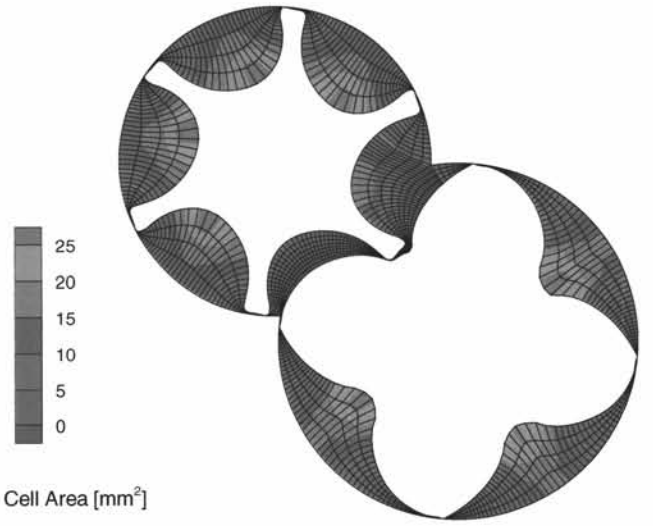

Figure 7.29: 2D grid in a slice of the screw compressor casing; cell volume; rotation 10 degrees

area. One can also notice that the grid displacement in the zone of the meshing nodes is acceptable because on the division line the node distribution is mixed with an equidistant distribution. With a distribution purely according to division line curvature, this displacement is much larger and would cause (too) skewed cells in the three-dimensional grid.

From the node displacement, the maximum node velocity can be derived. For a rotational speed of 17000 rpm (male), the maximum node velocity is 270 m/s. For this speed, the maximum rotor tip velocity is 106 m/s. The maximum expected fluid velocity in the gaps is of order 200-300 m/s. The maximum node velocity falls within this range and will not introduce eigenvalues of a different magnitude in the flow equation matrix. The stiffness of the flow matrix is not affected by the grid movement.

Based on the considerations above, the generated two-dimensional grids are suited for the calculations. A set of 60 root grids, each one degree rotation (female) apart is generated. Based on these grids, the three-dimensional grid is constructed and manipulated.

The root grids were generated on a Compaq DS20 machine using one processor per grid. The generation time breaks down as follows. The generation

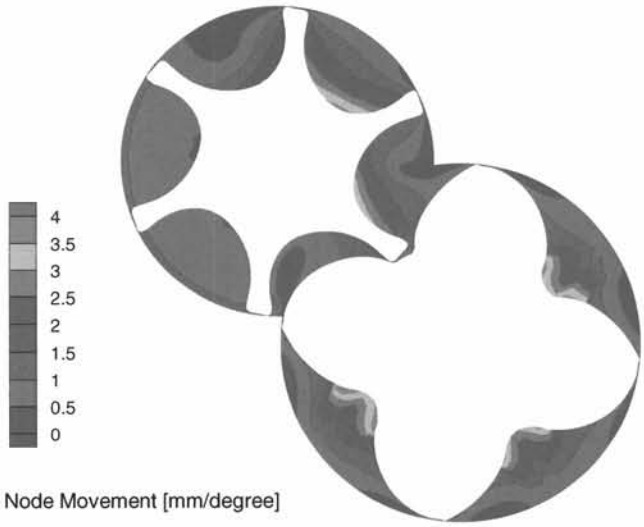

Figure 7.30: 2D grid in a slice of the screw compressor casing; grid node movement; rotation 10 degrees

of the triangular grid on which the potential solution is solved takes around 400 seconds. A typical grid has 40907 nodes. The solution of the potential equation, including iteratively determining the potential boundary conditions, takes around 450 seconds. The generation of the structured rectangular grid takes about 50 seconds. This makes a generation time of about 900 seconds per grid, or 15 hours for the entire set. Of course, the grid generation can be parallellized, thus significantly reducing the generation time. By comparison, one time step of the flow solver takes approximately 66 seconds on three linux boxes with a dual-processor of 2.4 GHz (so 6 processors).

Based on the set of root grids, the three-dimensional structured hexagonal grid in the casing is constructed. This is done by stacking 500 2D grids equidistantly in the axial direction. With this spacing, the aspect ratio is between one and 5 in the axial direction, and the skewness of the cells is acceptable. The grid in the casing thus consists of 2x4x240x499 = 958080 cells. The four blocks of grids are joined together using arbitrary sliding interfaces between the inlet and outlet port and the casing. The resulting three-dimensional grid has 1074963 cells. It is depicted in figures 7.31 and 7.32.

Figure 7.31: 3D grid in the screw compressor casing

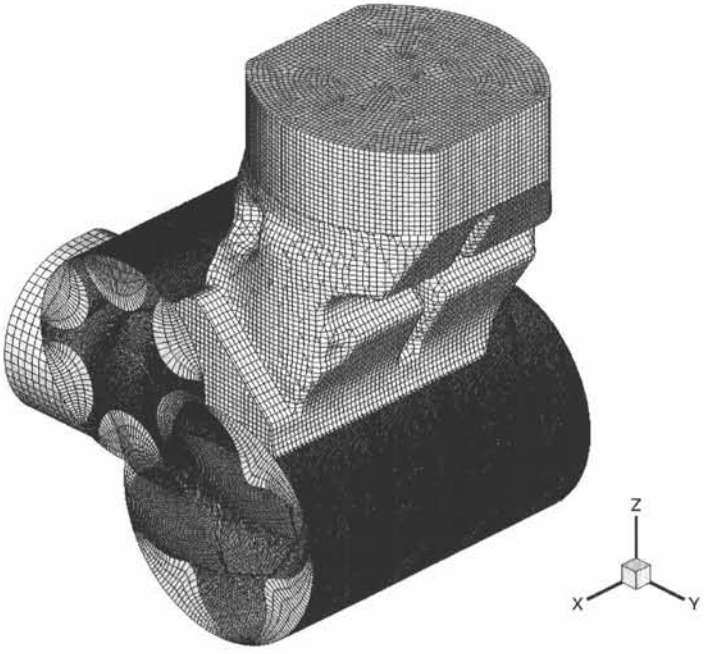

Figure 7.32: 3D grid in the screw compressor geometry

7.4.2 The solver

The flow calculations are performed by a commercial package that has been extended with a user-defined function to handle the grid movement.

The package used is Computational Dynamics' StarCD version 3.20. StarCD is a co-located cell-centered finite-volume code. It is developed for structured hexagonal grids and is capable of ALE calculations. The spatial discretization scheme that is used for the calculations is the Monotone Advection and Reconstruction Scheme (MARS). This is a monoticity-preserving TVD limiter scheme developed for the StarCD code. The temporal discretization is fully implicit. The set of algebraic equations obtained through these discretization schemes is solved using a modified PISO predictor-corrector scheme.

For the calculation, some simplifications have been made to the case.

The clearances at the end planes of the screw compressor are neglected. Especially at the compression end, gas leaks back to the inlet. This leakage is not comprised in the simulation and it is to be expected that the calculated efficiencies are slightly larger than the experimental.

Certain thermal effects are also neglected. The deformation of rotors and casing due to heating is not incorporated. This deformation mainly affects the size of the clearances between rotors and between rotors and casing. In first instance, an educated guess is made that the clearance between rotors and casing is 30 micron. The sensitivity of the results to the clearance is tested by further calculations with gaps of 10 micron and 50 micron. Furthermore, all walls are considered adiabatic. In reality, the casing is cooled by a water jacket. However, this cooling is aimed at minimizing the deformation of the casing due to heating. Because of the very short residence time of the gas in the machine (5 ms for 17000 rpm (male)), the external cooling of the compressing gas can be safely ignored. The assumption of adiabatic walls is valid.

As a final approximation, no turbulence model is used in the flow equations.

In the working chambers, in the outlet port, and to a lesser extent in the inlet port, the fluid flow is mainly driven by pressure gradients resulting from the change of volume in the working chamber and the expulsion and suction of gas. The influence of turbulence on such a flow is not very large. It is justifiable to ignore it.

In the gaps between the rotors and the rotors and the casing, the flow is actually laminar, because of the very small clearance. An expected velocity for the leakage flow is about 300 m/s. With a clearance of order 10 micron, this leads to a Reynolds number of order 1000.

This does not hold for the leakage flow through the blowhole, as the blowhole is much larger. However, the blowhole is short in the axial direction and a turbulent boundary layer cannot build up. Therefore, the error of considering this flow to be laminar is probably small.

As the compression is oil-free, the fluid is single-phase. As compressed gas, air is used, defined as an ideal gas. At the inlet and the outlet, pressure boundaries are imposed. The suction is atmospheric and at the inlet a pressure of 1 bar abs is imposed. The temperature of the entering gas is 293 K. At the outlet, pressures of 3 bar, 4 bar and 5 bar abs are imposed. The temperature of the re-entering gas is estimated to be 415 K, 455 K and 488 K respectively. These values are educated guesses based on the expected efficiency of the compression.

7.5 Calculation : results

During the simulation run, the mass flow rate and the power consumption of the compressor are monitored. These values will be compared to experimentally obtained values.

It is not possible to experimentally measure any characteristics other than global ones. Because the geometry is very closed-up, it is impossible to obtain flow field data inside the machine. In particular, velocity data in the gaps would be interesting, but is far beyond reach. The only local data that could be measured is the evolution of pressure in certain points on the casing. Even temperature measurements in these same points are not feasible as the temperature sensors are too slow in response for the high speeds at which the compressor operates. This is exactly why CFD could prove to be very useful.

To validate the calculations, the volumetric efficiency and the specific work are compared with experimental values. Temperature efficiencies are calculated to check whether the values are realistic. Inlet and outlet mass flow are compared to check whether the calculation is conservative. In a time-converged cycle, the amounts of air taken in and expelled must be equal.

7.5.1 Reference calculations

The first case is defined by clearances between the rotors and the casing that are 30 microns wide. This value is an educated guess for the clearances at operating conditions. As the exact value cannot be measured, an educated guess is the best that can be achieved.

The rotational speeds simulated are 4000 rpm, 10500 rpm and 17000 rpm (male rotor). It was discussed in a previous section that the application range of an oil-free screw compressor in terms of rotor tip speed is 50-100 m/s. For this geometry, this means rotational speeds between 8000 rpm and 16000 rpm. The simulation at 4000 rpm is way out of application range and the efficiencies should be miserable. The simulation at 17000 rpm is at the high edge of the application range.

The pressure ratio between inlet and outlet is one bar to 3 bar, 4 bar and 5 bar (absolute). It was discussed that a typical maximum achievable pressure ratio is of order one to 4.5-5. This puts the case with 5 bars outlet pressure again at the very edge of the application range. The discharge temperature calculated for this case is expected to be near the maximum allowable value. The built-in internal pressure ratio of the compressor is slightly lower than 3 for air. This means that in all three cases, undercompression will occur, albeit only light for 3 bar outlet pressure. This should be reflected in the plot of specific work.

Consider as illustration the simulation at 4000 rpm (male) and with a pressure ratio of 3 bars. In figure 7.33, the contours of pressure are plotted in a slice through the rotor axes. One can clearly distinguish the different working chambers formed by the rotor lobes.

In figure 7.34, the velocity profile in the gap between the rotors is depicted.

In figures 7.35, 7.36, 7.37, and 7.38, graphs of the mass flow rate and the averaged mass flow rate at inlet and outlet, the power consumption and averaged power consumption and the discharge temperature are plotted over the span of the complete simulation run. The mass flow rate and the power consumption are averaged over a period corresponding with one cycle (90 degrees male rotation). The three irregularities in the graphs correspond with the instances when the outlet pressure is raised from one bar to two bar, and then to three bar. Based on the graphs of the averaged mass flow rate and power consumption, it is concluded that the simulation has converged in

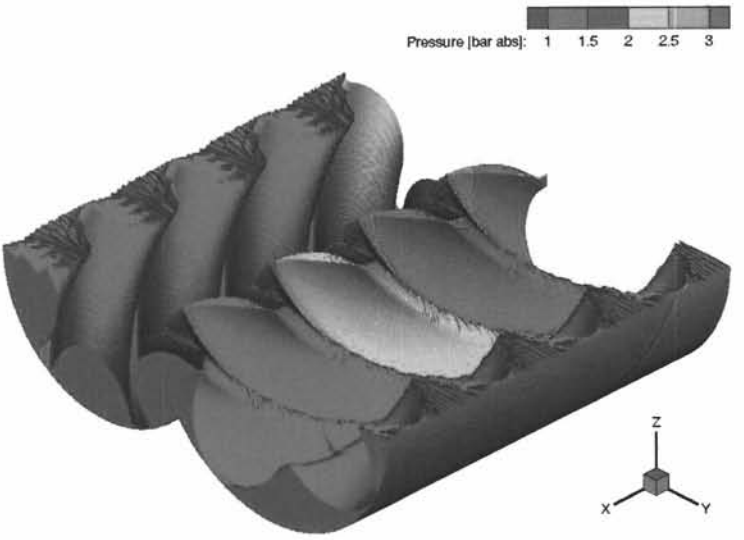

Figure 7.33: Contours of pressure in the screw compressor casing; 4000 rpm, 1-3 bar abs

Figure 7.34: Velocity profile in the gap between rotors; 4000 rpm, 1-3 bar abs

time to the steady-cycle state after approximately 17 compression cycles (or 1530 degrees male rotation). The averaged mass flow rate through the inlet is the same as through the outlet. This indicates mass conservation in the calculation. This is also true for the calculations at the other working points.

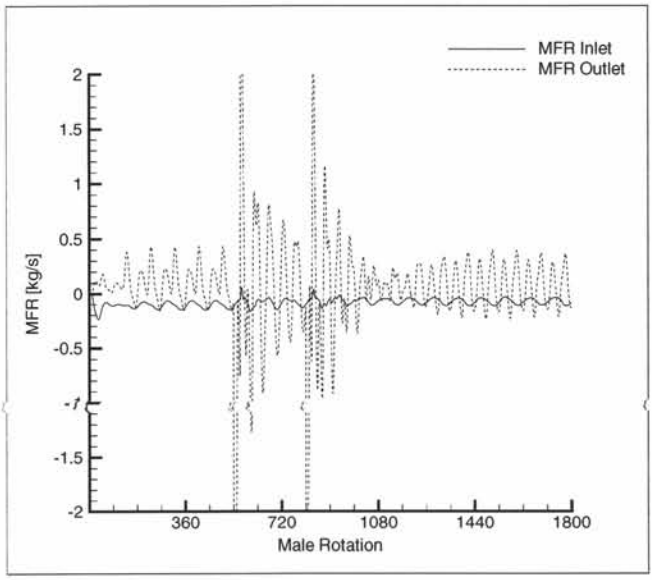

Figure 7.35: Evolution of mass flow rate at inlet and outlet

In figure 7.39, the mass flow rate at inlet and outlet over two cycles is plotted.

In the evolution of mass flow rate at the inlet, the non-linear change of the volume of the working chamber is easily recognized. In the mass flow rate at the outlet, a similar cycle can be found, but it is superposed with another cycle with the same frequency. The second peak is caused by a pressure wave induced by the undercompression in the machine. By comparison, in figure 7.40 one cycle of the mass flow rate at the outlet is plotted for an outlet pressure of one bar. This is the same as the inlet pressure and in this instance overcompression occurs. Again a second oscillation can be observed, this time caused by the overcompression. Notice that the effect of the overcompression is as notable as the undercompression, although the overcompression is much more severe than the undercompression (the internal pressure ratio is about 3). Even if the pressure ratio were exactly the same as the internal pressure ratio, the sudden contact between the outlet port and the working chamber would put the gas in the outlet port suddenly in motion, creating a pressure wave running down the outlet port. So even with an outlet pressure exactly

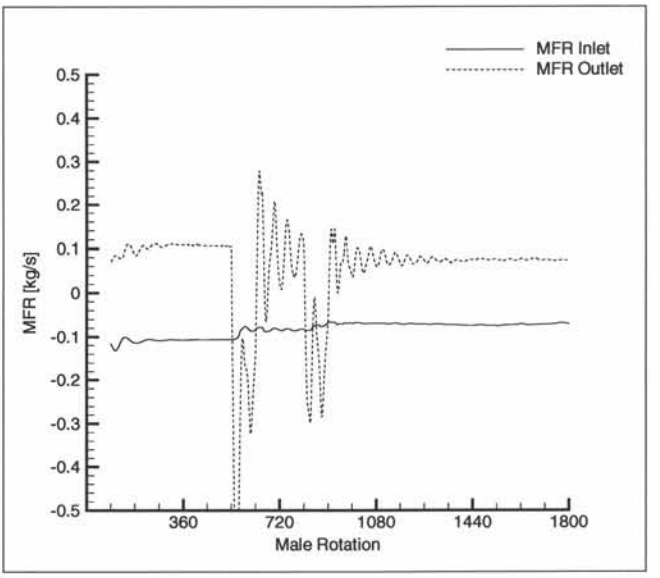

Figure 7.36: Evolution of averaged mass flow rate at inlet and outlet

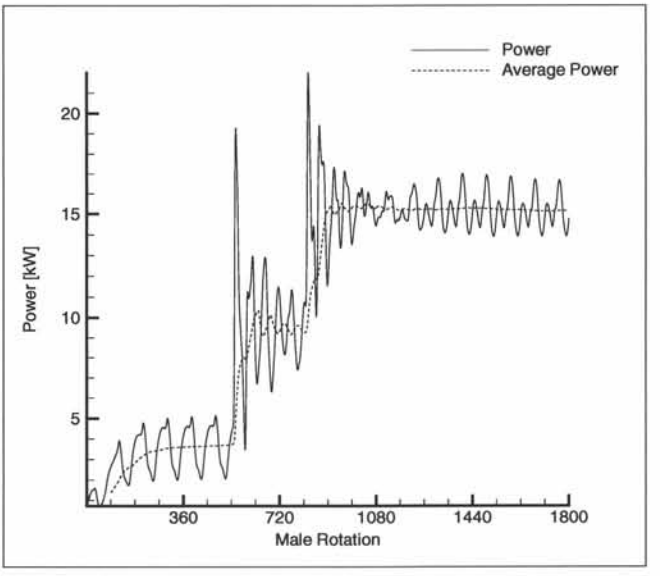

Figure 7.37: Evolution of power consumption

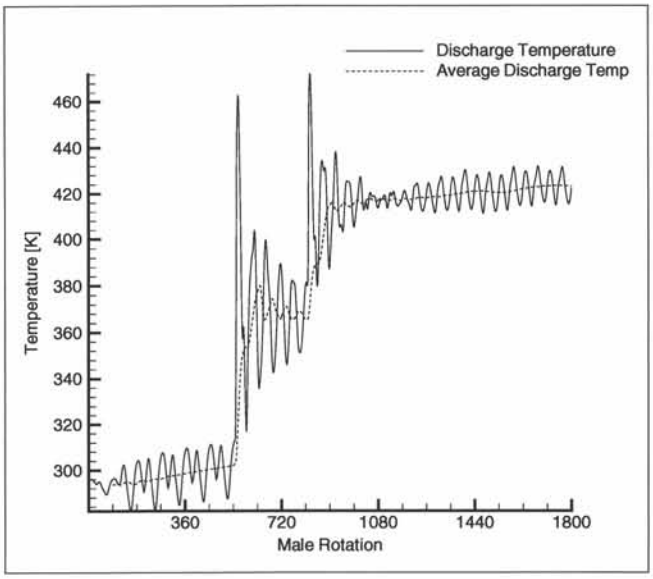

Figure 7.38: Evolution of temperature at outlet

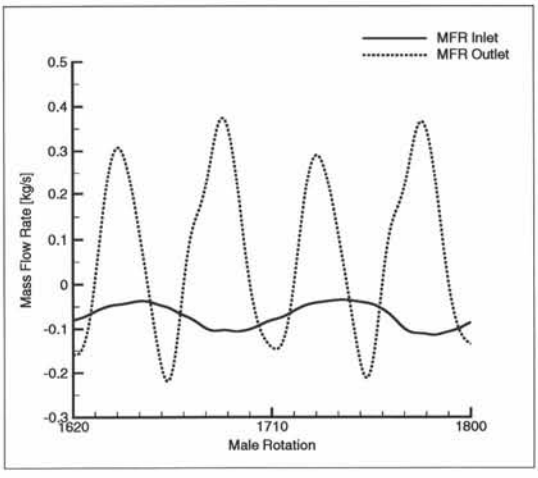

Figure 7.39: Evolution of mass flow rate at inlet and outlet during two compression cycles; 4000 rpm, 1-3 bar

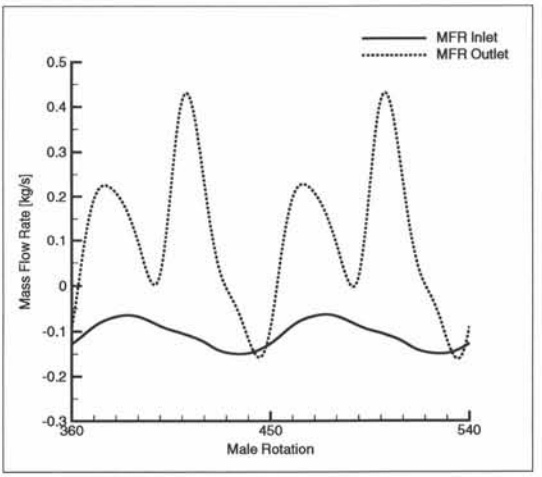

Figure 7.40: Evolution of mass flow rate at inlet and outlet during two compression cycles; 4000 rpm, 1-1 bar

matched to the internal volume ratio, the mass flow rate at the outlet could not be as smooth as at the inlet where the inflow is almost continuous.

What happens is that at the start of discharge, a pressure wave is formed, be it by gas entering or leaving the working chamber. This pressure wave is propagated with the speed of sound towards the outlet. But the gas is expelled into the outlet port at a much lower velocity. Therefore it may be interesting to evaluate the flow situation in the outlet section of the casing. This is the inlet section of the outlet port. It is hereafter named short 'outlet section'.

In figure 7.41, figure 7.42 and figure 7.43, the mass flow rate through the outlet section is plotted for an outlet pressure of 1 bar abs, 3 bar abs and 4 bar abs. The difference between overcompression and undercompression is clear on these plots, while it was a lot less clear on the previous plots due to the pressure waves. For an outlet pressure of 4 bar abs, the flow even reverses into the working chamber.

In figure 7.44 and figure 7.45, the mass flow rate through the outlet section is plotted for a rotational speed of 10500 rpm and 17000 rpm (male) and an outlet pressure of 3 bar abs. The mass flow rate through the outlet is plotted for these rotational speeds in figures 7.46 and 7.47. The profiles are different from the one for 4000 rpm (cf figures 7.42 and 7.39). This is because the cycle time has changed, but the speed of sound at which the pressure wave travels is the same. Thus the influence of the pressure wave on the flow in the outlet

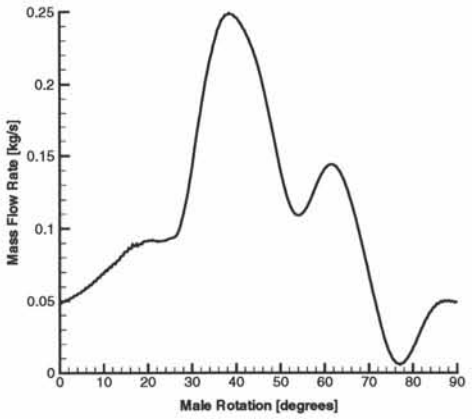

Figure 7.41: Evolution of mass flow rate through the outlet section during a compression cycle; 4000 rpm, 1-1 bar

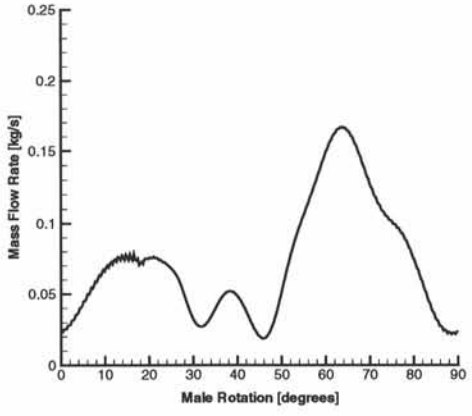

Figure 7.42: Evolution of mass flow rate through the outlet section during a compression cycle; 4000 rpm, 1-3 bar

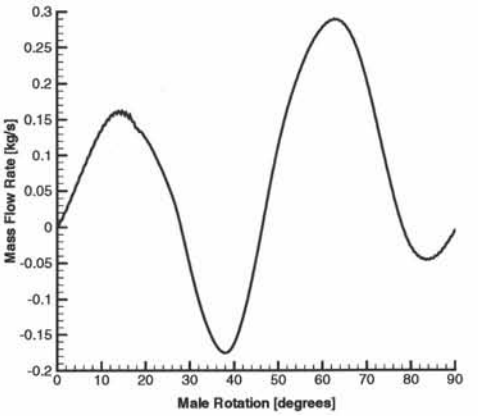

Figure 7.43: Evolution of mass flow rate through the outlet section during a compression cycle; 4000 rpm, 1-4 bar

port is different. This is the basis of the concept of tuning the outlet port for a specific optimal operating speed. By changing the shape of the outlet port, the pattern of the pressure waves is changed. This way one can design the outlet port such that the influence of the pressure waves is small or even positive. In figures 7.39, 7.46 and 7.47, it can be observed that the mass flow rate at the outlet is much smoother for a rotational speed of 10500 rpm or 17000 rpm. As 4000 rpm is really outside the application range it is not surprising that the outlet port is not tuned for such a low speed. The mass flow rate is highly irregular.

In figures 7.48 and 7.49 the mass flow rate through the outlet is plotted for pressures of 4 and 5 bar abs. It is clear that as the undercompression gets worse, the effect on the mass flow rate increases. The peak in the first half of the cycle grows.

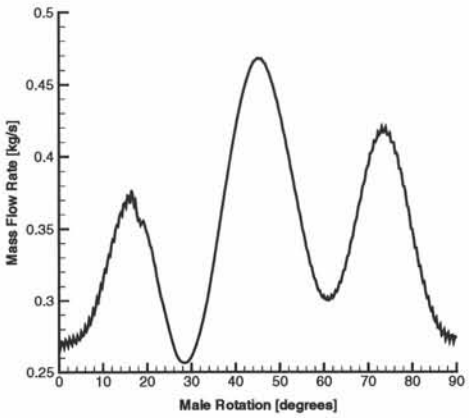

Figure 7.44: Evolution of mass flow rate through the outlet section during a compression cycle; 10500 rpm, 1-3 bar

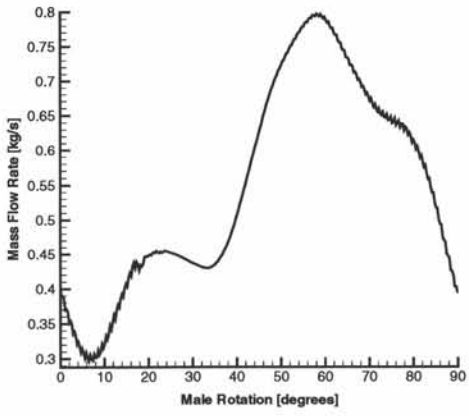

Figure 7.45: Evolution of mass flow rate through the outlet section during a compression cycle; 17000 rpm, 1-3 bar

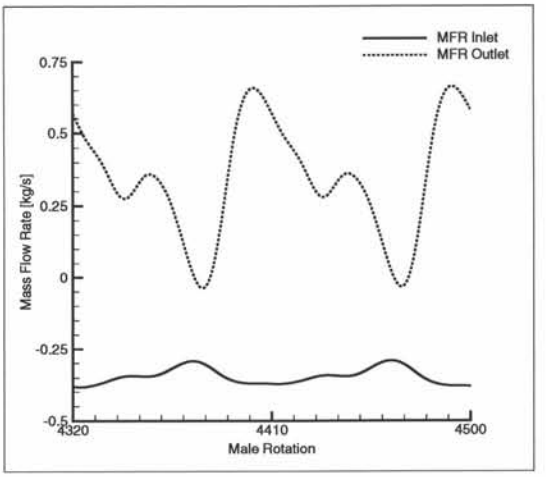

Figure 7.46: Evolution of mass flow rate at inlet and outlet during two compression cycles; 10500 rpm, 1-3 bar

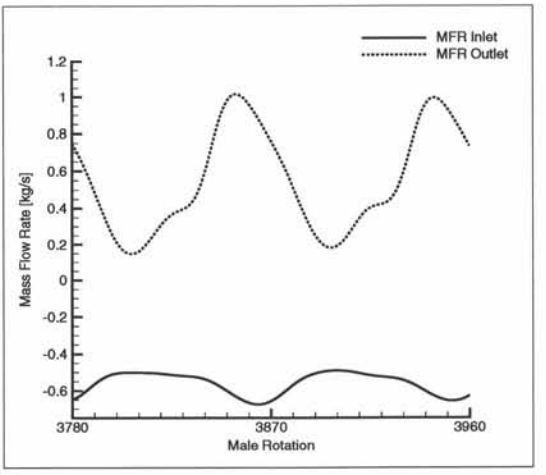

Figure 7.47: Evolution of mass flow rate at inlet and outlet during two compression cycles; 17000 rpm, 1-3 bar

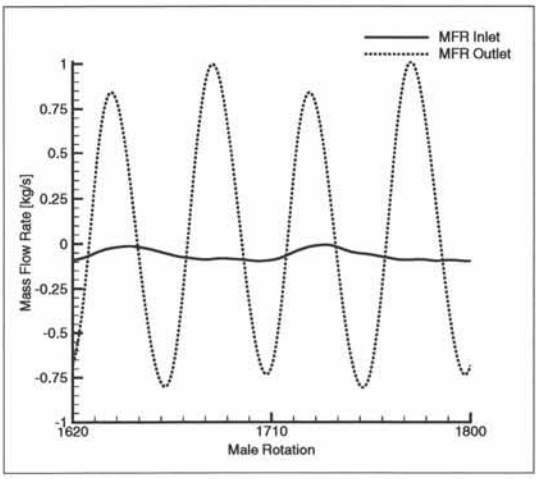

Figure 7.48: Evolution of mass flow rate at inlet and outlet during two compression cycles; 4000 rpm, 1-4 bar

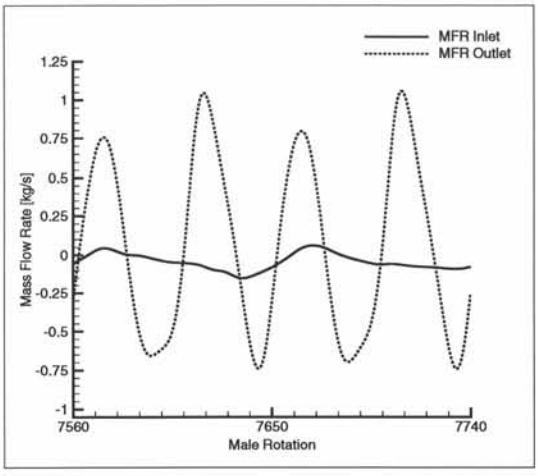

Figure 7.49: Evolution of mass flow rate at inlet and outlet during two compression cycles; 4000 rpm, 1-5 bar

In figure 7.50, the consumed power is plotted for 4000 rpm and an outlet pressure of 3 bar abs. In this plot, the power is broken up into the power consumed by the male rotor and by the female rotor. As was pointed out in previous sections, the female rotor consumes only a small fraction of the total power. This makes it possible to drive the female rotor by a timing gear of moderate size. Notice that the power consumed by the female rotor is positive throughout the cycle. This is a design aim as this ensures that any slack on the timing gear is consumed.

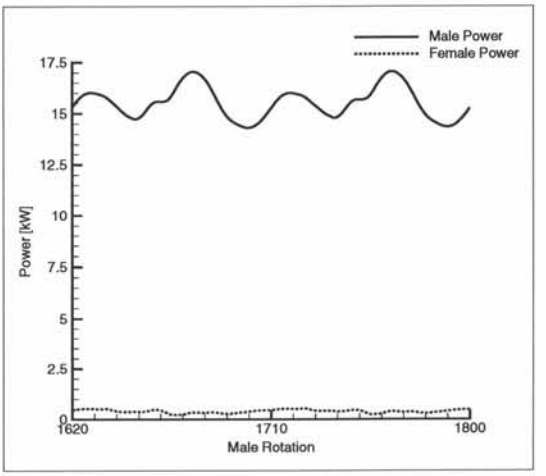

Figure 7.50: Power consumption during two compression cycles; 4000 rpm, 1-3 bar

It was also mentioned that the screw rotors are subject to an axial force due to their helical shape. This axial force is plotted in figure 7.51. It is always pointed towards one end of the compressor. This allows the end plane clearance to be accurately controlled by an axial bearing. Any axial slack is consumed by the axial force.

7.5.1a Efficiencies

Based on the averaged values of the time-converged mass flow rate, power consumption and temperature at the outlet, the efficiency of the screw compressor at the various working points can be evaluated. The volumetric efficiency is defined as the ratio of the averaged mass flow rate to the theoretical mass flow rate. The theoretical mass flow rate is defined as the maximum volume of the working chamber multiplied by the compression cycle rate and the density at the inlet. To assess the compression efficiency, the specific work to compress

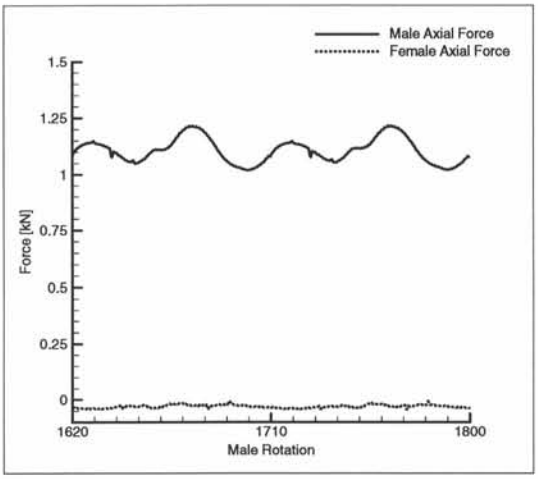

Figure 7.51: Evolution of axial force during two compression cycles; 4000 rpm, 1-3 bar

the air is calculated. It is defined as the averaged power divided by the mass flow rate. The specific work relates inversely to the compression efficiency. To assess the discharge temperature, the temperature efficiency is calculated. It is defined as the ratio of the temperature rise according to adiabatic compression to the actual temperature rise. A typical graph for oil-free screw compressors is depicted in figure 7.52.

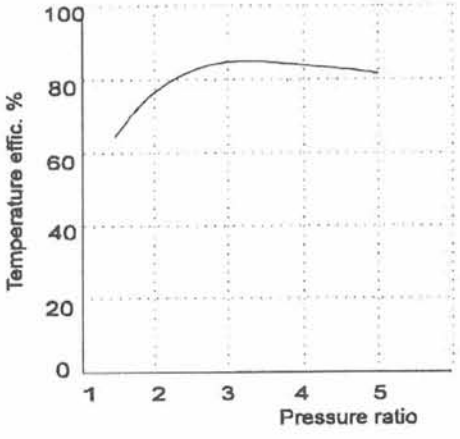

Figure 7.52: Typical plot of temperature efficiency versus pressure ratio

The volumetric efficiency calculated and measured in experiments is plotted in function of the rotational speed in figure 7.53 and in function of the

pressure ratio in figure 7.54.

The correspondence with experiments is good for 10500 rpm and 17000 rpm, but poor for 4000 rpm. Nevertheless, the important trends can be found in both the experiments and the calculations. The volumetric efficiency slowly lowers for higher pressure ratios. In function of rotational speed, it is high for the 10500 rpm and 17000 rpm and falls away rapidly for 4000 rpm. The calculated volumetric efficiency for 10500 rpm and 17000 rpm is slightly higher than the experimental one, indicating that the leakage flow is underestimated. A possible reason for this lies in neglecting the end plane clearance. For 4000 rpm, the leakage is grossly overpredicted. As mentioned earlier, this working point lies well below the operating range of the machine. Most probably, the educated guess of 30 microns for the size of the clearances between rotors and casing does not hold. At this very low speed, much less power is consumed by the compressor (only around one third of the power needed at 10500 rpm and around one fifth of the power at 17000 rpm). At the same time, the compressor efficiency is very bad, leading to high gas temperatures. The cooling jacket has a lot less heat to extract at a higher temperature difference and will do a much better job of cooling the casing. The rotors on the other hand are not cooled, but are exposed to higher temperatures. The rotors will expand, but the casing won't due to the cooling. The result is that the clearances are probably smaller than for the higher rotational speeds.

In figures 7.55 and 7.56, the specific work is plotted versus the rotational speed and the pressure ratio. Once again, the agreement with experiments is good for 10500 rpm and 17000 rpm, but way off for 4000 rpm. This is not surprising, as the overpredicted leakage flow for 4000 rpm has a severe negative effect on the compression efficiency, leading to an overprediction of the specific work.

The important trends are caught though. The specific work is slightly lower for 17000 rpm than for 10500 rpm, as the gain in volumetric efficiency still overcomes the growing losses associated with higher gas velocities. The specific work needed to compress at 4000 rpm is a lot larger than at the other rotational speeds due to the terrible volumetric efficiency. In function of the pressure ratio, a rise in specific work can be noted for any rotational speed. This is the effect of the undercompression that gets worse as the outlet pressure rises.

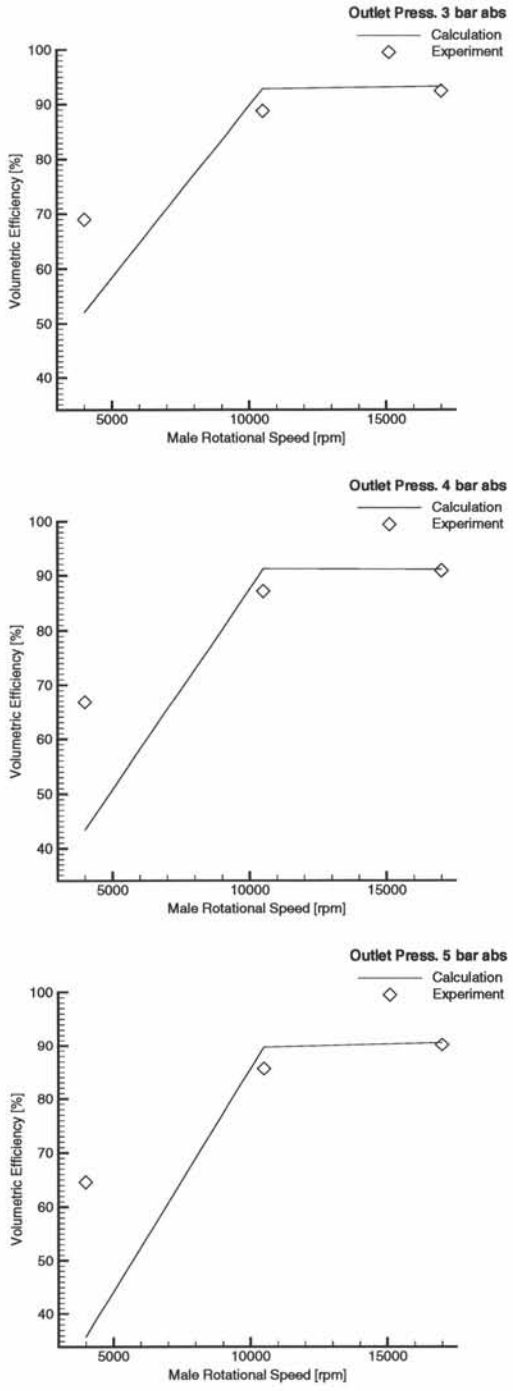

Figure 7.53: Plot of volumetric efficiency versus rotational speed for pressure ratio 3, 4 and 5

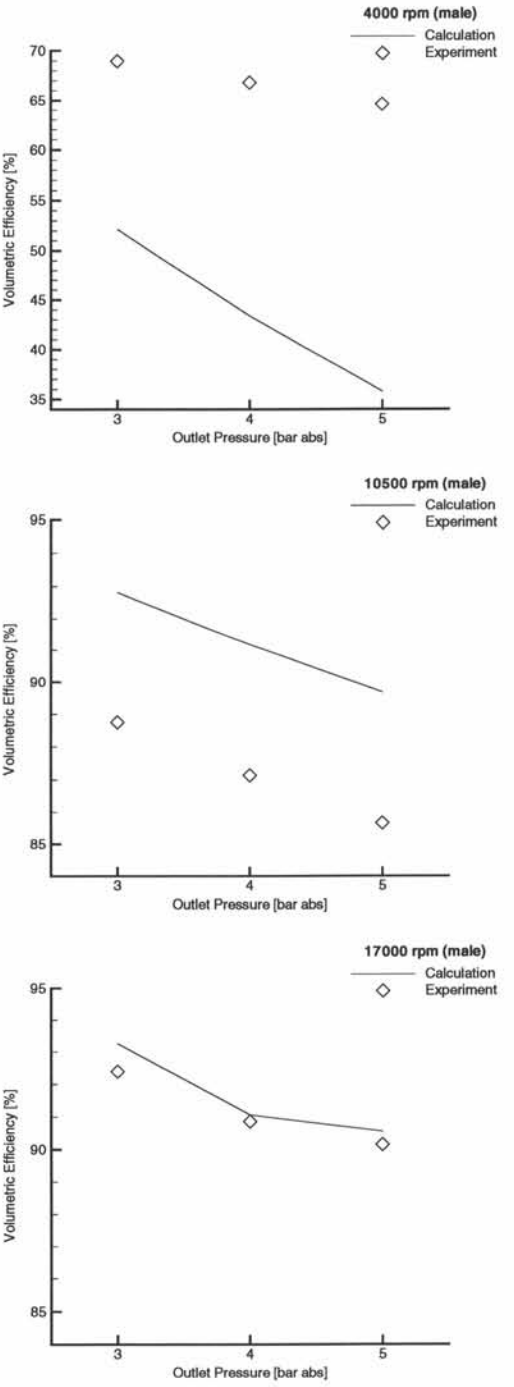

Figure 7.54: Plot of volumetric efficiency versus pressure ratio for rotational speed 4000 rpm, 10500 rpm and 17000 rpm

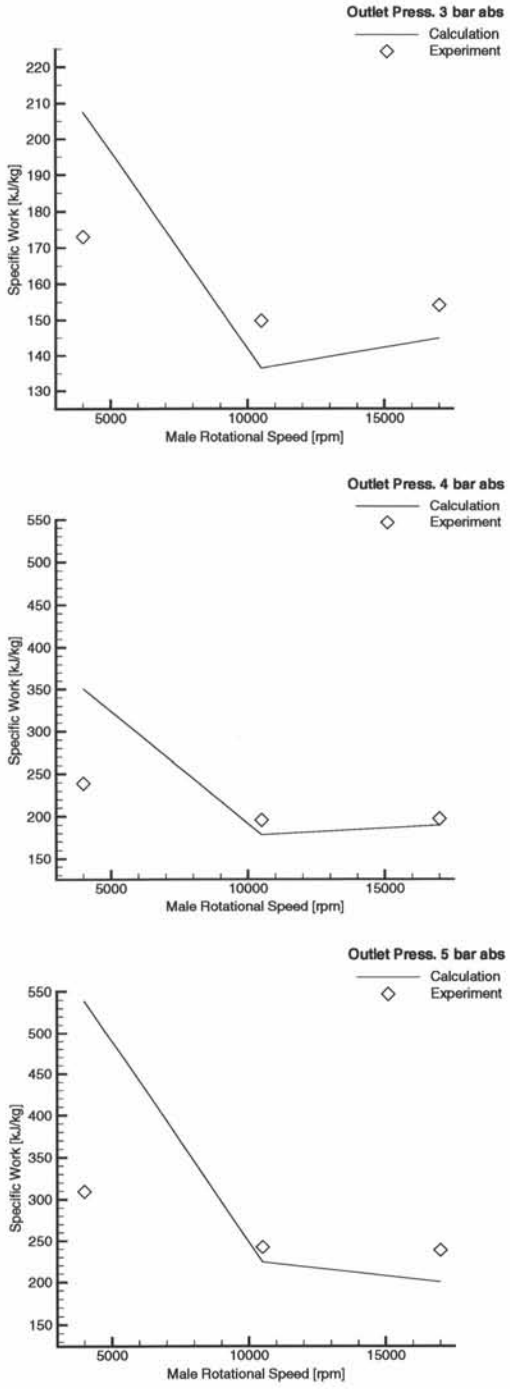

Figure 7.55: Plot of specific work versus rotational speed for pressure ratio 3, 4 and 5

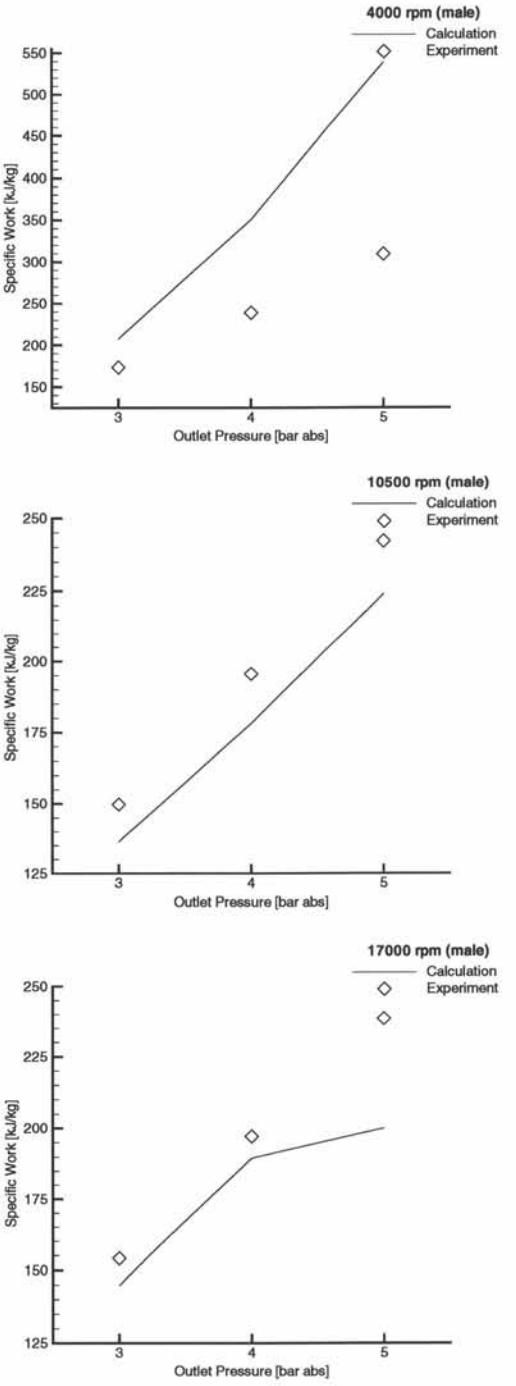

Figure 7.56: Plot of specific work versus pressure ratio for rotational speed 4000 rpm, 10500 rpm and 17000 rpm

Except for 4000 rpm, where the results are bad, the calculated specific work is slightly lower than the experimental one. Part of this is because of the slightly higher prediction of the volumetric efficiency. But part of it must also be attributed to mechanical losses (bearings, timing gear, ...) that are incorporated in the experimental results, but can't be added to the numerical calculations.

The temperature efficiencies are presented in figure 7.57 and table 7.5.1a.

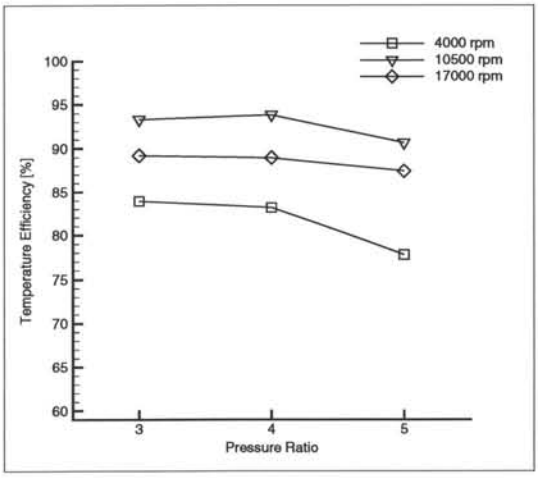

Figure 7.57: Plot of temperature efficiency versus pressure ratio for rotational speed 4000 rpm, 10500 rpm and 17000 rpm

ϵ_T	4000 rpm	10500 rpm	17000 rpm
1-3 bar	83.95	93.32	89.21
1-4 bar	83.19	93.83	88.95
1-5 bar	77.79	90.64	87.43

Table 7.5.1a: Temperature efficiency in %

7.5.2 Parameter study of the gap size

7.5.2a Reducing the gap size

As mentioned in the previous section, the results of the calculations at 4000 rpm lead to suspect that for this low speed the clearances are smaller than 30 microns. To test this assumption another calculation is performed at 4000 rpm, yet this time with clearances of only 10 micron. The grid for these smaller clearances is generated completely analogously as for the case described above. No problems were encountered.

The outlet pressure is set to be 3 bar. The volumetric efficiency and the specific work obtained numerically and experimentally are shown in table 7.5.2a.

	Experiment	Numerical 30 micron	Numerical 10 micron
ϵ_V	69.96	52.15	66.16
ΔW	172.97 kJ/kg	207.56 kJ/kg	161.43 kJ/kg

Table 7.5.2a

The numerical results obtained from the CFD calculation with the finer gaps are much closer to the experimental values. It seems that the theory proposed in the previous section, namely that the gaps between rotors and casing are much smaller in case of operation at very low speeds, is correct. Furthermore, it would seem that 10 microns is a good estimate for this gap size. However, the leakage flow at the end planes is neglected in these simulations, so it is difficult to make a strong statement about this.

Assessing the actual gap sizes in case of out of range operation is very important from a design standpoint. If the gaps were to become even smaller, the rotors might make contact with the casing. This could damage the rotors.

7.5.2b Increasing the gap size

In a similar fashion the dependency of the numerical results on the clearance size was tested for 10500 rpm. The efficiencies obtained numerically were better than the experimental, so in this instance the gaps were widened. The new clearance size is 50 micron. The outlet pressure was set to 3 bar.

The volumetric efficiency and the specific work are shown in table 7.5.2b.

	Experiment	Numerical 30 micron	Numerical 50 micron
ϵ_V	88.75	92.82	82.45
ΔW	149.77 kJ/kg	136.47 kJ/kg	152.12 kJ/kg

Table 7.5.2b

As expected, the volumetric efficiency is lower and the specific work higher. The volumetric efficiency is now lower than the experimental one. By interpolating between the calculated mass flow rates one might guess the clearances to be 41.05 microns. However, the specific work with a clearance of 50 micron is nearly right on the experimental value. As it is not possible to assess the mechanical losses of the compressor, it is difficult to make a stout statement. What must be born in mind is that the clearance at the end planes is neglected. Normally, air leaks back to the inlet through this gap. Therefore, the actual clearance between rotors and casing must be smaller than 41.05 micron. The educated guess of 30 micron seems to be a good one.

7.6 Conclusion

In this chapter the grid manipulation strategy discussed in chapter 6 was applied to an oil-free screw compressor geometry. The two-dimensional structured rectangular grid generator described in chapters 4 and 5 takes a pivotal place in the grid manipulation strategy.

For the final validation calculations, an oil-free screw compressor was chosen, as this is the most complex rotary positive-displacement machine. The geometry is fully three-dimensional. The rotors display three-dimensional features (helical shape). The size of the various gaps in the machine is extremely small (down to 10 micron).

The numerical results from the validation cases show good agreement with experimental results. The grid manipulation can be considered validated by the obtained results. They also stand as an example of the vast flow field information that can be obtained only through CFD in these machines.

As a conclusion, the arbitrary Lagrangian-Eulerian or ALE method coupled with the grid manipulation strategy developed is considered proven to be a valuable tool.

Chapter 8

Conclusion and Future Work

In this book the possible use of computational fluid dynamics or CFD calculations in rotary positive-displacement machines was studied.

It was concluded that CFD could be very useful in the development of these machines. Because of the specific geometry of rotary volumetric pumps and compressors, it is very difficult to obtain experimental flow field data. The design is mainly supported by one-dimensional models. At present day, the development of these machines has reached the point where there is a growing need for insight in the flow conditions inside the machine. Only a simulation using CFD can deliver this insight.

The problem that has withheld numerical flow calculations, is the complex movement of the flow domain boundaries (ie. the rotor surfaces) during the simulation. Two methods are studied that could solve this problem.

The first method is the Fictitious Domain method. This method was investigated in chapters 2 and 3. The technique circumvents the problem by not incorporating the offending moving boundaries in the calculation domain, yet simulating their influence on the fluid flow by locally adapting the flow equations.

The method was applied to incompressible flow with moderate success, but it is not suited for studying the various leakage flows. Serious difficulties were encountered when extending the method to compressible flow. The method was deemed not suitable for compressible flow calculations in rotary positive-

displacement machines.

The second method researched is the Arbitrary Lagrangian-Eulerian (ALE) method. In this method the grid is allowed to move during the simulation if the definition of the grid cells is unaltered. In facto, this method shifts the focus of the problem to grid generation and grid manipulation.

A robust grid manipulation strategy was developed and presented. This strategy allows ALE calculations using a hexagonal structured grid. At its core is situated a two-dimensional structured rectangular grid generator. The development of this grid generator is presented in chapters 4 and 5. It furnishes a two-dimensional domain with a structured rectangular grid based on a potential solution obtained in this domain. The favourable characteristics of this solution have been known since Winslow in 1967 [52]. The difference between the method presented and the methods derived from Winslow, is that the potential solution is explicitly obtained in the grid domain. This allows better control over the grid generation process.

The grid manipulation strategy was applied to flow calculations through a double-tooth compressor and an oil-free screw compressor. The results obtained numerically were compared with experimental results and a good agreement was found. The performed calculations validate the grid manipulation strategy. They were also used to illustrate the usefulness of CFD for these machines.

The grid manipulation algorithm is considered to be fully developed. It is sufficiently robust to perform ALE calculations in the most complex rotary positive-displacement machine geometries.

In the future, the grid manipulator can be used to research the various influences on the efficiencies of rotary volumetric compressors. A short example of how this could be done was presented at the end of chapter 7.

A very challenging extension is the inclusion of oil-injection in compressors. A powerful multiphase model will be needed. It is important that the mixing of oil and gas is captured accurately, as this mechanism extracts heat from the compressing gas, significantly influencing the compression efficiency. On the other hand, liquid films of oil will be formed inside the machine on the surfaces. These liquid films also have to be simulated accurately, as they seal various leakage paths between rotors and casing. Simulating both the break-up into a spray and the formation of an oil film promises quite a challenge.

Bibliography

[1] *StarCD Methodology.* CD Adapco, 2004.

[2] F. Baaijens. A fictitious domain/mortar element method for fluid-structure interaction. *Int. J. Numer. Meth. Fluids*, 35:734–761, 2001.

[3] F. Bertrand, P. Tanguy, and F. Thibault. Three-dimensional fictitious domain method for incompressible fluid flow problems. *Int. J. Numer. Meth. Fluids*, 25:719–736, 1997.

[4] F. Bertrand, F. Thibault, L. Delamare, and P. Tanguy. Adaptive finite element simulations of fluid flow in twin-screw extruders. *J. Comput. Chemic. Engrng.*, 27:491–500, 2003.

[5] R. Cortez and M. Minion. The blop projection method for immersed boundary problems. *J. Comput. Phys.*, 161:428–453, 2000.

[6] R. Cortez, C. Peskin, J. Stockie, and D. Varela. Parametric resonance in immersed elastic boundaries. *SIAM J. Appl. Math.*, 65:494–520, 2004.

[7] D. Deng and P. Shu. *Rotational Compressor.* Mechanical Engineering Press China, 1985. pp.91-96.

[8] E. Fadlun, R. Verzicco, P. Orlandi, and J. Mohd-Yusof. Combined immersed boundary finite-difference methods for three-dimensional complex flow simulations. *J. Comput. Phys.*, 161:35–60, 2000.

[9] C. Farhat, P. Geuzaine, and C. Grandmont. The discrete geometric conservation law and the nonlinear stability of ALE schemes for the solution of flow problems on moving grids. *J. Comput. Phys.*, 174:669–694, 2001.

[10] Z. Fong, F. Huang, and H. Fang. Evaluating the inter-lobe clearance of twin screw compressor by the iso-clearance contour diagram. *J. Mech. Mach. Theory*, 36:725–742, 2001.

[11] M. Fujiwara and Y. Osada. Performance analysis of an oil-injected screw compressor and its application. *Int. J. Refrig.*, 18(4):220–227, 1995.

[12] R. Glowinsky, T. Pan, and J. Periaux. Fictitious domain methods for incompressible viscous flow around moving rigid bodies. Brunel University, UK, 1996. MAFELAP.

[13] B. Griffith and C. Peskin. On the order of accuracy of the immersed boundary method for an elastic boundary with mass. *J. Comput. Phys.*, 208:75–105, 2005.

[14] C. Hirt, A. Amsden, and J. Cook. An arbitrary lagrangian-eulerian computing method for all flow speeds. *J. Comput. Phys.*, 14:227, 1974.

[15] Brackbill J. and J. Saltzman. Adaptive zoning for singular problems in two dimensions. *J. Comput. Phys.*, 46:342–368, 1982.

[16] E. Jung and C. Peskin. Two-dimensional simulation of valveless pumping using the immersed boundary method. *SIAM J. Sci. Comput.*, 23:19–45, 2001.

[17] J. Kim, D. Kim, and H. Choi. An immersed boundary finite-volume method for simulations of flow in complex geometries. *J. Comput. Phys.*, 171:132–150, 2001.

[18] P. Kramer and C. Peskin. Incorporating thermal fluctuations into the immersed boundary method. pages 1755–1758, 2003. Proceedings of the Second MIT Conference on Computational Fluid and Solid Mechanics.

[19] M. Lai and C. Peskin. An immersed boundary method with formal second-order accuracy and reduced numerical viscosity. *J. Comput. Phys.*, 160:132–150, 2000.

[20] M. Lesoinne and C. Farhat. Geometric conservation laws for flow problems with moving boundaries and deformable meshes. *Comput. Methods Appl. Mech. Engrg.*, 134:71–90, 1996.

[21] R. Leveque and Z. Li. The immersed interface method for elliptic equations with discontinuous coefficients and singular sources. *SIAM J. Numer. Anal.*, 31:1019–1044, 1994.

[22] Z. Li and M. Lai. The immersed interface method for the navier-stokes equations with singular forces. *J. Comput. Phys.*, 171:822–842, 2001.

[23] S. Lim and C. Peskin. Simulations of the whirling instability by the immersed boundary method. *SIAM J. Sci. Comput.*, 25:2066–2083, 2004.

[24] F. Litvin and P. Feng. Computerized design, generation and simulation of meshing of rotors of screw compressor. *J. Mech. Mach. Theory*, 32(2):137–160, 1997.

[25] D McQueen and C. Peskin. Heart simulation by an immersed boundary method with formal second-order accuracy and reduced numerical viscosity. In *Mechanics for a New Millenium*, 2001. Proceedings of the International Conference on Theoretical and Applied Mechanics (ICTAM) 2000.

[26] F. Muldoon and S. Acharya. Mass conservation in the immersed boundary method. Houston, TX, 2005. ASME. Fluids Engineering Division Summer Meeting.

[27] R. Nourgaliev, S. Wiri, T. Dinh, and T. Theofanous. Adaptive strategies for mass conservation in level set treatment. Toronto, ON, 2005. AIAA. 17th Computational Fluid Dynamics Conference.

[28] P. O'Neill. *Industrial Compressors.* IMechE, 1993. pp 572-578.

[29] P. O'Neill. *Industrial Compressors.* IMechE, 1993. pp 297-412.

[30] T. Pan. Numerical simulation of the motion of a ball falling in an incompressible viscous fluid. *C.R. Acad. Sci. Paris, Serie IIb*, 327:1035–1038, 1999.

[31] N. Patankar, P. Singh, D. Joseph, R. Glowinsky, and T. Pan. A new formulation of the distributed lagrange multiplier/fictitious domain method for particulate flows. *Int. J. Multiphase Flow*, April 1999.

[32] C. Peskin. *Flow Patterns around Heart Valves : a Digital Computing Method for Solving the Equations of Motion.* 1972. PhD thesis Yeshiva University.

[33] C. Peskin. The immersed boundary method. *Acta Numerica*, 11:479–517, 2001.

[34] K. Riemslagh, J. Vierendeels, and E. Dick. Two-dimensional incompressible navier-stokes calculations in complex-shaped moving domains. *J. Engineering Math.*, 34:57–73, 1998.

[35] A. Roma, C. Peskin, and M. Berger. An adaptive version of the immersed boundary method. *J. Comput. Phys.*, 153:509–534, 1999.

[36] P. Singh and J. Bowman. Calculation of blow hole area for screw compressors. pages 938–948, Purdue University, West Lafayette, 1990. International Compressor Engineering Conference.

[37] P. Singh, D. Joseph, T. Hesla, R. Glowinsky, and T. Pan. A distributed lagrange multiplier/fictitious domain method for viscoelastic particulate flows. *Int. J. Multiphase Flow*, 25:755–794, 1999.

[38] P. Singh and A. Onushak. A comprehensive computerized method for twin-screw rotor profile generation and analysis. pages 519–527, Purdue University, West Lafayette, 1984. International Compressor Engineering Conference.

[39] P. Singh and P. Schwartz. Exact analytical representation of screw compressor rotor geometry. pages 925–937, Purdue University, West Lafayette, 1990. International Compressor Engineering Conference.

[40] N. Stosic. Screw compressorsin refrigeration and air conditioning. *HVAC&R Research*, 10(3):233–263, 2004.

[41] N. Stosic, K. Hanjalic, Lj. Milutinovic, and A. Kovacevic. Investigation of the influence of oil injection upon the screw compressor working process. *Int. J. Refrig.*, 15(4):206–220, 1992.

[42] N. Stosic and A. Kovacevic. Short course on cfd for posititve-displacement comopressors. Technical report, City University, London, 2003.

[43] N. Stosic, I. Smith, and A. Kovacevic. Optimisation of screw compressors. *J. Appl. Therm. Engrng.*, 23:1177–1195, 2003.

[44] J. Thompson, F. Thames, and C. Mastin. Automatic numerical generation of body-fitted coordinate systems for fields containing any number of arbitrary two-dimensional bodies. *J. Comput. Phys.*, 15:299–319, 1974.

[45] H. Udaykumar, R. Mittal, P. Rampunggoon, and A. Khanna. A sharp interface cartesian grid method for simulating flows with complex moving boundaries. *J. Comput. Phys.*, 174:345–380, 2001.

[46] J. Vande Voorde. *Algoritmes voor stromingsberekening in bewegende geometrie.* 2001. Graduate thesis Ghent University.

[47] J. Vande Voorde and J. Vierendeels. A grid manipulation algorithm for ALE calculations in screw compressors. Toronto, ON, 2005. AIAA. 17th Computational Fluid Dynamics Conference, Awarded Second Prize in the 1st AIAA Student CFD Competition.

[48] J. Vande Voorde, J. Vierendeels, and E. Dick. A force-based grid manipulator for ALE calculations in a lobe pump. *J.Therm. Science*, 12(4):318–322, 2003.

[49] J. Vande Voorde, J. Vierendeels, and E. Dick. Development of a laplacian-based mesh generator for ALE calculations in rotary volumetric pumps and compressors. *J. Comput. Methods Appl. Mech. Engrg*, 193:4401–4415, 2004.

[50] J. Vande Voorde, J. Vierendeels, and E. Dick. Flow simulations in rotary volumetric pumps and compressors with the fictitious domain method. *J. Comput. Appl. Math.*, 168:491–499, 2004.

[51] J. Vimmr. Mathematical modeling of compressible inviscid fluid flow through a sealing gap in the screw compressor. *J. Math. Comput. in Simul.*, 61:187–197, 2003.

[52] A. Winslow. Numerical solution of the quasi-linear poisson equation in a nonuniform triangle mesh. *J. Comput. Phys.*, 1:149–172, 1967.

[53] H. Wu, X. Peng, Z. Xing, and P. Shu. Experimental study on p-v indicator diagrams of twin-screw refrigeration compressor with economizer. *J. Appl. Thermal Engrng.*, 24:1491–1500, 2004.

[54] T. Ye, R. Mittal, H. Udaykumar, and W. Shyy. An accurate cartesian grid method for viscous incompressible flows with complex immersed boundaries. *J. Comput. Phys.*, 156:209–240, 1999.

[55] D. Zaytsev and C. Infante Ferreira. Profile generation method for twin screw compressor rotors based on the meshing line. *Int. J. Refrig.*, 2004.

[56] L. Zhang and J. Hamilton. Main geometric characteristics of the twin screw compressor. pages 449–456, Purdue University, West Lafayette, 1992. International Compressor Engineering Conference.

[57] Z. Zhou. Computer aided design of a twin-rotor screw refrigerant compressor. pages 457–466, Purdue University, West Lafayette, 1992. International Compressor Engineering Conference.

[58] L. Zhu and C. Peskin. Simulation of a flapping flexible filament in a flowing soap film by the immersed boundary method. *J. Comput. Phys.*, 179:452–468, 2003.

Appendix A

A Force-Based Grid Manipulator for ALE Calculations in a Lobe Pump

This calculation was published in the Journal of Thermal Science Vol.12-4(2003) pp. 318-322 [48].

A Force-Based Grid Manipulator for ALE Calculations in a Lobe Pump.

John Vande Voorde, Jan Vierendeels and Erik Dick.
Department of Flow, Heat and Combustion Mechanics,
Ghent University, Belgium
e-mail : John.Vandevoorde@rug.ac.be

In this paper, a time-dependant calculation of flow in a lobe pump is presented. Calculations are performed using the arbitrary Lagrangean Eulerean (ALE) method. A grid manipulator is needed to move the nodes between time steps. The used grid manipulator is based on the pseudo-force idea. This means that each node is fictitiously connected with its 8 neighbours via fictitious springs. The equilibrium of the resulting pseudo spring forces, defines the altered position of the nodes. The grid manipulator was coupled with a commercial flow solver and the whole was tested on the flow through a three-lobe lobe pump. Results were obtained for a rotational speed of 460 rpm and incompressible silicon oil as fluid.

keywords : ALE, arbitrary Lagrangean Eulerean, moving grids, lobe pump.

I. Introduction.

A lobe pump is a rotary displacement pump. Figure 1 depicts the geometry of a lobe pump with three-lobes for different rotation angles. As the rotors rotate, the lobes seal off volumes of fluid and transport this fluid from the suction side to the pressure side.

As a lobe pump is a cyclic volumetric machine, only time-dependent flow simulations are meaningful.

Due to the interlocking of the rotors, it is impossible to divide the flow domain into zones where the grid would stay unaltered in an attached coordinate system (a prerequisite to use a sliding meshes method). As is obvious from figure one, any potential grid used to discretize the flow domain, will have to adapt to the changing geometry.

The only method applicable to this problem is the Arbitrary Lagrangean Eulerean method (ALE).

The ALE method basically prescribes that any movement of the grid nodes in-between time steps is allowed, as long as the grid topology is maintained. This means that no new cells may appear and no cells may disappear. Every cell in the new grid must be defined by the same corner vertices.

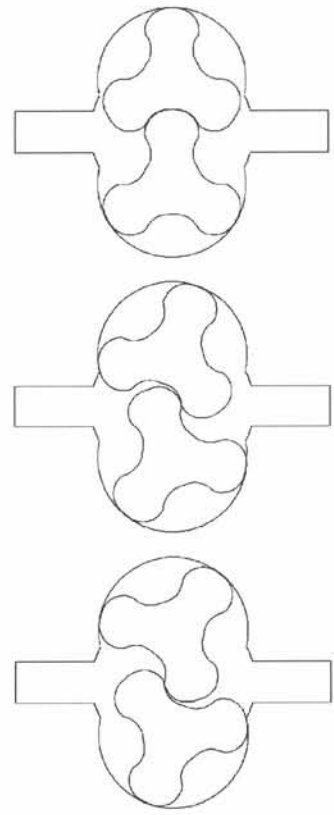

Figure 1. The geometry of a three-lobe lobe pump. Inlet left and outlet right. The rotation is clockwise for the top rotor and counter-clockwise for the bottom rotor. The rotation angles are 0 (top), 20 (middle), and 40 degrees (bottom).

The theoretical repercussions to the flow solver are minimal. Only one equation, expressing conservation of volume, must be added to the flow equations.

The main problem lurks in the movement of the nodes. Of course the aim of the method is to obtain a valid and qualitatively good grid at each time step. For complex moving geometries, such as a lobe pump, this is not straightforward.

The aim of this paper is to present a separate piece of software, named a grid manipulator, whose task it is to move the nodes in-between time steps to a suitable position. The actual calculation of the flow is handled by a commercial code, used as a black box in this respect.

II. A force-based grid manipulator.

2.1 General.

Many basic ideas exist for grid manipulation algorithms. Most grid manipulators have a top-down approach. This approach can be strictly mathematical or have some relation to a physical principle (the new position of the nodes can for instance be based on the calculation of the deformation of a fictitious elastic sub-layer attached to the nodes [1]).

The grid manipulator presented in this paper however takes a bottom-up approach.

Consider a node (i,j) and its eight direct neighbours (cf. figure 2). In each node (i,j) a pseudo-force $F_{i,j}$ is defined determined by its position relative to its neighbours (1).

This approach has already been applied before on unstructured grids [2].

$$F_{i,j} = F\left(\vec{r}_{i,j}, \vec{r}_{i-1,j}, \vec{r}_{i+1,j}, \vec{r}_{i-1,j-1}, \vec{r}_{i,j-1}, \vec{r}_{i+1,j-1}, \vec{r}_{i-1,j+1}, \vec{r}_{i,j+1}, \vec{r}_{i+1,j+1}\right) \quad (1)$$

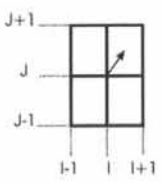

Figure 2. A node (i,j) (left) and a cell (right) with its direct neighbouring nodes.

It must be stressed that the forces introduced in this manner hold absolutely no reference to the actual flow field, hence the naming pseudo-forces.

With the thus defined pseudo-forces, the unique position of all nodes can be calculated for which a force-equilibrium is obtained. The nodes are updated to this new position.

A good definition of the pseudo-forces (1) is of course essential to the quality of the obtained grid.

Although certain pseudo-force definitions are equivalent to a top-down mathematical algorithm (the example presented next for instance), one has more freedom in the definition of the pseudo-forces. Furthermore there is the somewhat philosophical point of view that each node's motion is based solely on the local grid situation, which gives the algorithm a more general approach. In this regard, the force-based method bears resemblance to the theory of cellular automata and the lattice-gas fluid dynamics.

2.2 An example of a pseudo-force.

One of the simplest pseudo-forces conceivable is a pseudo-spring force.

Just imagine all cell faces (of a two-dimensional grid) being springs with a constant stiffness 1. The pseudo-force definition is (2).

$$\vec{F}_{i,j} = \left(x_{i-1,j} + x_{i+1,j} + x_{i,j-1} + x_{i,j+1} - 4 \cdot x_{i,j}\right) \cdot \vec{e}_x + \left(y_{i-1,j} + y_{i+1,j} + y_{i,j-1} + y_{i,j+1} - 4 \cdot y_{i,j}\right) \cdot \vec{e}_y \quad (2)$$

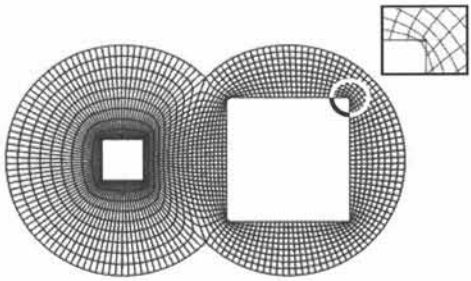

Figure 3. A simple test case for the pseudo-spring method with constant stiffness. The circle on the right accentuates the grid drawn over a sharp intrusion into the flow domain.

The resulting algorithm was applied to a simple test case (cf. figure 3). The left side of the test case shows that this very simple definition nevertheless yields a gentle good grid. The right side however illustrates the main problem. It doesn't handle intrusions of the geometry in the flow domain well.

As a note about equivalency the following. The careful reader may have already noticed that (2) is also (exempt a multiplying factor) a definition for a Laplacean grid smoother. Its problems with sharp intrusions are well known.

But furthermore does the force-balance of (2) prescribe that each node is moved to the analytical middle of its north, east, south and west neighbours. This viewpoint makes the intrusion problems self-explanatory.

This simple example is a nice illustration of both the potential of a bottom-up method and its generality.

2.3 An improved pseudo-spring.

Based on an advanced grid smoother [3] the spring stiffnesses are made dependant on the position of the neighbouring nodes and extra diagonal pseudo-springs are added (connecting the centre node with the NE, SE, SW and NW neighbouring nodes).

The new pseudo-force definitions are (3).

Multiplying the stiffnesses of the pseudo-springs in I-direction, J-direction and the diagonal springs with weighing factors allows to fine-tune the effects of the variability of the pseudo-spring stiffness to one's needs.

$$\vec{F}^{\,I}_{i,j} = \frac{1}{4}\cdot\left[\left(x_{i,j+1}-x_{i,j-1}\right)^2+\left(y_{i,j+1}-y_{i,j-1}\right)^2\right] \times\left[\left(x_{i-1,j}+x_{i+1,j}-2\cdot x_{i,j}\right)\cdot\vec{e}_x+\left(y_{i-1,j}+y_{i+1,j}-2\cdot y_{i,j}\right)\cdot\vec{e}_y\right] \tag{3a}$$

$$\vec{F}^{\,J}_{i,j} = \frac{1}{4}\cdot\left[\left(x_{i+1,j}-x_{i-1,j}\right)^2+\left(y_{i+1,j}-y_{i-1,j}\right)^2\right] \times\left[\left(x_{i,j-1}+x_{i,j+1}-2\cdot x_{i,j}\right)\cdot\vec{e}_x+\left(y_{i,j-1}+y_{i,j+1}-2\cdot y_{i,j}\right)\cdot\vec{e}_y\right] \tag{3b}$$

$$\vec{F}^{\,D}_{i,j} = -\frac{1}{4}\left[\left(x_{i+1,j}-x_{i-1,j}\right)\cdot\left(x_{i,j+1}-x_{i,j-1}\right)\cdot\left(y_{i+1,j}-y_{i-1,j}\right)\cdot\left(y_{i,j+1}-y_{i,j-1}\right)\right]\times \left[\left(x_{i+1,j+1}+x_{i-1,j-1}-x_{i+1,j-1}-x_{i-1,j+1}\right)\cdot\vec{e}_x+\left(y_{i+1,j-1}+y_{i-1,j-1}-y_{i+1,j-1}-y_{i-1,j+1}\right)\cdot\vec{e}_y\right] \tag{3c}$$

The algorithm resulting from these new definitions is now capable of handling the irregular flow domains that may result from complex moving geometries.

2.4 Finishing touches.

The algorithm described above is capable of redistributing the internal nodes of the grid in such a manner that a good grid is obtained. However, before moving the internal nodes, the nodes on the boundaries must be moved to a better position.

To do this the same approach is used as above. Nodes on the inner and the outer boundaries with the same I-coordinate are connected with pseudo-springs with a constant stiffness $C_0 = 0.9$ (4). Neighbouring nodes on the same boundary are connected with pseudo-springs with constant stiffness 1.

$$\vec{F}^{\,I=0}_{i} = c_0\times\left[\left(x_{i,inner}-x_{i,outer}\right)\cdot\vec{e}_x+\left(y_{i,inner}-y_{i,outer}\right)\cdot\vec{e}_y\right] \tag{4}$$

In a first step, the force balance of these pseudo-forces is calculated. This determines the new position of the boundary nodes. In a following step the internal nodes are redistributed as described in the former subsection.

This algorithm can produce an appropriate grid for every time step during the simulation of flow in a lobe pump. This will now be demonstrated in the next section.

III. A working example : the lobe pump.

3.1 The grid manipulation.

In this section an ALE calculation on the lobe pump whose geometry is shown in figure 1 will be worked out.

The flow domain is divided in four zones : an inlet zone, an outlet zone and two zones attached to the two rotors. The grid in the inlet and outlet zones contains 1759 nodes and will remain unchanged during the simulation.

The grid of the zones attached to the upper and the lower rotor will be adapted at each time step by the previously described grid manipulator. Figure 4 shows a valid grid in these two zones for a rotation of zero degrees. The resolution is twice 225x20 nodes.

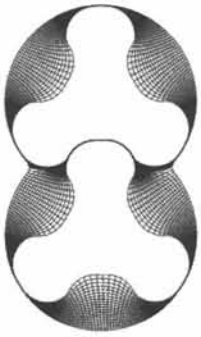

Figure 4. Starting grid. Zero degrees rotation.

The nodes on the outer boundary remain fixed during manipulation. This is done to prevent the need for sliding grid interfaces when connecting the four zones. This does not interfere with the working of the manipulation algorithm. In fact, an equidistant spacing of the nodes on the outer boundary is beneficial to the grid quality.

Figure 5 shows the execution of the first step of the algorithm. For visibility purposes only the nodes considered are connected. On the left the result of a twenty-degree rotation of the rotors is shown. On the right the new position of the boundary nodes is depicted.

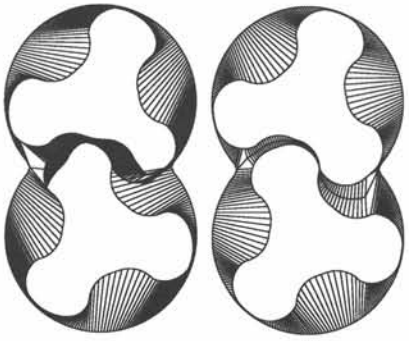

Figure 5. Moving the nodes on the rotors to a suitable position.

One can see that a good compromise is obtained between minimizing the distance between corresponding nodes on inner and outer boundary (which will prevent cell wrapping), and maintaining an even distribution of the nodes on the boundaries (which will prevent high aspect ratios and large differences in cell volume).

Figure 6 shows the resulting grid after executing the second part of the manipulation algorithm. The grid in inlet and outlet zones is also depicted. One can observe that a grid of sufficient quality is obtained.

3.2 The actual flow calculation.

Using the grid manipulator to move the nodes between time steps, an ALE calculation of the flow was set up. The flow solver applied here was the commercial code StarCD v3.15A.

The fluid simulated is silicon oil. This oil is to be considered incompressible. It has a density of 880 kg/m^3 and a viscosity of 0.04048 kg/m.s.

The rotational speed of the lobe pump is 460 rpm. The surface of the rotors is calculated to be 0.00730 m^2. With these values a theoretical mean mass flow rate of 87.61 kg/s.m is determined. This theoretical value does not account for leakage, so the actual value is lower. Unfortunately, no experimental data is available, so a rigorous validation of the results is not possible.

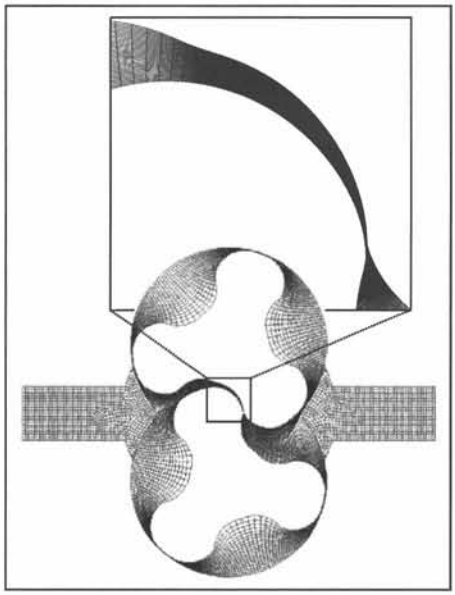

Figure 6. The complete resulting grid for twenty degrees rotation.

A two-dimensional simulation with these values was performed. The inlet and outlet boundary conditions were pressure boundary conditions (both 1 bar absolute). The turbulence model used is Chen's k-ε model.

Figure 7 shows a plot of the simulated mass flow rate versus the rotation angle as well as the mean mass flow rate. It should be pointed out that a rotation of 1440 degrees is equivalent with 24 cycles of the lobe pump and that the simulation is transiently converged. The resulting mean mass flow rate is 84.11 kg/s.m, which would be close to reality.

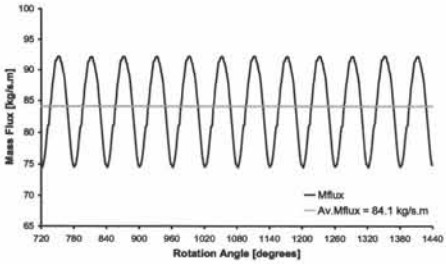

Figure 7. Actual and mean mass flow rate through the lobe pump versus rotation angle.

Finally figure 8 shows plots of velocity vectors for several rotation angles. Figure 9 shows the good resolution of the results in the gaps.

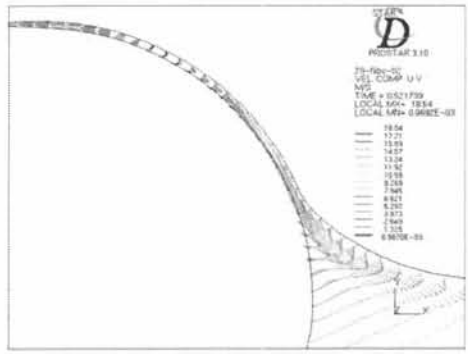

Figure 9. Plot of velocity vectors in the gap between the rotors. Rotation angle is zero degrees.

IV. Conclusion.

In this paper a pseudo-force based grid manipulator for ALE calculations with structured grids was presented. This manipulator was applied to the test case of incompressible flow in a three-lobe lobe pump, and the results obtained from this test case show the effectiveness of this grid manipulator.

Acknowledgement :

The research reported here was funded with a fellowship granted by the Flemish Institute for the Promotion of Scientific and Technological Research in the Industry (IWT).

References :

[1] *Mer K. and Nkonga B.* : Implicit Calculations of an Aero-elasticity Problem, Int. J. Comp. Fluid Dyn., vol 9, pp. 165-178 (1998)

[2] *K. Riemslagh, J. Vierendeels and E. Dick* : Two-dimensional incompressible Navier-Stokes calculations in complex-shaped moving domains. J. Eng. Math., vol 34(1-2), pp.57-73 (1998).

[3] *Thompson J.F., Thames F.C. and Mastin C.W.* : Automatic numerical grid generation of body-fitted curvilinear coordinate system of field containing and number of arbitrary 2-dimensional bodies, J. Comp. Physics, vol 15, pp. 299-319 (1974).

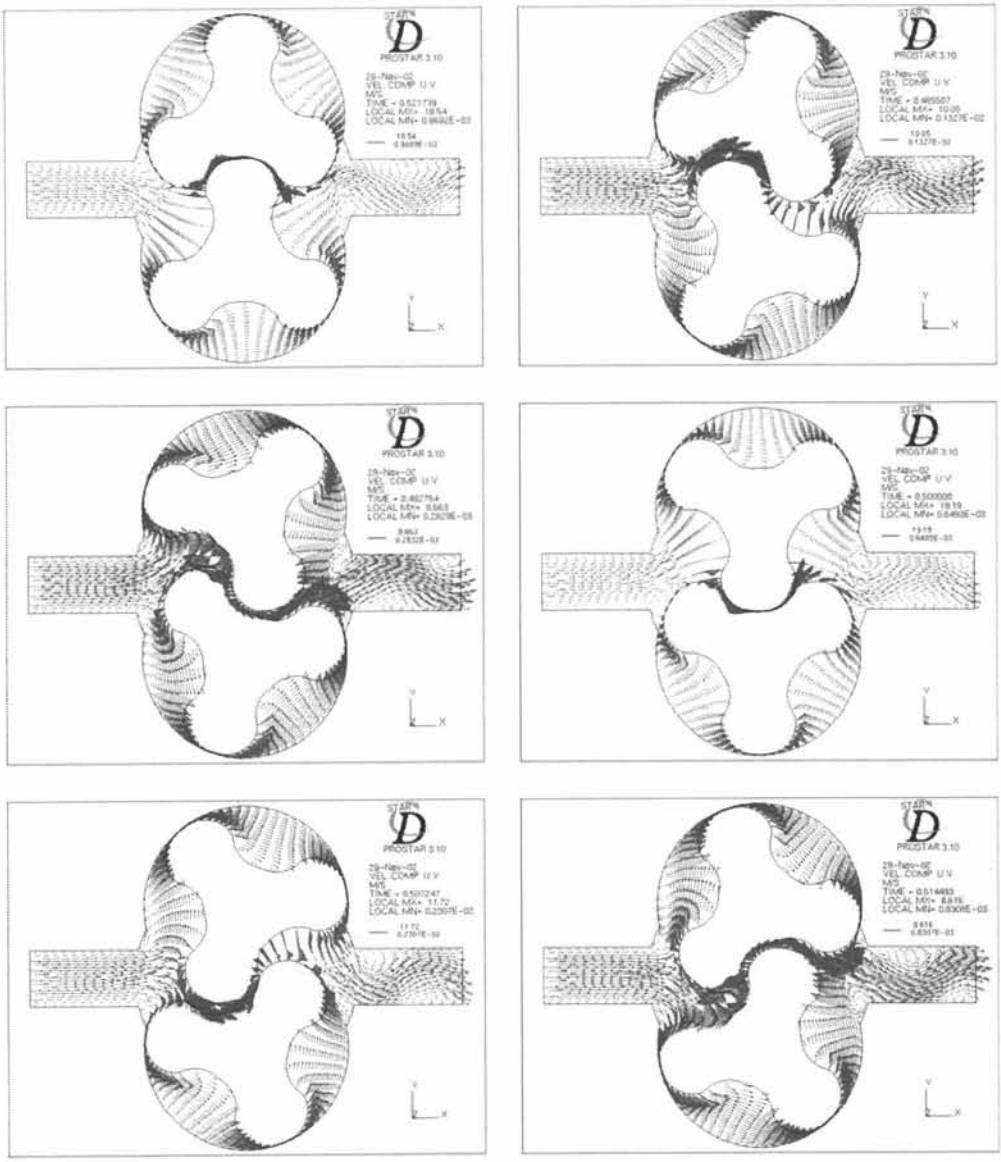

Figure 8. Plots of velocity vectors. Rotation angles : 0, 20, 40, 60, 80 and 100 degrees.